Supporting Information

Photogenerated Ni(I)–Bipyridine Halide Complexes: Structure-Function Relationships for Competitive C(sp^2)–Cl Oxidative Addition and Dimerization Reactivity Pathways

David A. Cagan[†], Daniel Bím[†], Brendon J. McNicholas, Nathanael P. Kazmierczak, Paul H. Oyala, and Ryan G. Hadt*

Division of Chemistry and Chemical Engineering, Arthur Amos Noyes Laboratory of Chemical Physics, California Institute of Technology, Pasadena, California 91125, United States

*Corresponding Author: rghadt@caltech.edu

Table of Contents

S1. Experimental Section.

S1.1. General Considerations.

All purchased compounds were used as received unless otherwise noted. Bis-(1,5-cyclooctadiene) nickel(0) was purchased from Strem Chemicals. Ligands 4,4′-di-*tert*-butyl-2,2′-bipyridine ($^{t\text{-Bu}}$bpy), 2,2′-bipyridine (bpy), and dimethyl-2,2′-bipyridine-4,4′-dicarboxylate (^{MeOOC}bpy) were purchased from Sigma-Aldrich. Aryl halide compounds, 2-*chloro*-toluene, 2-*bromo*-toluene, 2-*iodo*-toluene, 2-*chloro*-α,α,α-trifluorotoluene, 4-*chloro*-anisole, 4-*chloro*-toluene, *chloro*-benzene, 4-*chloro*-benzamide, and 4′-*chloro*-acetophenone were also obtained from Sigma-Aldrich. Solids were dried under vacuum and brought into a nitrogen-atmosphere glove box; liquids were sparged (N_2) and degassed via freeze-pump-thaw techniques, brought into the glove box, and stored over 3 Å molecular sieves. All solvents were air-free and collected from the solvent purification system (SPS), then stored in the glove box over 3 Å molecular sieves. Tetrahydrofuran (THF), 2-methyl tetrahydrofuran (2-MeTHF), and d_8-tetrahydrofuran (d_8-THF) were inhibitor-free. All synthesized compounds were made using air-free Schlenk techniques or made in the glove box. All synthesized complexes are considered air and moisture sensitive. Light sensitivity was also seen even in the solid state if left exposed for extended time.

Room temperature UV-vis spectra of the complexes were obtained on a Varian Cary 500 spectrophotometer or a StellarNet Inc. Black Comet UV-vis spectrophotometer. Variable temperature (heating) decomposition kinetics were acquired on a UV-vis HP Agilent 8453 spectrophotometer coupled to an HP 89090A Peltier temperature controller with a cell holder. Variable temperature (cooling) UV-vis spectra were acquired using a Varian Cary 50 spectrophotometer equipped with a USP-203 series cryostat (UNISOKU Co.) and a liquid nitrogen dewar. Samples were equilibrated at each temperature for five minutes prior to acquisition. All spectra were baselined in THF at the appropriate temperature. Starna Cells 6-Q 2- or 10-mm path length cuvettes fitted with air-tight seals were used.

Proton nuclear magnetic resonance (^{1}H NMR) and fluorine nuclear magnetic resonance (^{19}F NMR) spectra were recorded on a 400 MHz Varian Spectrometer with broadband auto-tune OneProbe. ^{13}C NMR spectra were collected on a Bruker AV-III HD 400 MHz spectrometer and were ^{1}H decoupled. ^{19}F NMR were externally referenced to neat fluorobenzene (δ = -113.15 ppm). Chemical shifts are reported in parts per million (δ in ppm, s: singlet, d: doublet, t: triplet, m: multiplet) and are referenced to residual solvent signal (d_8-THF = 3.58 ppm). Deuterated solvents were dried and stored over activated 3 Å molecular sieves in a nitrogen-filled glove box for at least three days before use. Fourier transform infrared (FTIR) spectra were collected using a Thermo Scientific Nicolet iS5 FTIR spectrometer with an iD5 diamond ATR accessory in an inert-atmosphere glove box. Electron paramagnetic resonance (EPR) spectroscopy was performed using a Bruker EMX X-band CW-EPR Spectrometer equipped with a ER4119HS high sensitivity resonator or ER4116DM dual mode resonator for room temperature and cryogenic experiments, respectively. Room temperature spectra in 2-MeTHF were collected in a 1.5 mm I.D. quartz capillary tube inside an air-free standard 4 mm O.D. quartz X-band EPR tube. Spectra at cryogenic temperatures were performed using an Oxford ESR 900 liquid helium/nitrogen flow-through cryostat after freezing samples in liquid nitrogen. The recorded spectra were simulated in EasySpin for Matlab. Room temperature cyclic voltammetry was performed in a nitrogen-filled glove box with a Gamry Reference 600 or Biologic SP-200 potentiostat using a three-electrode cell. Spectroelectrochemistry was performed in a nitrogen-filled glove box with a Gamry Reference 600 or Biologic SP-200 potentiostat.

S1.2. Photochemical Setup.

Photochemical stocks were prepared in a nitrogen-filled glove box and distributed into separate spectroscopic cuvettes (Starna Cells, 2- or 10-mm path length) with air-tight seals. Each cuvette cell had volume of 3.0 mL as determined by syringe and were placed 5 cm away from a Kessil PR160L LED (λ_{max} = 370 nm unless otherwise stated, P_{LED} = 70 mW cm^{-2} at 5 cm distance) on highest setting. A cooling fan was used to maintain room temperature irradiation during the experiment. Sample positions were rotated periodically to ensure even irradiation throughout the entire duration of the experiment.

S1.3. Synthetic Details.

Preparation of parent Ni(II)–bpy aryl halide complexes.

The parent four-coordinate complexes, Ni(II)($^{t\text{-Bu}}$bpy)(*o*-tolyl)Cl, Ni(II)($^{t\text{-Bu}}$bpy)(*o*-tolyl)Br, Ni(II)(bpy)(*o*-tolyl)Cl, and Ni(II)($^{t\text{-Bu}}$bpy)(CF_3Ph)Cl were synthesized according to previous reports.[1,2] Their spectroscopic properties were identical to those described prior.[1,2] The parent complexes Ni(II)($^{t\text{-Bu}}$bpy)(*o*-tolyl)I and Ni(II)(^{MeOOC}bpy)(*o*-tolyl)Cl were prepared following a modified literature procedure (see below).

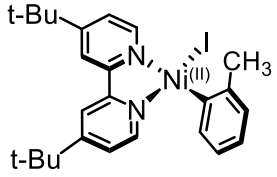

Ni(^{tBu}bpy)(*o*-tolyl)I. In a nitrogen filled glove box, a 20 mL scintillation vial was charged with a Teflon coated stir bar, bis-(1,5-cyclooctadiene) nickel(0) (0.195 g, 0.709 mmol, 1 eq.), and 4,4′-*tert*-butyl-2-2′-bipyridine (0.210 g, 0.782 mmol, 1.1 eq.). To this vial, 3.0 mL THF was added, and the mixture was stirred for one hour affording a deep purple solution. Subsequently, 0.3 mL of 2-*iodo*-toluene (excess) was added dropwise, while stirring. A red solid precipitated. Mixture was left stirring for 15 minutes longer, then transferred to aa 75 mL amber jar. Pentanes (40 mL) were added, and the mixture was left to stir for 45 minutes. The jar was placed in the freezer (-35 °C) overnight to complete the precipitation. The solid was then collected by filtration, washed with pentanes (3x10 mL or until filtrate is clear), then dried under vacuum (0.356 g, 92% yield). UV-vis (THF): λ_{MLCT} = 488 nm, $\varepsilon_{488\ nm}$ = 2200 M^{-1} cm^{-1}. ^{1}H NMR (400 MHz, CD_2Cl_2): δ 9.56 (d, *J* = 6.0 Hz, 1H), 7.83 (d, *J* = 14.0 Hz, 2H), 7.58 (d, *J* = 7.4 Hz, 1H), 7.46 (d, *J* = 6.0 Hz, 1H), 7.17 (d, *J* = 6.2, 2.1 Hz, 1H), 6.87 – 6.80 (m, 2H), 6.77 (t, *J* = 7.3 Hz, 1H), 6.70 (t, *J* = 7.2 Hz, 1H), 2.96 (s, 3H), 1.40 (s, 9H), 1.34 (s, 9H). ^{13}C{^{1}H}NMR (100 MHz, CD_2Cl_2) δ 163.44, 162.93, 155.88, 153.80, 153.24, 149.50, 147.92, 143.19, 137.82, 127.50, 123.81, 123.26, 122.29, 117.78, 117.37, 35.56, 30.27, 30.09, 26.76. FT-IR (ATR, cm^{-1}): 600, 734, 840, 858, 1015, 1250, 1407, 1544, 1616, 2862, 2896, 2961, 3052.

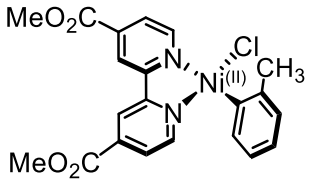

Ni(^{CH_3OOC}bpy)(*o*-tolyl)Cl. In a nitrogen filled glove box, a 250 mL Schlenk flask was charged with a Teflon coated stir bar and crystalline Ni(TMEDA)(*o*-tolyl)Cl (red crystals grown from slow evaporation in hexanes/THF, 2.25 g, 0.746 mmol, 1 eq.). To this vial, dimethyl-2,2′-bipyridine-4,4′-dicarboxylate (2.23 g, 0.819 mmol, 1.1 eq.) was added along with 128 mL of heptane and 22 mL toluene (6:1 heptane/toluene). *Note that it was important to carefully wash the solid down the sides of the Schlenk flask, as separation of unreacted starting Ni(TMEDA)(o-tolyl)Cl is challenging during the work-up phase; excess bpy is used to aid in consumption of all Ni(TMEDA)(o-tolyl)Cl.* Upon removal from the glove box, the flask was sonicated for 10 minutes to promote solubilization of the reagents. The flask was attached to the nitrogen Schlenk line, covered in aluminum foil (product is light sensitive), and stirred at 60 °C for 18 hours affording a deep purple solution. The temperature was then increased to 65 °C for an additional 8 hours. After allowing the Schlenk flask to cool, it was brought back into the glove box where it had precipitated a purple solid. This solid was collected by vacuum filtration, washed copiously with pentanes and hexanes, then was dried under vacuum (3.1 g, 91% yield). Spectroscopic properties were identical to those reported previously.[1,2]

Preparation of the dimeric [Ni(I)($^{t\text{-}Bu}$bpy)Cl]$_2$ complex.

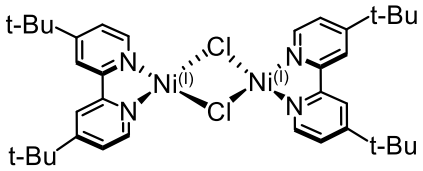

[Ni(I)($^{t\text{-}Bu}$bpy)Cl]$_2$. The title complex was prepared according to literature precedent,[2] save that the washing step was done with toluene and 2-methyl THF instead of benzene and THF owing to decreased solubility of the complex in the former solvents. When fully dry, the solid is a gray powder; when wet or in solution, it is black-brown. ^{1}H NMR (400 MHz, d_8-THF): δ 130 (broad s, 1.3H), 56–58 (broad d, 3.0H), 36–41 (broad d, 2.7H), 1.29 (s, 35.0 H). EPR analysis gave no resolvable signals as demonstrated previously (T = 5 K, 9.638 GHz, 8 G modulation amplitude, 2.184 mW power).

Preparation of Ni(I)–bpy halide complexes.
Ni(I)(^{R}bpy)X compounds were accessed directly from their parent Ni(II)–bpy aryl halide precursors by air- and moisture-free irradiation at 370 nm using Kessil PR160L purple LEDs and were characterized by UV-vis and EPR spectroscopies. Typical irradiation times were ~30-60 minutes, but these varied with each complex and were dependent on the individual compound's rate of Ni(I) photochemical formation and decay, initially described in our earlier work by k_p and k_d, respectively (Table S1).[1] These irradiation times, t, were chosen to maximize the concentration of Ni(I) in solution and minimize the amount of decomposition product(s) by observing the following kinetic analysis.

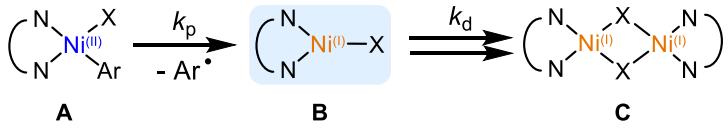

Scheme S1. Photochemical reaction pathway initially modeled in reference 1 using global analysis. In this model, k_p is the first-order rate constant for the photolysis step and k_d is the bimolecular rate constant for the decay step.

For an initial approximation, we can model the process given in **Scheme S1** as a sequential first-order reaction involving the conversion of **A** to **C** via an intermediate species, **B**, i.e., [$\boldsymbol{A} \rightarrow \boldsymbol{B}$, $\boldsymbol{B} \rightarrow \boldsymbol{C}$], where the initial concentrations of the intermediate and product species are zero, i.e., $[\mathbf{B}]_o = [\mathbf{C}]_o = 0$, $[\mathbf{A}]_o > 0$, the concentration of **B** can be given by equation S1, and the change in its concetration by equation S2.

$$[\mathbf{B}] = \frac{k_p}{(k_d - k_p)}\left(e^{-k_p t} - e^{-k_d t}\right)[\mathbf{A}]_o \qquad \textbf{(eq. S1)}$$

$$\frac{\delta[\mathbf{B}]}{\delta t} = \frac{k_p}{(k_d - k_p)}\left(-k_p e^{-k_p t} + k_d e^{-k_d t}\right)[\mathbf{A}]_o \qquad \textbf{(eq. S2)}$$

Solving for the maximum concentration of **B**, we set equation S2 to zero and find equations S3-S5.

$$k_p e^{-k_p t} = k_d e^{-k_d t} \qquad \textbf{(eq. S3)}$$

$$\ln(k_p) - k_p t = \ln(k_d) - k_d t \qquad \textbf{(eq. S4)}$$

$$\ln(k_p) - \ln(k_d) = (k_p - k_d)t \qquad \textbf{(eq. S5)}$$

Therefore, the irradiation time, t, which maximizes the concentration of the Ni(I)–bpy halide species is given by equation S6.

$$t = \frac{\ln(k_p) - \ln(k_d)}{(k_p - k_d)} \qquad \textbf{(eq. S6)}$$

These irradiation times were used for the preparation of the Ni(I)–bpy halide complexes as reported below. More detailed modelling of the photogeneration of the Ni(I) complexes using 370 nm incident light is provided in Section S1.5.

Table S1. Summary of the optimized first-order rate constants for the [$\boldsymbol{A} \rightarrow \boldsymbol{B}$, $\boldsymbol{B} \rightarrow \boldsymbol{C}$] reaction model described previously[1] and the irradiation time to maximize the Ni(I) concentration.

Parent Ni(II) Complex	Ni(I) Complex	k_p (x10^{-2} min^{-1})	k_d (x10^{-2} min^{-1})	t (min)
Ni(II)($^{t\text{-Bu}}$bpy)(*o*-tolyl)Cl	**1-Cl**	4.1 ± 0.4	0.70 ± 0.03	52
Ni(II)($^{t\text{-Bu}}$bpy)(*o*-tolyl)Br	**1-Br**	8.1 ± 0.8	0.26 ± 0.09	44
Ni(II)($^{t\text{-Bu}}$bpy)(*o*-tolyl)I	**1-I**	7.7 ± 0.3	0.08 ± 0.01	60
Ni(II)(bpy)(*o*-tolyl)Cl	**2-Cl**	3.3 ± 0.5	0.5[b]	67
Ni(II)(^{MeOOC}bpy)(*o*-tolyl)Cl	**3-Cl**	15.0 ± 0.8	0.27 ± 0.06	27

[a]Data for **1-I** are given in Supporting Information Section S1.5. [b]No value for k_d was found for **2-Cl**, so we have approximated it as 0.5 x10^{-2} M^{-1} min^{-1}, i.e., an intermediate value between **1-Cl** and **3-Cl**.

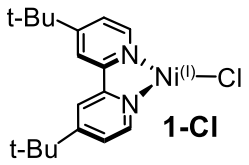

1-Cl

Ni(I)($^{t\text{-Bu}}$bpy)Cl, **1-Cl**. Air- and moisture-free irradiation of the parent Ni(II) compound, Ni(II)($^{t\text{-Bu}}$bpy)(*o*-tolyl)Cl, for t = ~ 50 minutes afforded the title compound. UV-vis (THF): λ_1 = 660 nm (15,152 cm^{-1}), λ_2 = 422 nm, (23,700 cm^{-1}). EPR (2-MeTHF, T = 5 K, frequency = 9.637 GHz, power = 2.2 mW, modulation amplitude = 8 G): g_z = 2.248, g_x = 2.050, g_y = 2.070, g_{iso} = 2.123.

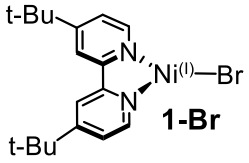

1-Br

Ni(I)($^{t\text{-Bu}}$bpy)Br, **1-Br**. Air- and moisture-free irradiation of the parent Ni(II) compound, Ni(II)($^{t\text{-Bu}}$bpy)(*o*-tolyl)Br, for t = ~ 45 minutes, afforded the title compound. UV-vis (THF): λ_1 = 653 nm (15,314 cm^{-1}), λ_2 = 386 nm, (25,906 cm^{-1}). EPR (2-MeTHF, T = 5 K, frequency = 9.637 GHz, power = 2.2 mW, modulation amplitude = 8 G): g_z = 2.255, g_x =2.042, g_y = 2.079, g_{iso} = 2.125.

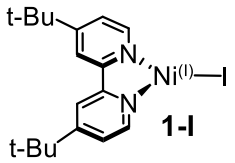

1-I

Ni(I)($^{t\text{-Bu}}$bpy)I, **1-I**. Air- and moisture-free irradiation of the parent Ni(II) compound, Ni(II)($^{t\text{-Bu}}$bpy)(*o*-tolyl)I, for t = ~ 45 minutes, afforded the title compound. Note that while the modelling (Table S1) predicts t = 60 min, we used the same irradiation time as for **1-Br** because of the similarities in the experimentally observed rate constants (Table S2). UV-vis (THF): λ_1 = 640 nm (15,625 cm^{-1}), λ_2 = 382 nm, (26,178 cm^{-1}). EPR (2-MeTHF, T = 5 K, frequency = 9.646 GHz, power = 2.2 mW, modulation amplitude = 8 G): g_z = 2.370, g_x = 2.044, g_y = 2.075, g_{iso} = 2.163.

2-Cl

Ni(I)(bpy)Cl, **2-Cl.** Air- and moisture-free irradiation of the parent Ni(II) compound, Ni(II)(bpy)(*o*-tolyl)Cl, for t = ~ 70 minutes, afforded the title compound. UV-vis (THF): λ_1 = 673 nm (15,625 cm^{-1}), λ_2 = 431 nm, (23,200 cm^{-1}). Sufficiently high concentration samples of **2-Cl** were precluded at low temperature (see Section S1.9). As such, no low temperature EPR signal could be resolved experimentally.

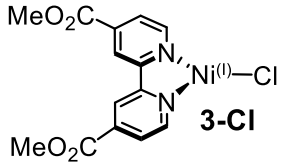

3-Cl

Ni(I)(^{MeOOC}bpy)Cl, **3-Cl.** Air- and moisture-free irradiation of the parent Ni(II) compound, Ni(II)(^{MeOOC}bpy)(*o*-tolyl)Cl, for t = ~ 30 minutes, afforded the title compound. UV-vis (THF): λ_1 = 805 nm (12,422 cm^{-1}), λ_2 = 523 nm (19,120 cm^{-1}). EPR (2-MeTHF, T = 5 K, frequency = 9.637 GHz, power = 2.2 mW, modulation amplitude = 8 G): g_z = 2.217, g_x = 2.171, g_y = 2.195, g_{iso} = 2.194.

S1.4. Steady-State UV-vis Spectroscopy.

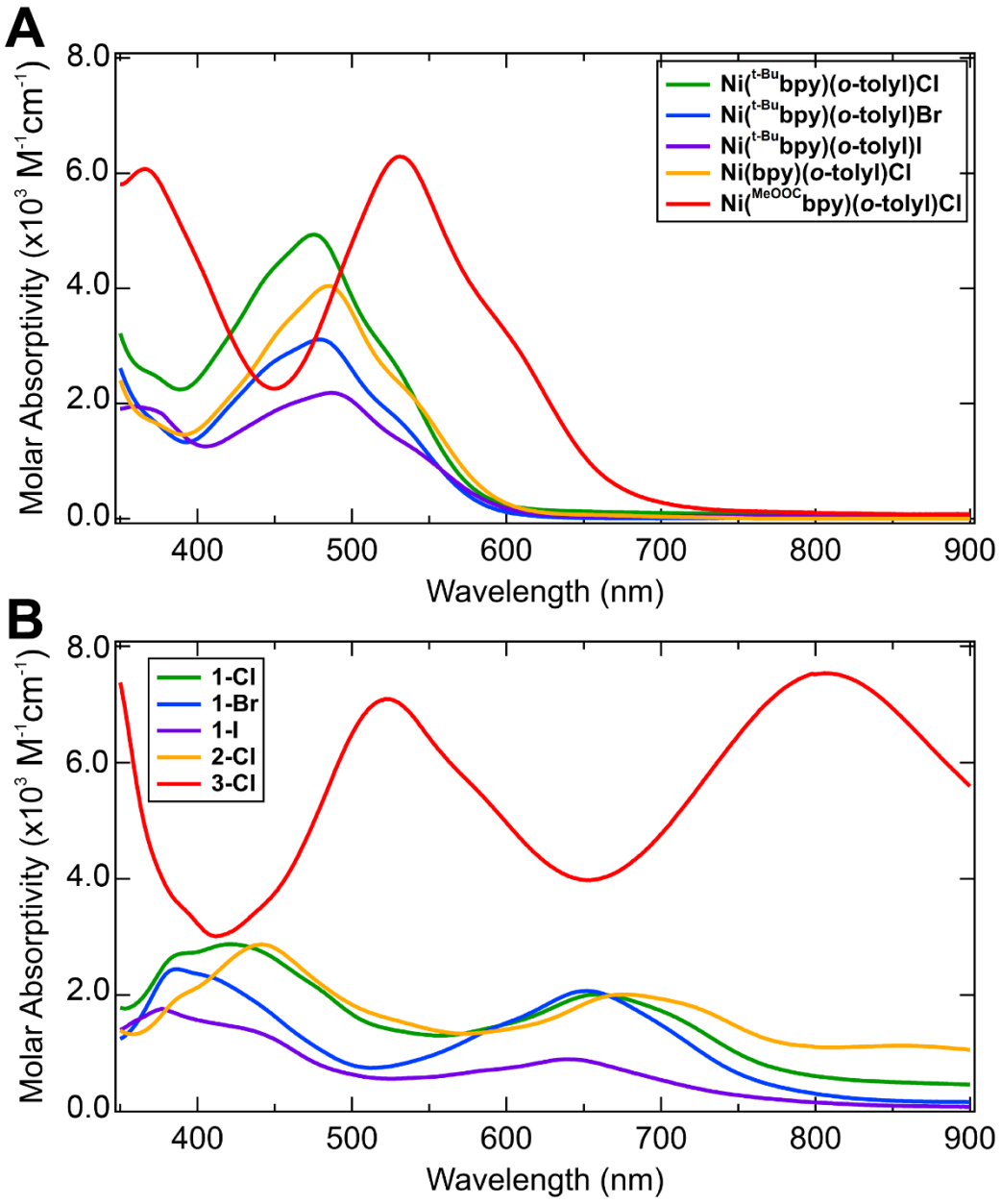

Figure S1. UV-vis spectra in THF on a wavelength scale of (A) the parent Ni(II)–bpy aryl halides and (B) the photogenerated Ni(I)–bpy halides examined in this work. Molar absorptivity assignments based on Matlab kinetic simulations reported in Supporting Information Section S1.5.

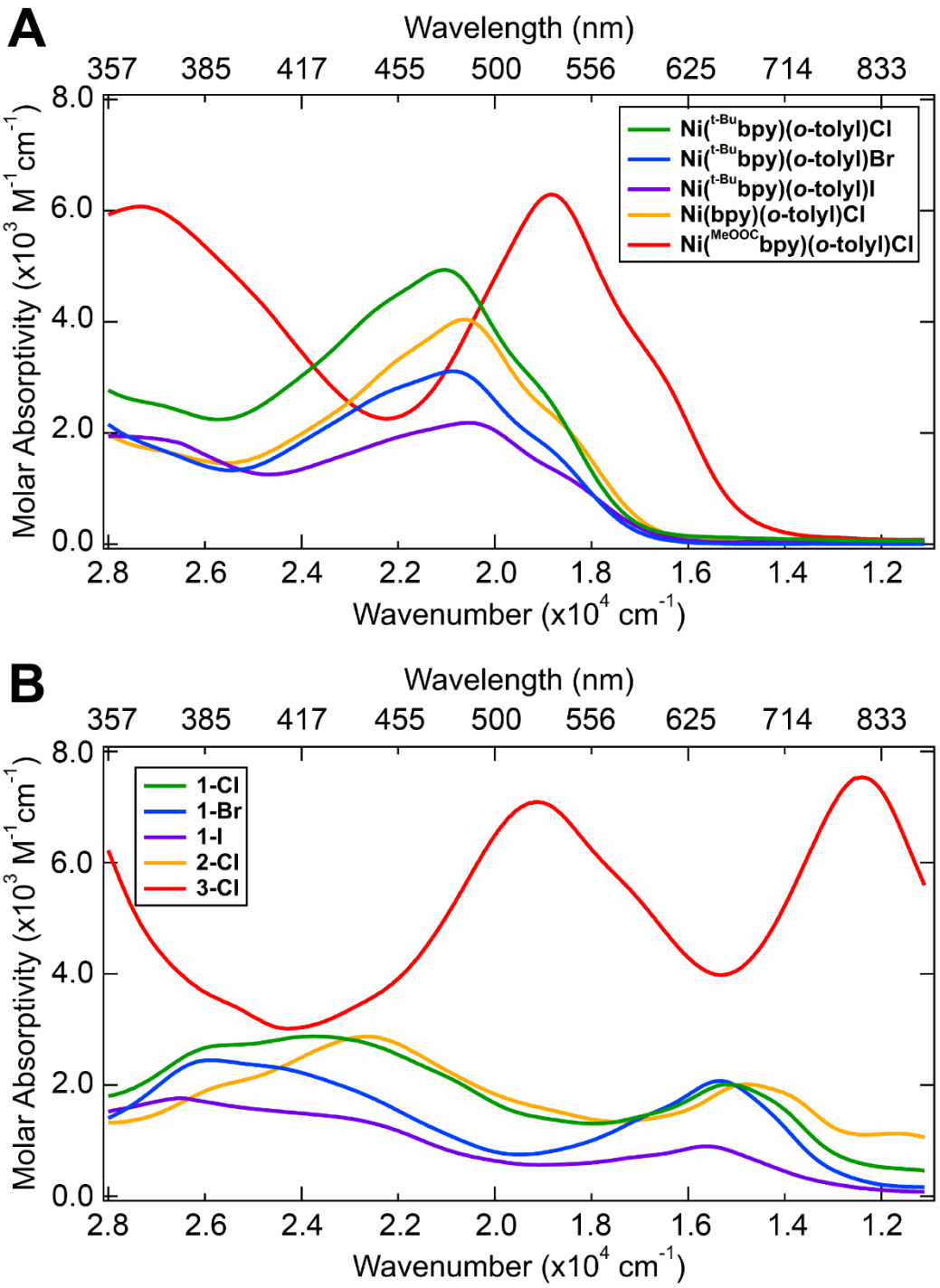

Figure S2. UV-vis spectra in THF on a wavenumber scale of (A) the parent Ni(II)–bpy aryl halides and (B) the photogenerated Ni(I)–bpy halides examined in this work. Molar absorptivity assignments based on Matlab kinetic simulations reported in Supporting Information Section S1.5.

S1.5. Experimental Photolysis Kinetics, Quantum Yields, and Global Kinetic Modeling.

Experimental Photolysis Kinetics.

Quantification of the photolysis kinetics of the Ni(II)–bpy aryl halide complexes upon irradiation with the Kessil PR160L LEDs (incident light wavelength = 370 nm, $\boldsymbol{P_{LED}}$ = 70 mW cm^{-2} at a 5 cm distance) afforded the first-order rate constants, $k_{obs,1}$ for the decomposition of the Ni(II) parent and $k_{obs,2}$ for the formation of the Ni(I)–bpy halide species.

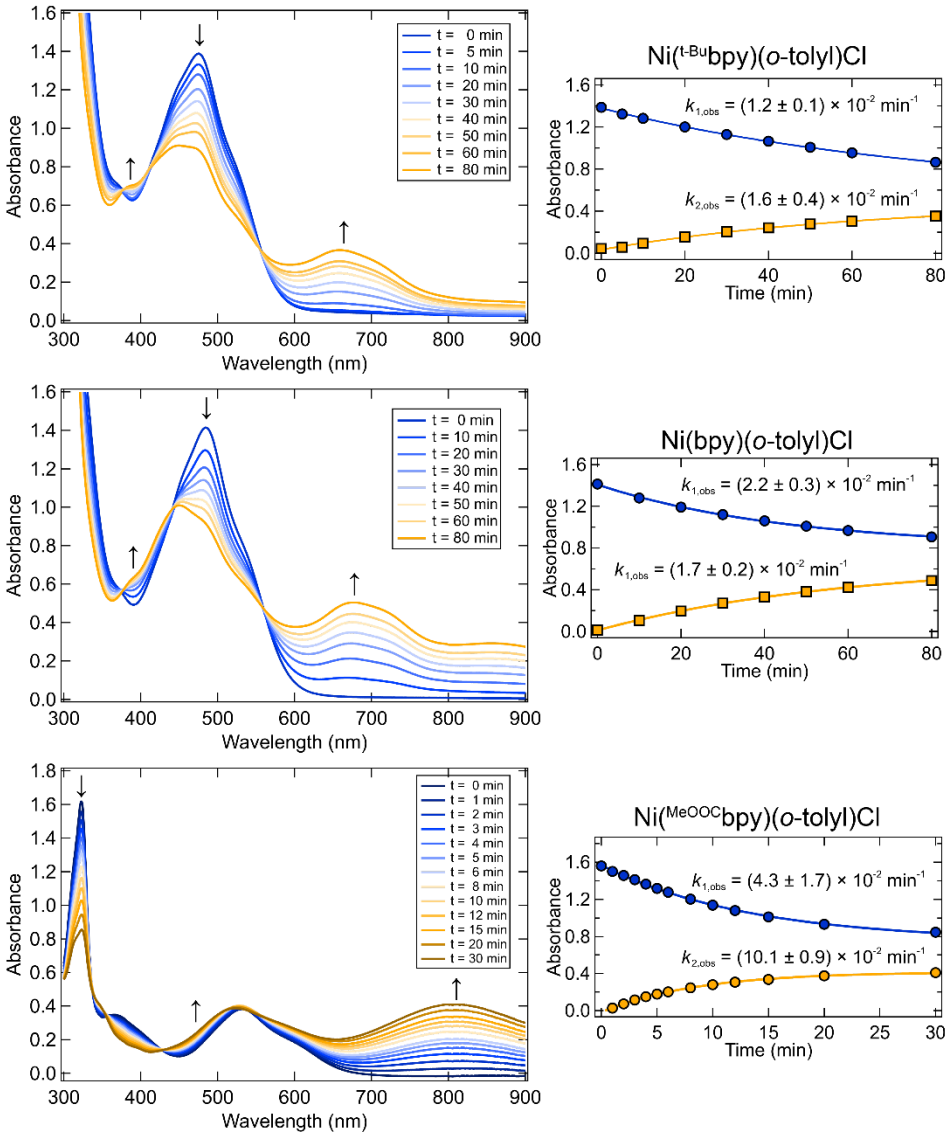

Figure S3. Photolysis profiles in THF using 370 nm excitation for the formation of **1-Cl**, **2-Cl**, and **3-Cl** from their respective Ni(II)–bpy aryl halide parent complexes. Photolysis kinetics were monitored at wavelengths indicated by the arrows in each panel. Side panels correspond to the fitted kinetic data (blue curve for the decay of the starting material, orange curve for the formation of the new species). Data were fit using a single exponential; error bars are one standard deviation.

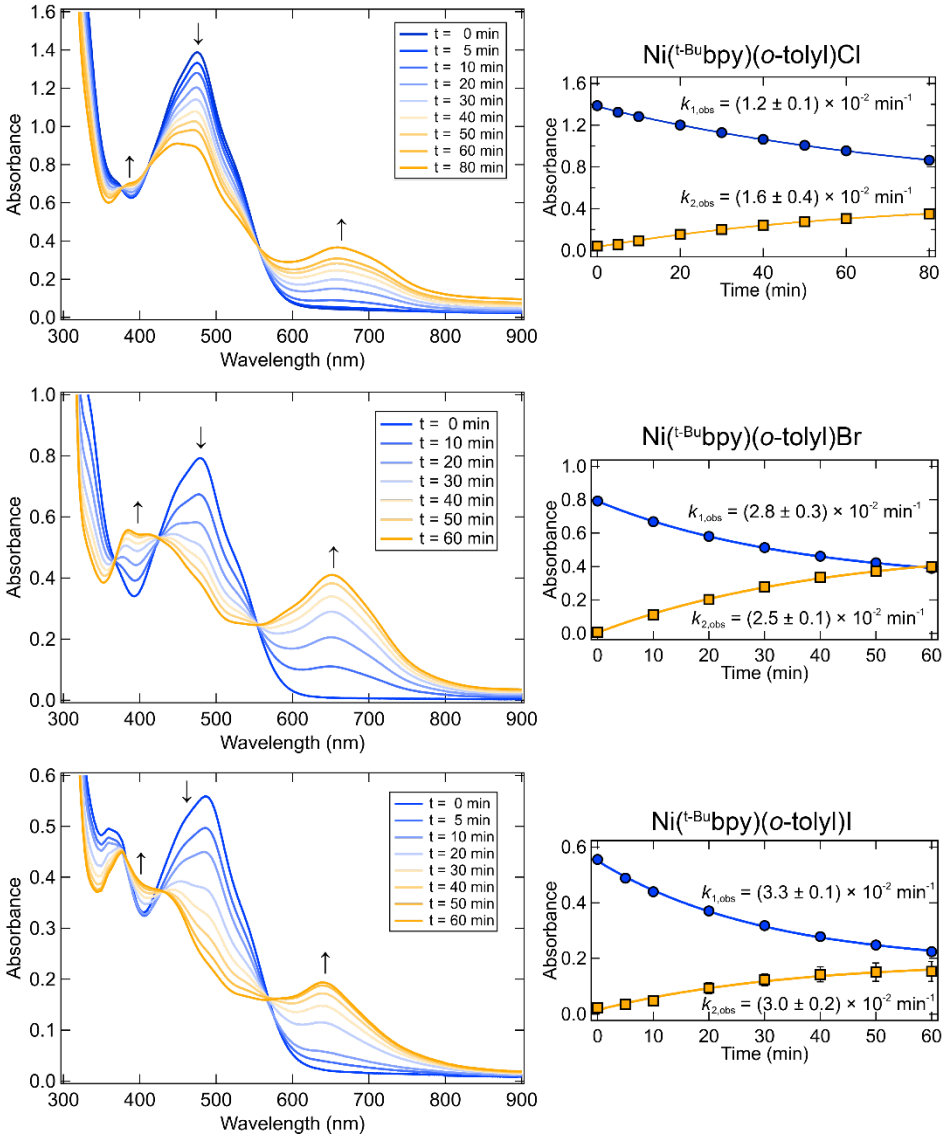

Figure S4. Photolysis profiles in THF using 370 nm excitation for the formation of **1-Cl**, **2-Cl**, and **3-Cl** from their respective Ni(II)–bpy aryl halide parent complexes. Photolysis kinetics were monitored at wavelengths indicated by the arrows in each panel. Side panels correspond to the fitted kinetic data (blue curve for the decay of the starting material, orange curve for the formation of the new species). Data were fit using a single exponential; error bars are one standard deviation.

Experimental Quantum Yield Determination.

From these data, quantum yields (Φ) were calculated using the method developed by Gescheidt et al. following equation S7, where h is Planck's constant, c is the speed of light in a vacuum, N_A is Avogadro's constant, V is the volume of the reactant solution irradiated (in liters), λ is the primary wavelength of the light source (in meters), and P_{LED} is the power of the light source. The value of the rate constant $k_{obs,1}$ was taken from the data above and the concentration of the Ni(II) parent was determined by Beer's Law analysis. Note that the value, Abs_{NiC}^{370}, is the measured absorbance of the reactant solution at the primary light source wavelength, 370 x10^{-9} m.

$$\Phi = \frac{hcN_aV}{\lambda P_{LED}} \frac{k_1[\mathrm{Ni}]}{1-10^{-Abs_{\mathrm{NiC}}^{370}}} \qquad \textbf{(eq. S7)}$$

As noted in our previous report, the absolute quantum yield determination by equation S7 is reliant on an accurate measurement of the power of the light source used. We found that the power of our Kessil PR160L 370 nm LED is 70 mW cm^{-2} when measured by a Thorlabs S425C thermal detector power meter 5 cm away from the light source. Utilizing a constant volume of 0.0025 L in each cuvette gives an irradiation surface area of 2.5 cm^2, and accordingly, we found our P_{LED} = 175 mW.

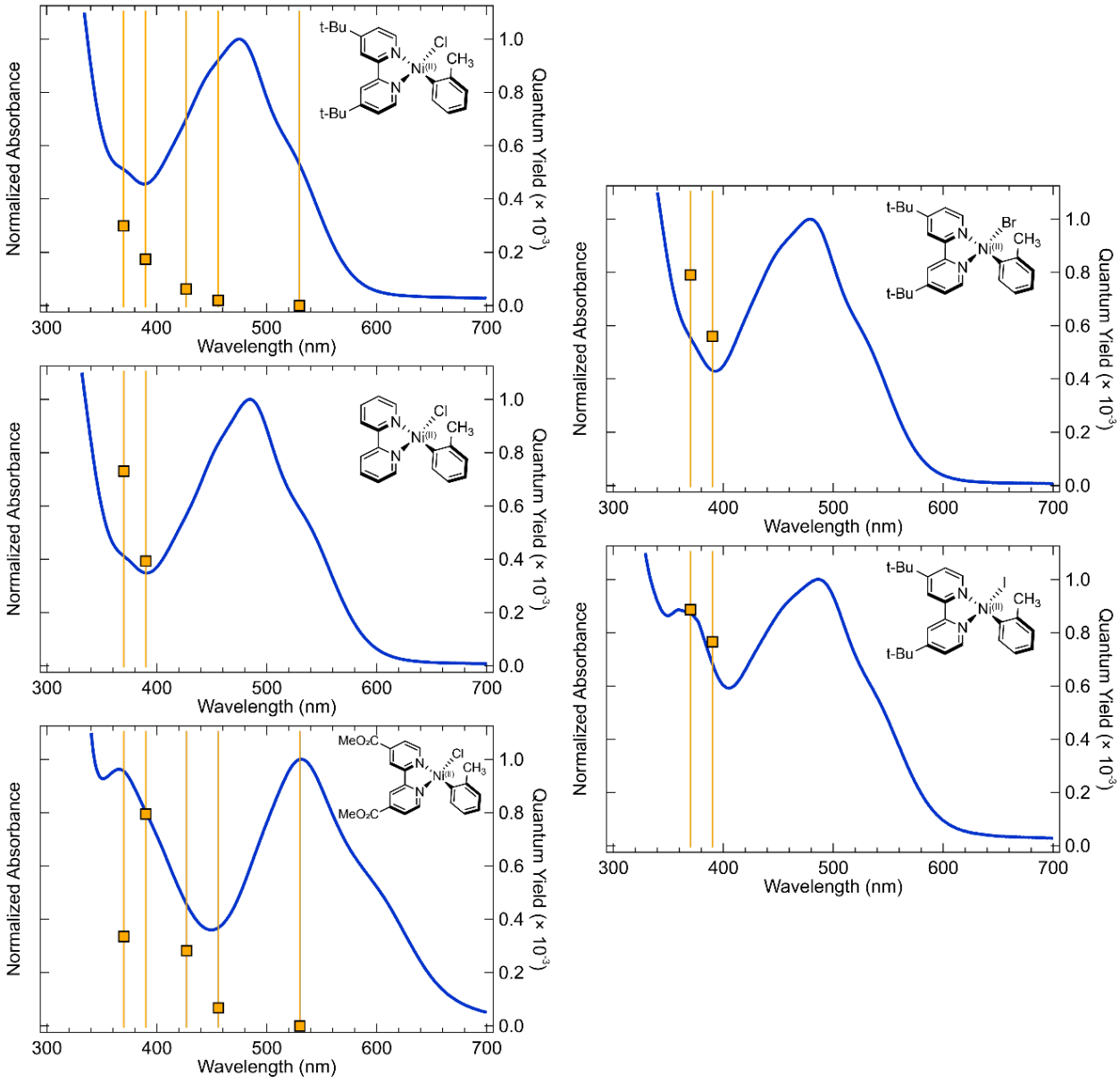

Figure S5. Wavelength-dependent quantum yields for the photolysis of the parent Ni(II) complexes in THF using 370 nm light. Some data from incident light wavelengths 390 nm, 427 nm, 456 nm, and 525 nm was taken from reference 1. In all cases, save for Ni(II)($^{\mathrm{MeOOC}}$bpy)(*o*-tolyl)Cl, $\Phi_{370\ \mathrm{nm}} > \Phi_{390\ \mathrm{nm}}$.

Global Kinetic Modeling.

We note that the single wavelength exponential fits used above may contain spectral overlap of the starting material and the photolysis product. Additionally, they cannot explain differences between $k_{obs,1}$ and $k_{obs,2}$. Consequently, we can further model the process given in **Scheme S1** as a sequential reaction involving the conversion of **A** to **C** via an intermediate species, **B**, i.e., [$\boldsymbol{A} \rightarrow \boldsymbol{B}$, $2\boldsymbol{B} \rightarrow \boldsymbol{C}$], following our previously described analysis using in-house Matlab scripts patterned after established programs.[1] From these data (Figures S6-S10) we find that the [$\boldsymbol{A} \rightarrow \boldsymbol{B}$, $2\boldsymbol{B} \rightarrow \boldsymbol{C}$] model agrees very well with the experimental photolysis profiles, we are able to deconvolute the absorbance spectra of the formed Ni(I) species, and we find little to no Ni(I) decomposition product formed in the samples upon irradiation at room temperature (more analysis on the thermal decomposition of the Ni(I) species in Supporting Information Section S1.8, Thermodynamics Experiments and Eyring Analysis).

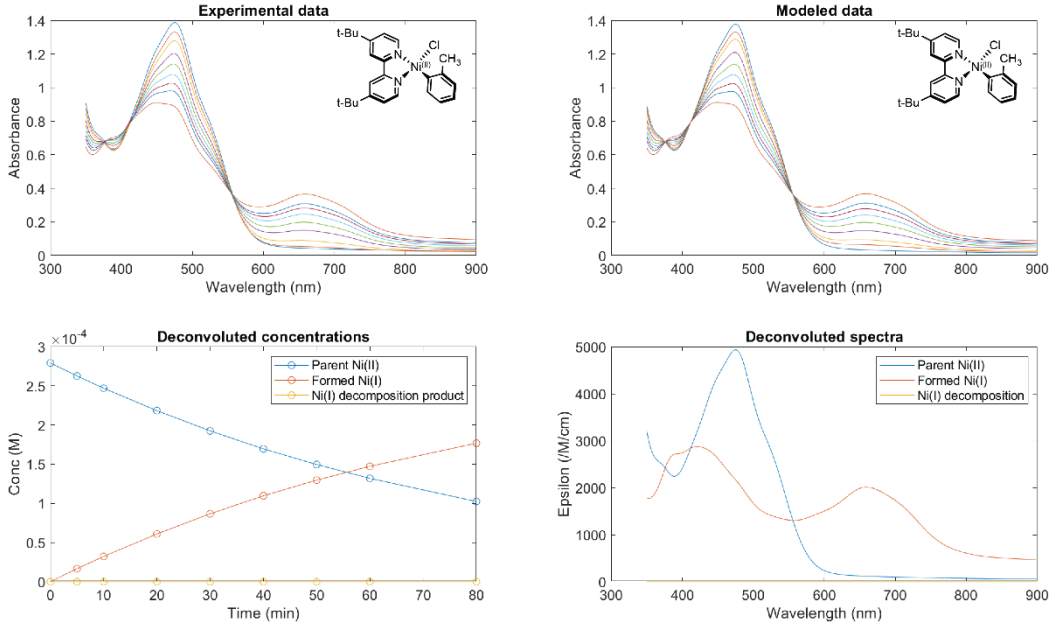

Figure S6. Kinetic global fitting for parent compound Ni(II)($^{t\text{-Bu}}$bpy)(*o*-tolyl)Cl. *Top left:* Raw experimental absorbance data. *Top right:* absorbance data reproduced by the [$\boldsymbol{A} \rightarrow \boldsymbol{B}$, $2\boldsymbol{B} \rightarrow \boldsymbol{C}$] kinetic model. *Bottom left*: concentration profiles of each chemical species as a function of photolysis time. *Bottom right:* deconvoluted molar absorptivity spectra for each chemical species. Absorptivity of the Ni(I) decomposition product is set to zero. Root-mean-square of the residuals = 5.0×10^{-3}.

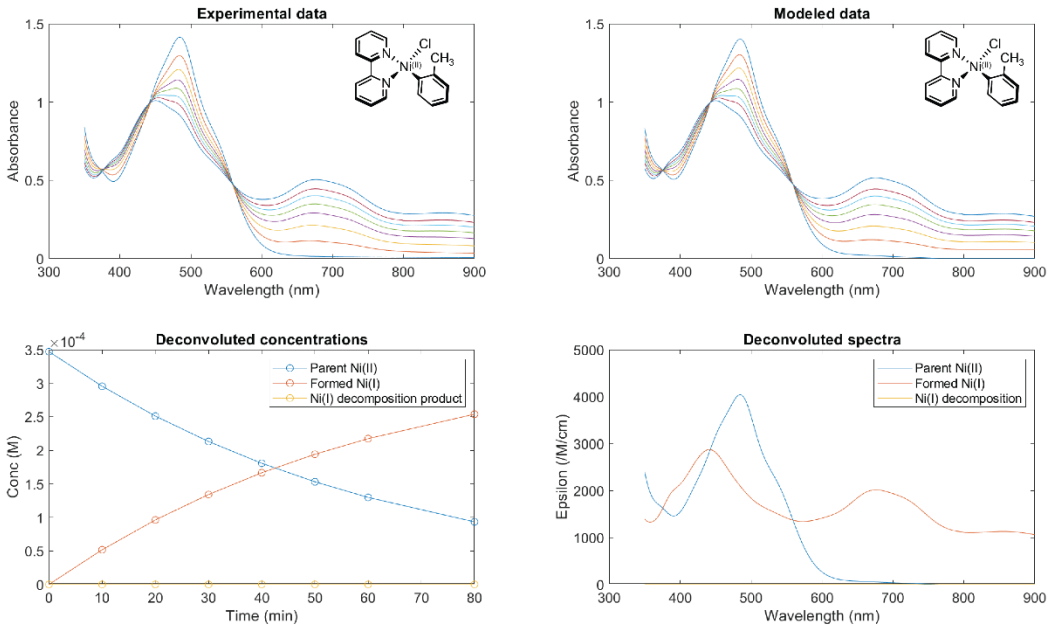

Figure S7. Kinetic global fitting for parent compound Ni(II)(bpy)(*o*-tolyl)Cl. *Top left:* Raw experimental absorbance data. *Top right:* absorbance data reproduced by the [$\boldsymbol{A} \rightarrow \boldsymbol{B}$, $2\boldsymbol{B} \rightarrow \boldsymbol{C}$] kinetic model. *Bottom left*: concentration profiles of each chemical species as a function of photolysis time. *Bottom right:* deconvoluted molar absorptivity spectra for each chemical species. Absorptivity of the Ni(I) decomposition product is set to zero. Root-mean-square of the residuals = 8.5×10^{-3}.

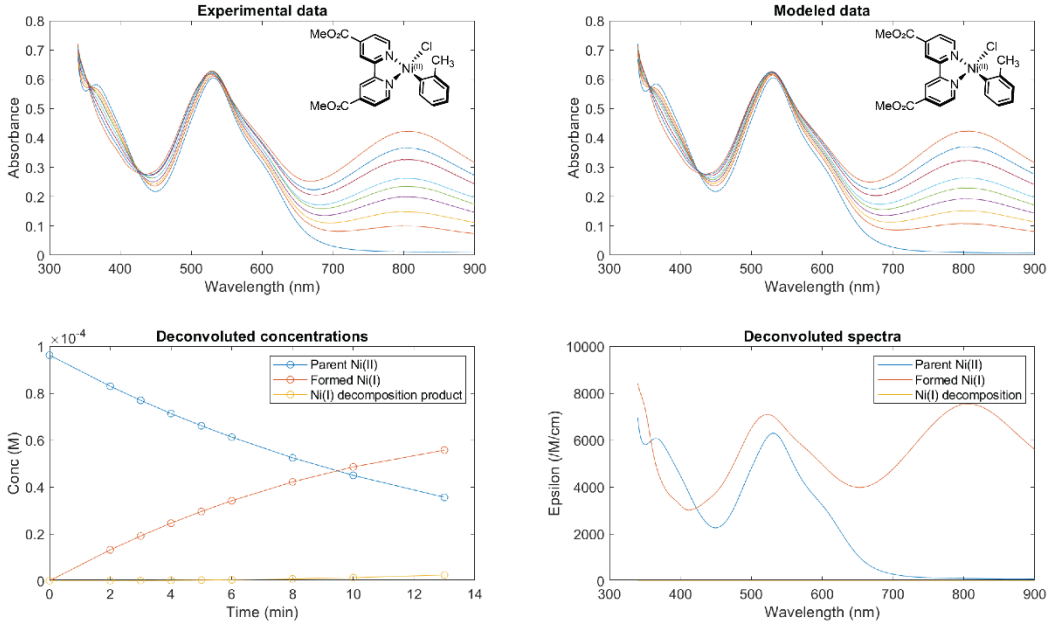

Figure S8. Kinetic global fitting for parent compound Ni(II)(^{MeOOC}bpy)(*o*-tolyl)Cl. *Top left:* Raw experimental absorbance data. *Top right:* absorbance data reproduced by the [$\boldsymbol{A} \rightarrow \boldsymbol{B}$, $2\boldsymbol{B} \rightarrow \boldsymbol{C}$] kinetic model. *Bottom left*: concentration profiles of each chemical species as a function of photolysis time. *Bottom right:* deconvoluted molar absorptivity spectra for each chemical species. Absorptivity of the Ni(I) decomposition product is set to zero. Root-mean-square of the residuals = 3.5×10^{-3}.

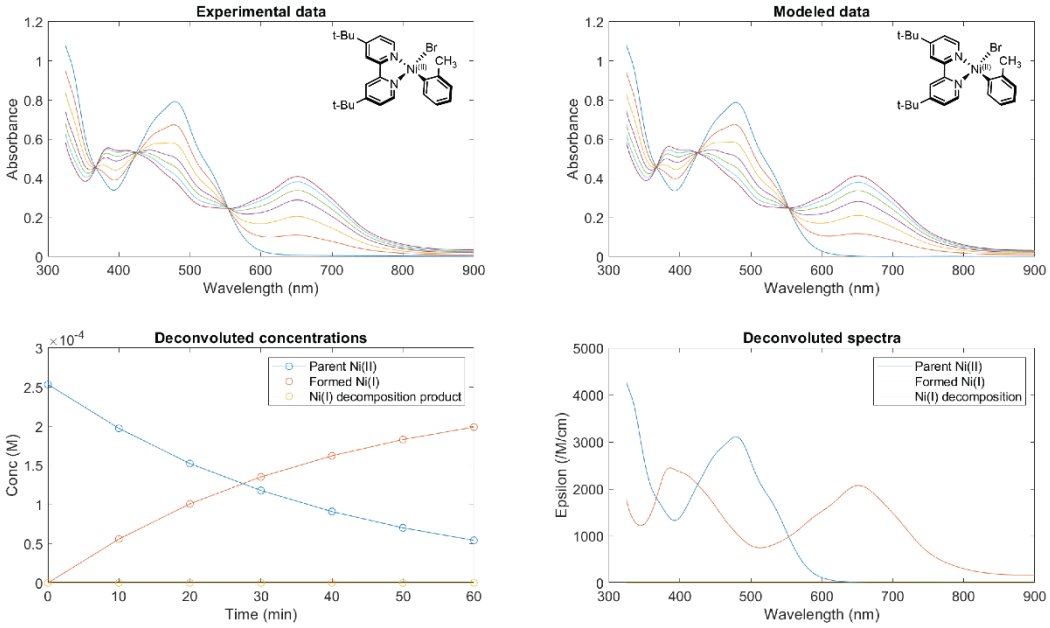

Figure S9. Kinetic global fitting for compound parent compound Ni(II)($^{t\text{-Bu}}$bpy)(*o*-tolyl)Br. *Top left:* Raw experimental absorbance data. *Top right:* absorbance data reproduced by the [$\boldsymbol{A} \rightarrow \boldsymbol{B}$, $2\boldsymbol{B} \rightarrow \boldsymbol{C}$] kinetic model. *Bottom left*: concentration profiles of each chemical species as a function of photolysis time. *Bottom right:* deconvoluted molar absorptivity spectra for each chemical species. Absorptivity of the Ni(I) decomposition product is set to zero. Root-mean-square of the residuals = 3.3×10^{-3}.

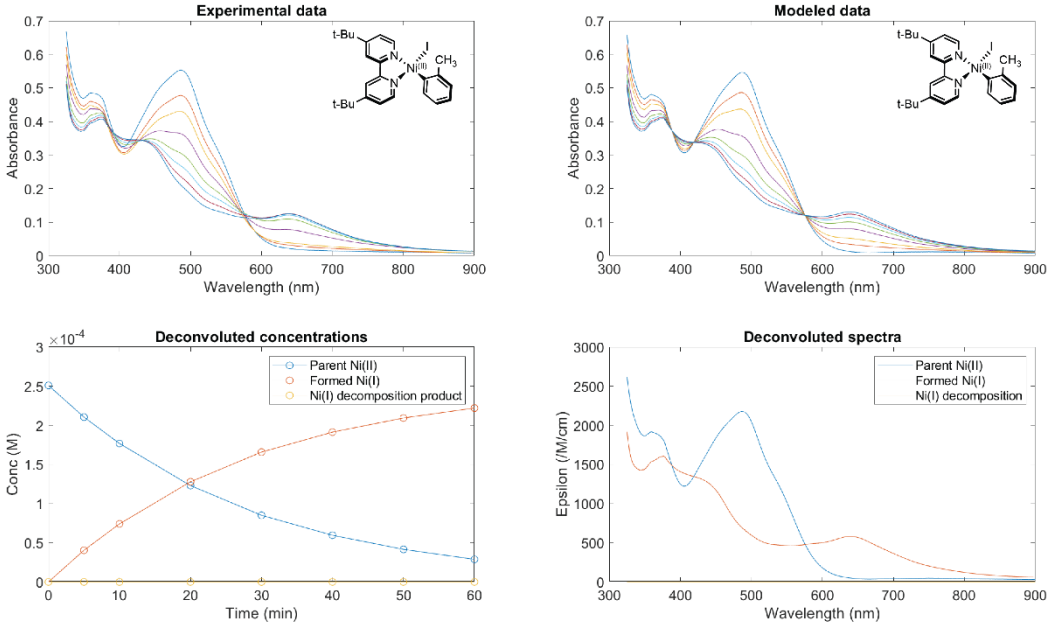

Figure S10. Kinetic global fitting for parent compound Ni(II)($^{t\text{-Bu}}$bpy)(*o*-tolyl)I. *Top left:* Raw experimental absorbance data. *Top right:* absorbance data reproduced by the [$\boldsymbol{A} \rightarrow \boldsymbol{B}$, $2\boldsymbol{B} \rightarrow \boldsymbol{C}$] kinetic model. *Bottom left*: concentration profiles of each chemical species as a function of photolysis time. *Bottom right:* deconvoluted molar absorptivity spectra for each chemical species. Absorptivity of the Ni(I) decomposition product is set to zero. Root-mean-square of the residuals = 4.7×10^{-3}.

Table S2. Tabulated experimental kinetics and quantum yields for the photolysis of the parent Ni(II)–bpy aryl halides to form the Ni(I)–bpy halide complexes. Some data at 390 nm incident light taken from reference 1 for comparison purposes.

Parent Ni(II) Compound	$k_{obs,1}$ **(370 nm)** **(×10^{-2} min^{-1})**	$k_{obs,2}$ **(370 nm)** **(×10^{-2} min^{-1})**	Φ_{370} **(×10^{-3})**	$k_{obs,1}$ **(390 nm)** **(×10^{-2} min^{-1})**	$k_{obs,2}$ **(390 nm)** **(×10^{-2} min^{-1})**	Φ_{390} **(×10^{-3})**
Ni(II)($^{t\text{-Bu}}$bpy)(*o*-tolyl)Cl	1.2 ± 0.1	1.6 ± 0.4	0.30	2.5 ± 0.2	7.6 ± 0.7	0.18
Ni(II)(bpy)(*o*-tolyl)Cl	2.2 ± 0.3	1.7 ± 0.2	0.73	3.6 ± 0.6	2.9 ± 0.3	0.39
Ni(II)(^{MeOOC}bpy)(*o*-tolyl)Cl	4.3 ± 1.7	10.1 ± 0.9	0.34	17.0 ± 0.7	10.1 ± 3.9	0.86
Ni(II)($^{t\text{-Bu}}$bpy)(*o*-tolyl)Br	2.8 ± 0.3	2.5 ± 0.1	0.79	6.9 ± 0.4	9.2 ± 0.7	0.56
Ni(II)($^{t\text{-Bu}}$bpy)(*o*-tolyl)I	3.3 ± 0.1	3.0 ± 0.2	0.89	6.9 ± 0.4	9.2 ± 0.7	0.77

Table S3. Optimized rate constants for the [$\boldsymbol{A \rightarrow B}$, $\boldsymbol{2B \rightarrow C}$] reaction model. Note that k_p is analogous to $k_{obs,1}$ from the experimental dataset using Kessil PR160L 370 nm LEDs as incident light source. Root-mean-square of the residuals = RMSR.

Parent Ni(II) Compound	$\boldsymbol{k_p}$ **[$A \rightarrow B$] (×10^{-2} min^{-1})**	***RMSR***
Ni(II)($^{t\text{-Bu}}$bpy)(*o*-tolyl)Cl	1.4 ± 0.1	5.0×10^{-3}
Ni(II)(bpy)(*o*-tolyl)Cl	1.5 ± 0.1	8.5×10^{-3}
Ni(II)(^{MeOOC}bpy)(*o*-tolyl)Cl	9.2 ± 1.2	3.5×10^{-3}
Ni(II)($^{t\text{-Bu}}$bpy)(*o*-tolyl)Br	2.6 ± 0.1	3.3×10^{-3}
Ni(II)($^{t\text{-Bu}}$bpy)(*o*-tolyl)I	1.5 ± 0.1	4.7×10^{-3}

S1.6. Electrochemical Studies.

Cyclic Voltammetry.

Room temperature cyclic voltammetry was performed in a nitrogen-filled glove box with a Gamry Reference 600 or Biologic SP-200 potentiostat using a three-electrode cell. We used a 3 mm diameter glassy carbon working electrode with an effective surface area of 0.0877 cm^2 (CH Instruments), a 0.01 M $Ag^{+/0}$ in 0.1 M $TBAPF_6$ in acetonitrile quasi-reference electrode (Bioanalytical Systems, Inc.), and a platinum wire counter electrode (Kurt J. Lesker). Potentiostatic electrochemical impedance spectra (PEIS) were recorded to obtain Nyquist plots to determine the uncompensated resistance. Of the uncompensated resistance, 95% was accounted for using electronic compensation.

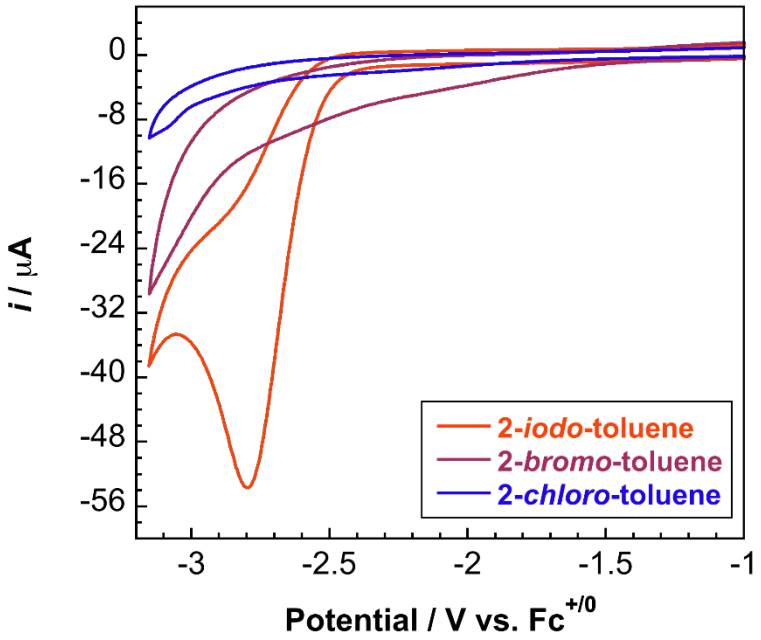

Figure S11. Cyclic voltammetry of 1.0 mM 2-*chloro*-toluene, 2-*bromo*-toluene, and 2-*iodo*-toluene on glassy carbon in THF solution with 0.2 M $TBAPF_6$ electrolyte. All scans taken at 100 mV s^{-1} and referenced to $Fc^{+/0}$. Reduction of 2-*chloro*-toluene is experimentally found to be less than –3.2 V vs $Fc^{+/0}$.

Spectroelectrochemistry Analysis.

Spectroelectrochemistry was performed in a nitrogen-filled glove box with a Gamry Reference 600 or Biologic SP-200 potentiostat. Measurements were performed with a quartz spectroelectrochemical cell with a 0.17 cm path length from Pine Research Instrumentation (AKSTCKIT3), a 0.01 M $Ag^{+/0}$ in 0.1 M $TBAPF_6$ in acetonitrile quasi-reference electrode (Bioanalytical Systems, Inc.), a gold honeycomb electrode (Pine Instruments), and a platinum wire counter electrode (Kurt J. Lesker). Potentiostatic electrochemical impedance spectra (PEIS) were recorded to obtain Nyquist plots to determine the uncompensated resistance. 95% of the uncompensated resistance was accounted for using electronic compensation. Measurements were recorded using a StellarNet SL4 deuterium-tungsten UV-vis-NIR light source coupled to StellarNet Black Comet UV-vis and DWARF-Star NIR spectrometers.

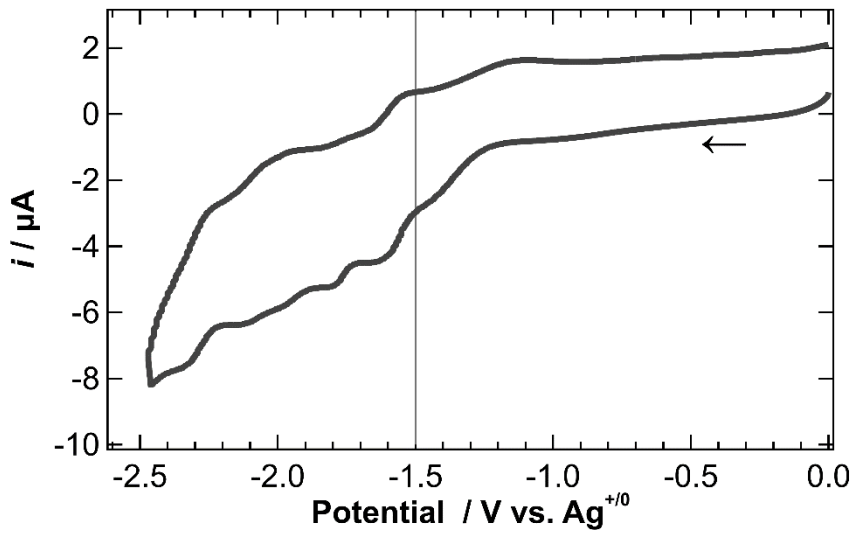

Figure S12. Cyclic voltammetry (as performed in the spectroelectrochemical cell) of 0.67 mM Ni(II)($^{t\text{-Bu}}$bpy)Cl_2 in THF solution with 0.44 M $TBAPF_6$ at a scan rate of 20 mV s^{-1}. Vertical line is the potential where the spectroelectrochemistry data were collected.

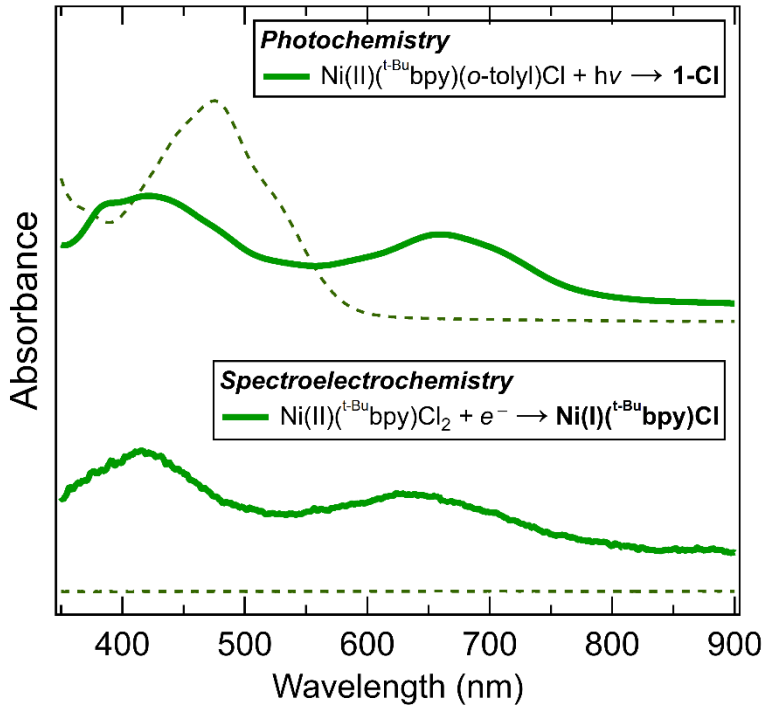

Figure S13. *Top*: UV-vis spectrum for the photochemical preparation of **1-Cl** (solid green line) from its Ni(II)–bpy aryl halide (dashed lines) parent using a 370 nm LED. *Bottom*: Spectroelectrochemistry of 0.67 mM Ni(II)($^{t\text{-Bu}}$bpy)Cl_2 (dashed lines) forming Ni(I)($^{t\text{-Bu}}$bpy)Cl (solid green line) in THF solution with 0.44 M $TBAPF_6$. Spectrum recorded after ten minutes of electrolysis at −1.5 V vs. $Ag^{+/0}$, which corresponds to a potential slightly negative of the first reduction. The slight blue-shift of the electrochemically produced Ni(I) spectrum versus **1-Cl** is most likely due to the high electrolyte concentration. Reproduced from Figure 2B of the main text.

S1.7. Oxidative Addition Experiments.

Steady-state Ni(I)–bpy halide reactivity by UV-vis.

We sought to gauge the oxidative addition reactivity of the photogenerated Ni(I)–bpy halide species. To achieve this, in the glove box we prepared solutions of the parent Ni(II)–bpy aryl halide complexes such that their primary MLCT absorption peak was ~1.0 absorbance (affording ~10^{-4} M solutions, V = 3.0 mL, solvent = THF). These solutions were transferred to air-free quartz cuvettes (10 mm) and irradiated using Kessil PR160L LEDs with incident light wavelength = 370 nm. In all cases, the Ni(I)–bpy halide peak was present. We returned the cuvettes to the glove box, opened them, and introduced 0.2 mL of aryl–halides of increasing C(sp^2)–X bond strengths (X = Cl, Br, I). In all cases, except **3-Cl** with 2-*chloro*-toluene, the Ni(I) absorbance feature was quenched (Figure S14-S15).

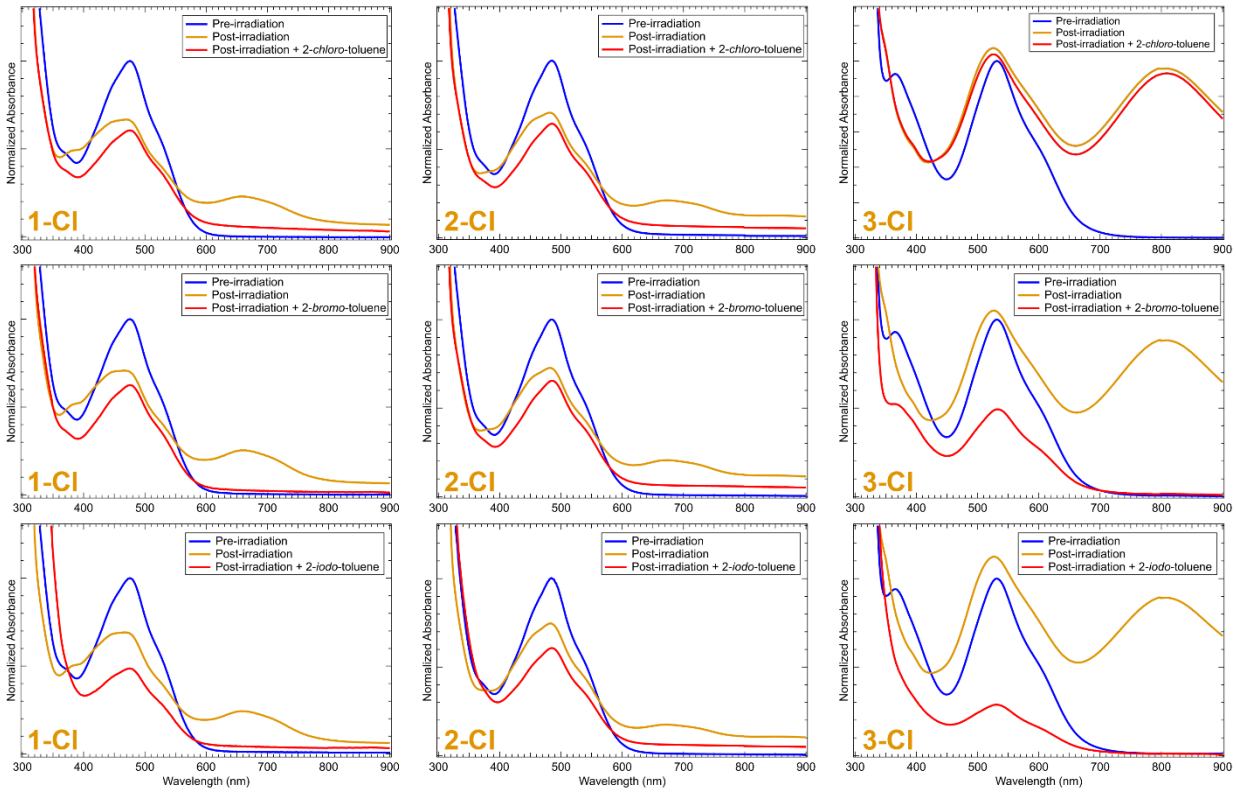

Figure S14. UV-vis absorption spectra of the oxidative addition studies done on the bpy series, **1-Cl** (left column), **2-Cl** (center column), and **3-Cl** (right column) by adding in molar excess (0.2 mL) aryl halide: 2-*chloro*-toluene (top row), 2-*bromo*-toluene (center row), or 2-*iodo*-toluene (bottom row). Note that complex **3-Cl** does not react with 2-*chloro*-toluene. Blue line is the parent Ni(II)–bpy aryl halide complex before irradiation, orange line is the photogenerated Ni(I)–bpy halide, and the red line is upon addition of the aryl halide. The data post-addition of aryl halide depict unreacted and newly generated parent four-coordinate Ni(II)–bpy aryl halide. Solvent = THF; initial solution volume = 3.0 mL, incident light wavelength = 370 nm.

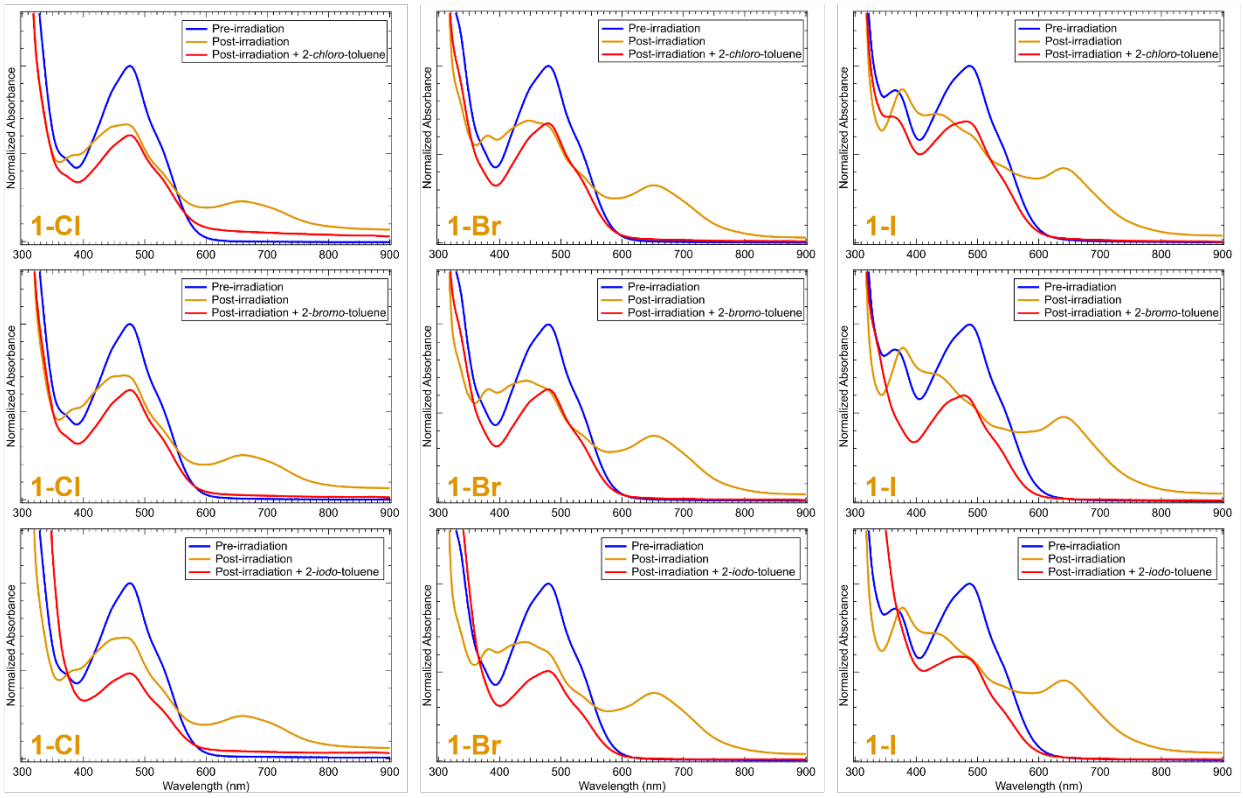

Figure S15. UV-vis absorption spectra of the oxidative addition studies done on the halide series, **1-Cl** (left column), **1-Br** (center column), and **1-I** (right column) in THF by adding in excess (0.2 mL) aryl halide: 2-*chloro*-toluene (top row), 2-*bromo*-toluene (center row), or 2-*iodo*-toluene (bottom row). Blue line is the parent Ni(II)–bpy aryl halide complex before irradiation, orange line is the photogenerated Ni(I)–bpy halide, and the red line is upon addition of the aryl halide. The data post-addition of aryl halide depict unreacted and newly generated parent four-coordinate Ni(II)–bpy aryl halide. Solvent = THF; initial solution volume = 3.0 mL, incident light wavelength = 370 nm.

Steady-state Ni(I)–bpy halide reactivity by NMR.

In an effort to confirm the reactivity of the Ni(I)–bpy halides towards 2-*chloro*-toluene, we selected the representative complex, **1-Cl** to examine further by NMR. In the glove box, we dissolved 5.0 mg of Ni(II)($^{t\text{-Bu}}$bpy)(*o*-tolyl)Cl in 2.0 mL of d_8-THF (5.5 mM parent Ni(II)). Of this solution, 500 µL (2.8 µmol parent Ni(II)) was transferred to a J-Young NMR tube by microsyringe for ^{1}H NMR analysis (blue data in Figure S16, pre-irradiation). The remaining 1.5 mL of solution was transferred to an air-tight cuvette, removed from the glove box, and irradiated to generate the Ni(I) species, **1-Cl**. The cuvette was then reintroduced to the glove box and another 500 µL was removed for ^{1}H NMR analysis (green data in Figure S16, post-irradiation). To a third J-Young tube, 3.0 µL of a 0.92 M solution of 2-*chloro*-toluene in d_8-THF (2.8 µmol of 2-*chloro*-toluene) was added by microsyringe. A 500 µL aliquot of the irradiated Ni(I) solution was added to this same J-Young tube, rinsing down the sides of the tube to capture all of the aryl halide. This third tube was then taken for ^{1}H NMR analysis (red data in Figure S16, post-irradiation + [2-*Cl*-Tol]). Assuming all Ni(II) is converted to Ni(I), this amount of aryl halide added to the third tube represents one molar equivalent. However, given the incomplete irradiation, decay of the **1-Cl** complex over time, and errors induced by measuring small volumes in the glove box, the amount is > 1 eq by NMR.

From this analysis (Figure S16), we see the decrease in parent Ni(II)–bpy aryl halide peaks upon irradiation (blue to green data), and the regeneration of this parent complex after addition of 2-*chloro*-toluene (red data). However, the change is small and makes the interpretation of the ^{1}H NMR data difficult.

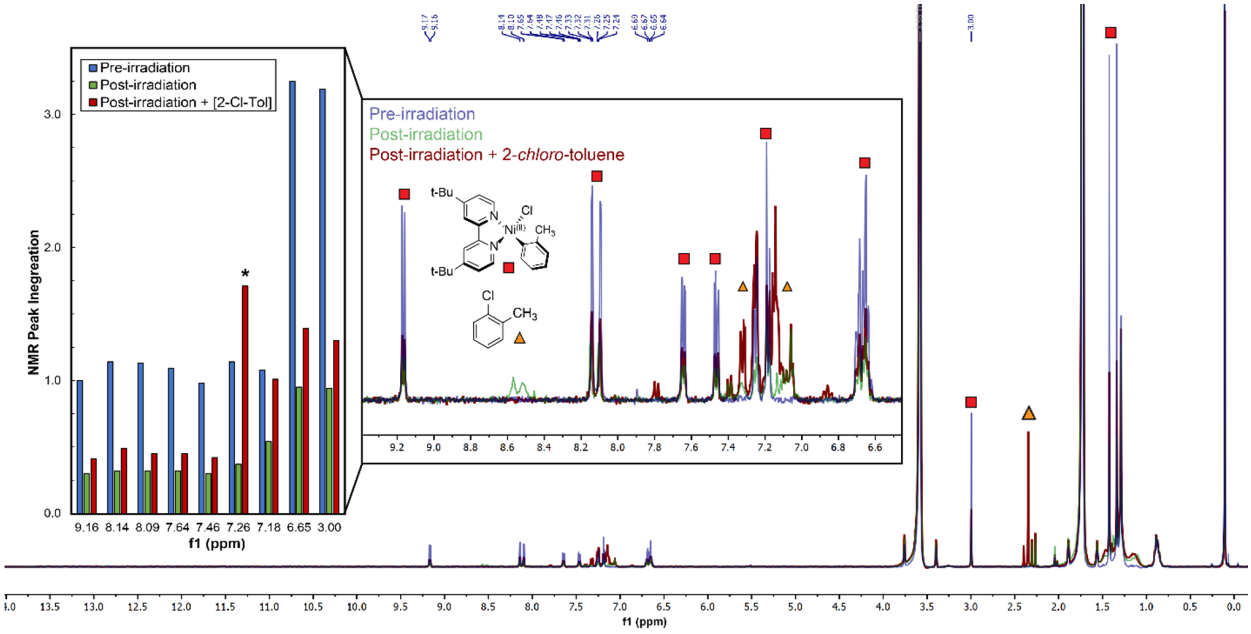

Figure S16. Oxidative addition study of **1-Cl** with ~ 1 eq. 2-*chloro*-toluene in d_8-THF. Red squares are the parent four-coordinate Ni(II)–bpy aryl halide, yellow triangles are the added 2-*chloro*-toluene. Regeneration of the parent complex after oxidative addition is seen in the integrated peaks, highlighted in the bar graph on the left (blue = pre-irradiation, green = post-irradiation, red = post-irradiation and addition of the aryl halide). The starred peak in the graph is large due to overlap with the aryl halide peaks. Aryl radical products (from the photolysis step) are seen near 2.4 ppm.

We turned to ^{19}F NMR for a clearer confirmation of the C(sp^2)–Cl oxidative addition reactivity of **1-Cl**. In the glove box, we dissolved 1.0 mg of Ni(II)($^{t\text{-Bu}}$bpy)(*o*-tolyl)Cl in 2.0 mL of d_8-THF (1.1 mM parent Ni(II)). Of this solution, 500 µL (0.6 µmol parent Ni(II)) was transferred to a J-Young NMR tube by microsyringe for ^{1}H NMR analysis (gray data in Figure S17, pre-irradiation).

The remaining solution was split in two: a 730 µL aliquot (0.8 µmol parent Ni(II)) was added to a 2 mm quartz air-tight cuvette (**C1**) along with 20 µL of d_8-THF, and, in another 2 mm quartz air-tight cuvette (**C2**), a second 730 µL aliquot of the solution was combined with 20 µL of 2-*chloro*-α,α,α-trifluorotoluene (0.15 mmol, ~193 molar equivalents relative to the parent Ni(II)). Both cuvettes, **C1** and **C2**, were removed from the glove box, simultaneously irradiated to generate **1-Cl**, then reintroduced to the glove box. From **C1**, 500 µL was removed into a J-Young for both ^{1}H NMR analysis (red data in Figure S17) and ^{19}F NMR analysis (Figure S18A, red data). The J-Young tube was then returned to the box and its sample recombined with the remaining solution from **C1**. To the full solution, 20 µL of 2-*chloro*-α,α,α-trifluorotoluene was added and mixed with a glass pipette; 500 µL was again removed for ^{19}F NMR analysis (Figure S18C, blue data). From **C2**, 500 µL was removed for ^{19}F NMR analysis (Figure S18B, green data). We also subjected independently synthesized Ni(II)($^{t\text{-Bu}}$bpy)(CF_3Ph)Cl and for ^{19}F NMR analysis (Figure S18D, black data).

From this analysis (Figure S18), we see formation of a ^{19}F NMR peak that corresponds to Ni(II)($^{t\text{-Bu}}$bpy)(CF_3Ph)Cl after both irradiation of the parent Ni(II) complex in the presence of the aryl chloride and after addition of to 2-*chloro*-α,α,α-trifluorotoluene directly to photogenerated **1-Cl**. Therefore, we conclude that oxidative addition of C(sp^2)–Cl bonds does occur in the presence of the photogenerated Ni(I) complexes as shown in main text Scheme 1.

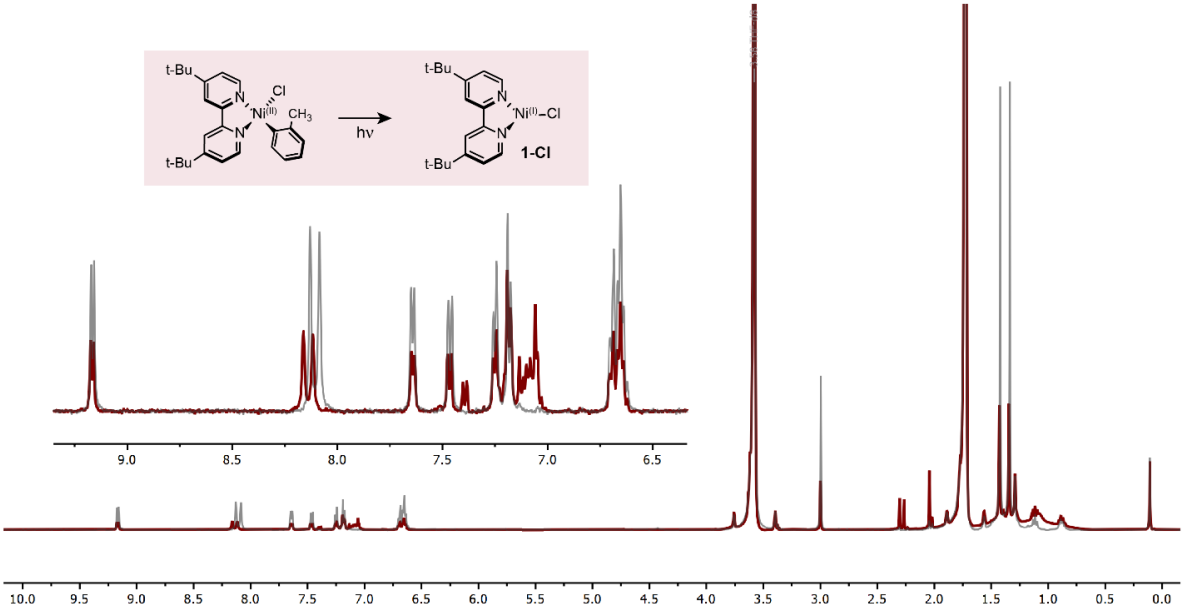

Figure S17. ^{1}H NMR spectra showing the decrease in the parent Ni(II) peaks upon irradiation of Ni($^{t\text{-Bu}}$bpy)(*o*-tolyl)Cl to form **1-Cl** for the oxidative addition study with 0.20 µL (~ 200 eq.) of 2-*chloro*-α,α,α-trifluorotoluene in d_8-THF (Figure S18).

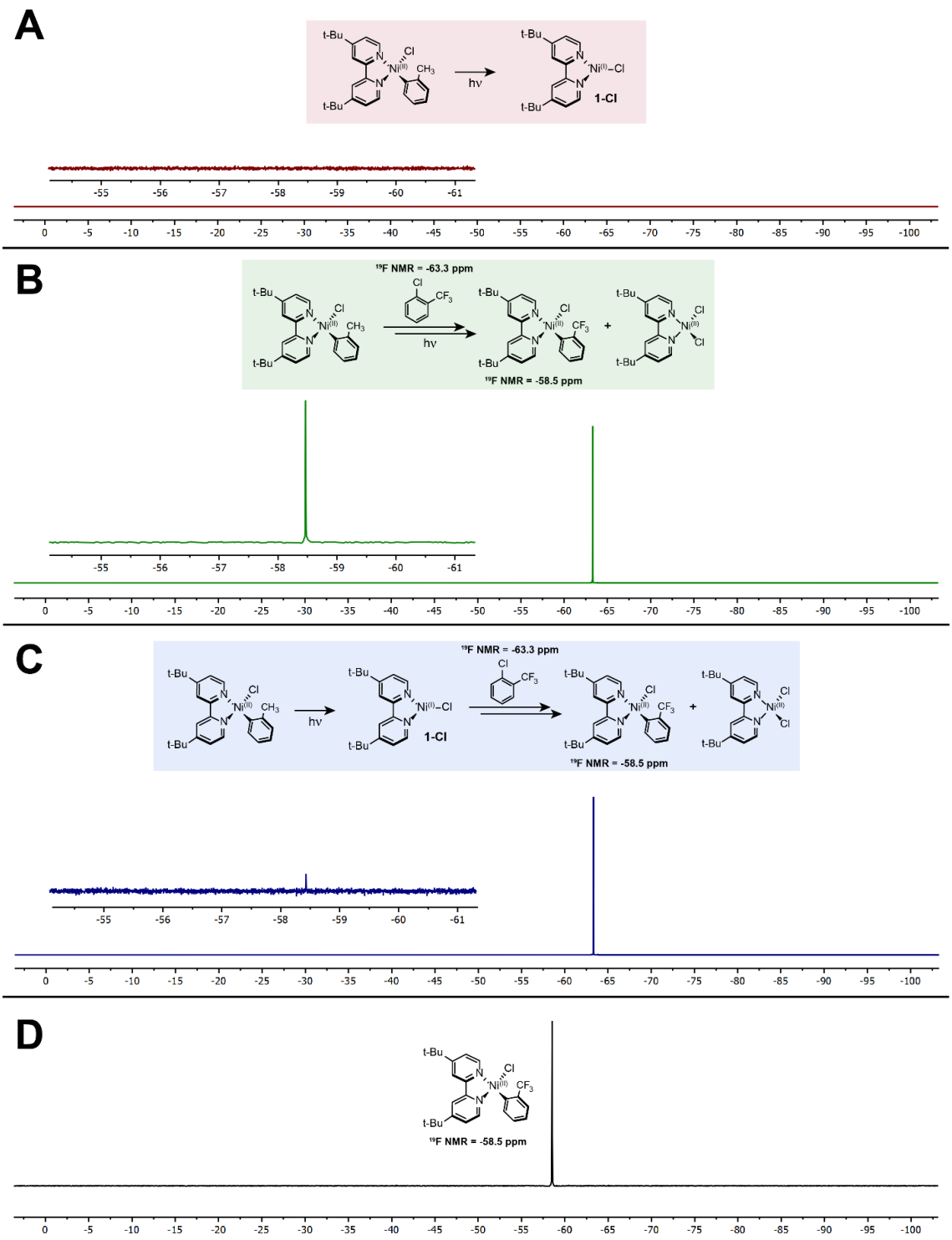

Figure S18. ^{19}F NMR spectra in d_8-THF showing (A) the absence of signals upon irradiation of Ni($^{t\text{-Bu}}$bpy)(*o*-tolyl)Cl to form **1-Cl** (^{1}H NMR spectra in Figure S17), (B) the formation of a new peak at –58.5 ppm when the parent Ni(II) complex is irradiated in the presence of 20 µL of 2-*chloro*-α,α,α-trifluorotoluene (peak at –63.3 ppm), (C) the formation of a new peak at –58.5 ppm when of 0.20 µL (~ 200 eq.) of 2-*chloro*-α,α,α-trifluorotoluene is added to pre-generated **1-Cl**, and (D) the presence of the peak at –58.5 ppm for independently generated Ni($^{t\text{-Bu}}$bpy)(CF_3Ph)Cl.

Time-resolved Ni(I)–bpy halide reactivity kinetics with 2-chloro-toluene by UV-vis.
Kinetic investigations were made by quantitative addition of excess 2-*chloro*-toluene to the photogenerated Ni(I) complexes such that the observed reaction followed *pseudo*-first order conditions. In a nitrogen-filled glove box, the parent Ni(II)(^{R}bpy)(*o*-tolyl)X, (R = *tert*-butyl, H, MeOOC; X = Cl, Br, I) were dissolved in THF, then transferred to air-free cuvettes charged with stir bars such that each cuvette held 3.000 mL of solution by microsyringe. Note that the solvent used must be strictly air, water, and impurity/stabilizer free, as the Ni(I) complexes demonstrate significant instability under non-ideal conditions. Ni(I)–bpy halide complexes were generated by irradiation of the parent Ni(II) complexes using Kessil PR160L 370 nm LEDs outside of the glove box. Therefore, the cuvettes used must also maintain strictly air- and water-free conditions. We found that Starna Cells 6-Q cuvettes fitted with a Kontes PTFE plug showed the greatest reproducibility.

After irradiation was completed, the cuvettes were reintroduced to the glove box. We used a StellarNet Inc. Black Comet UV-vis fitted with fiber optic cables and CUV 2 LensQ-Col holder to monitor the absorbance spectra of the complexes inside the glove box. This instrument was critical for the quantitative addition of the aryl halide, as we found that even using septa-based air-free techniques would provide inconsistent results due to trace air contamination. Once in the box, the cuvettes of Ni(I) solutions were uncapped, placed in the spectrometer holder, and stirred at 500 rpm. To each 3.000 mL cuvette, 0.150 mL of stock solutions of 2-*chloro*-toluene was added by microsyringe. Stock solutions were prepared as given in Table S4. Data were collected using Episodic Data Capture mode (10 ms integration time, 5 scans averaged). Reactions were run in triplicate. Oxidative addition kinetic data are only linear when plotting ln([**Ni(I)**]–[**Ni(I)**]$_0$) vs time, illustrative of the *pseudo* first-order nature of the reaction (Figures S19-S20).

Table S4. Specifications for the stock solutions prepared for quantitative addition of 2-*chloro*-toluene to the Ni(I)–bpy halide complexes.

Stock Sol'n	2-*Cl*-THF (mL)	THF (mL)	2-*Cl*-Tol:THF V:V	Stock [2-*Cl*-Tol] (M)	Stock Added (mL)	Final [2-*Cl*-Tol] (M)
1	0.500	1.000	1:2	2.852	0.150	0.136
2	1.000	1.000	1:1	4.277	0.150	0.204
3	1.000	0.500	2:1	5.703	0.150	0.272
4	1.500	0	N/A	8.555	0.150	0.407

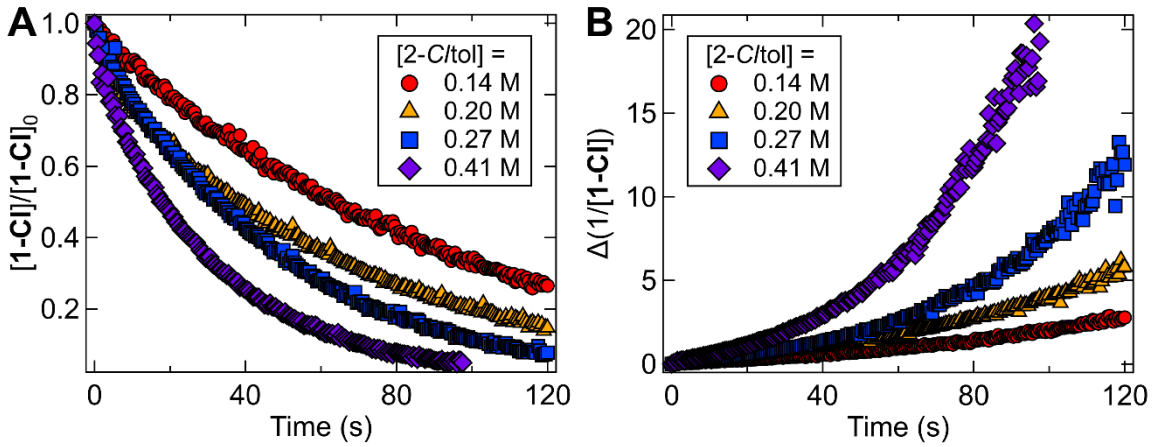

Figure S19. Evaluation of the order of the oxidative addition reaction, showing **1-Cl** with 2-*chloro*-toluene in THF at room temperature as a representative example. (A) Zero-order graph, showing the non-linearity when plotting Ni(I) concentration on the y-axis. (B) Second-order graph, showing the non-linearity when plotting the reciprocal of the Ni(I) concentration on the y-axis.

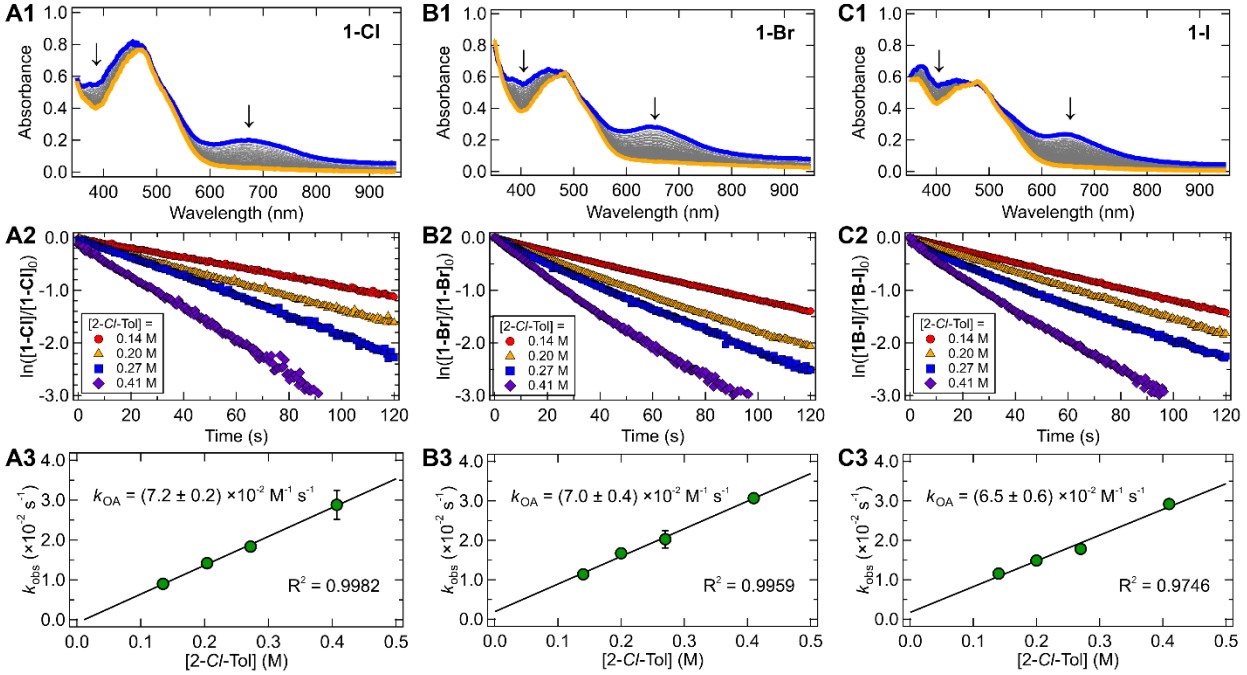

Figure S20. Experimental kinetic analysis of the oxidative addition reaction for **1-Cl**, **1-Br**, and **1-I**. (*A1, B1, C1*.) UV-vis absorption plots in THF showing the addition of 2-*chloro*-toluene to photochemically generated Ni(I)–bpy halides (initial spectrum of Ni(I)–bpy halide, blue line (~10^{-4} M); after 2-*chloro*-toluene addition, orange line). Note that the orange spectra depict unreacted and newly generated parent four-coordinate Ni(II)–bpy aryl halide. (*A2, B2, C2*.) Linear plots of ln([**Ni(I)**]/[**Ni(I)**]$_0$) versus time showing the pseudo-first order nature of the oxidative addition reaction over several half-lives; [2-*Cl*-Tol] = 0.14 M (red circles), 0.20 M (orange triangles), 0.27 M (blue squares), and 0.41 M (purple diamonds). (*A3, B3, C3*.) Plots of k_{obs} versus [2-*Cl*-Tol]. Error bars are one standard deviation of three trials. Slope of the fitted line gives second-order rate constants, k_{OA} (M^{-1} s^{-1}).

Time-resolved Ni(I)–bpy halide reactivity kinetics with 4-R-chlorobenzene by UV-vis and associated Hammett analysis.

In the same fashion as above, room temperature kinetic investigations were made into the aryl substituent dependence on the rate of oxidative addition of 4-R-chlorobenzene, where R = OCH_3, CH_3, H, $CONH_2$, and $COCH_3$. In the glove box, a ~0.2 mM solution of Ni(II)($^{t\text{-Bu}}$bpy)(*o*-tolyl)Cl was prepared in THF (absorbance ~1.0). The solution was transferred to an air-tight, quartz 40 mL scintillation vial which was further sealed with electrical tape prior to removal from the glove box. The sample was irradiated with Kessil PR160L 370 nm LEDs for 60 minutes forming ~0.1 mM **1-Cl**, reintroduced to the glove box, and split into 1 cm path length cuvettes (3.000 mL each by analytical syringe). To each 3.000 mL cuvette, 0.150 mL of stock solutions of 4-R-chlorobenzene was added by microsyringe. Concentrations were chosen such that the aryl chloride added was in a minimum of 10-fold excess. Data were collected using a StellarNet Inc. Black Comet UV-vis fitted with fiber optic cables and CUV 2 LensQ-Col holder in Episodic Data Capture mode (10 ms integration time, 5 scans averaged).

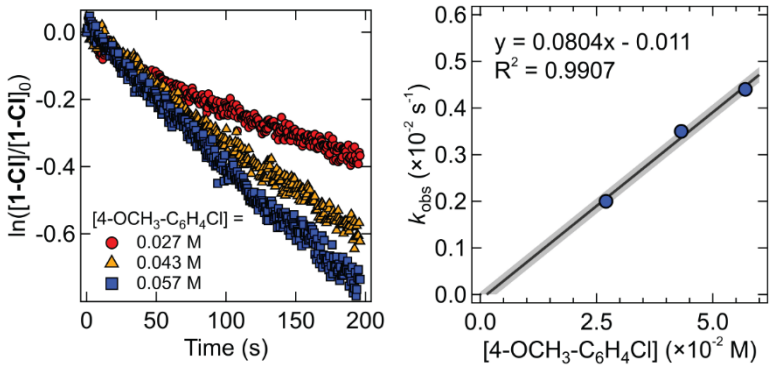

Figure S21. Kinetic data for the reaction of **1-Cl** with 4-OCH_3-C_6H_4Cl in THF. Linear plots of ln([**1-Cl**]/[**1-Cl)**]$_0$) versus time showing the pseudo-first order nature of the oxidative addition reaction over several half-lives. Final concentrations indicated in the legend. Error from the linear least-squares regression fit is given shaded in gray.

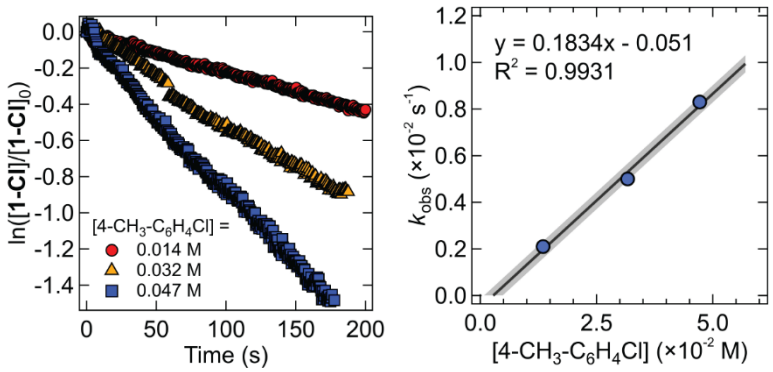

Figure S22. Kinetic data for the reaction of **1-Cl** with 4-CH_3-C_6H_4Cl in THF. Linear plots of ln([**1-Cl**]/[**1-Cl)**]$_0$) versus time showing the pseudo-first order nature of the oxidative addition reaction over several half-lives. Final concentrations indicated in the legend. Error from the linear least-squares regression fit is given shaded in gray.

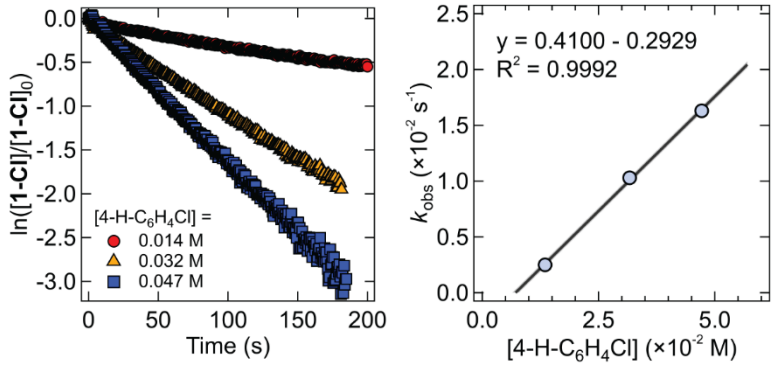

Figure S23. Kinetic data for the reaction of **1-Cl** with 4-H-C_6H_4Cl in THF. Linear plots of ln([**1-Cl**]/[**1-Cl)**]$_0$) versus time showing the pseudo-first order nature of the oxidative addition reaction over several half-lives. Final concentrations indicated in the legend. Error from the linear least-squares regression fit is given shaded in gray.

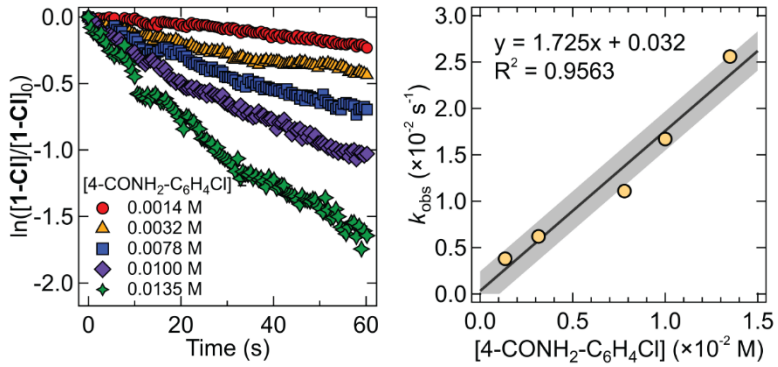

Figure S24. Kinetic data for the reaction of **1-Cl** with 4-$CONH_2$-C_6H_4Cl in THF. Linear plots of ln([**1-Cl**]/[**1-Cl)**]$_0$) versus time showing the pseudo-first order nature of the oxidative addition reaction over several half-lives. Final concentrations indicated in the legend. Error from the linear least-squares regression fit is given shaded in gray. Because of the speed of the reaction, two additional concentrations were tested.

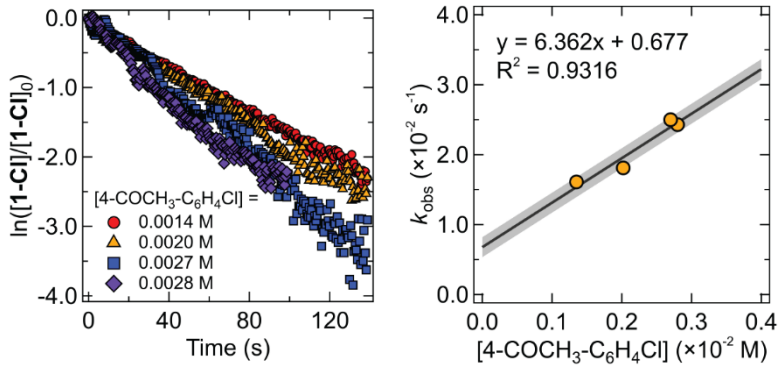

Figure S25. Kinetic data for the reaction of **1-Cl** with 4-$COCH_3$-C_6H_4Cl in THF. Linear plots of ln([**1-Cl**]/[**1-Cl)**]$_0$) versus time showing the pseudo-first order nature of the oxidative addition reaction over several half-lives. Final concentrations indicated in the legend. Error from the linear least-squares regression fit is given shaded in gray. Because of the speed of the reaction, an additional concentration was tested.

S1.8. Thermal Decomposition Experiments and Eyring Analysis.

Thermodynamics Experiments and Eyring Analysis.

When conducting the temperature dependent photolysis studies done previously, thermal dependence on the decomposition of the Ni(I) species was observed.[1] We were prompted to further investigate the solution-phase stability of the photogenerated Ni(I)–bpy halide species. To that end, we conducted variable temperature kinetic analysis.

In the glove box, we prepared solutions of the parent Ni(II)–bpy aryl halide complexes such that their primary MLCT absorption peak was ~1.0 absorbance (affording ~10^{-4} M solutions, V = 3.0 mL, solvent = THF). These stock solutions were transferred to air-free quartz cuvettes (10 mm), removed from the glove box one at a time, and irradiated using Kessil PR160L LEDs with incident light wavelength = 370 nm, forming the Ni(I)–bpy halide species. As in the oxidative addition studies, the cuvettes used must maintain strictly air- and water-free conditions (necessitating the use of Starna Cells 6-Q cuvettes fitted with a Kontes PTFE plug). Variable temperature decomposition kinetics were acquired on a UV-vis HP Agilent 8453 spectrophotometer coupled to an HP 89090A Peltier temperature controller with a cell holder. Samples were stirred during kinetic measurements; thermal decomposition analysis was done in the dark to avoid regeneration the Ni(I) by ambient light. Data points were acquired every 30 or 60 s, depending on the rate of dimerization. All measurements were baselined with THF at each temperature. Solutions for each temperature were prepared from a single parent Ni(II) stock and photolyzed with the same irradiation time to reproducibly form the Ni(I) complex for each series.

Decomposition data are only linear when plotting 1/([**Ni(I)**]–[**Ni(I)**]$_0$) vs time, illustrative of the second-order nature of the dimerization (Figures S26-S27). We note that for **2-Cl**, possible additional thermal decomposition pathways were seen at longer times, wherein the data became irregular. For **1-I**, large precipitation induced scattering necessitated the use of only early times for the analysis (i.e., before accumulation of the precipitate confounded the UV-vis data collection).

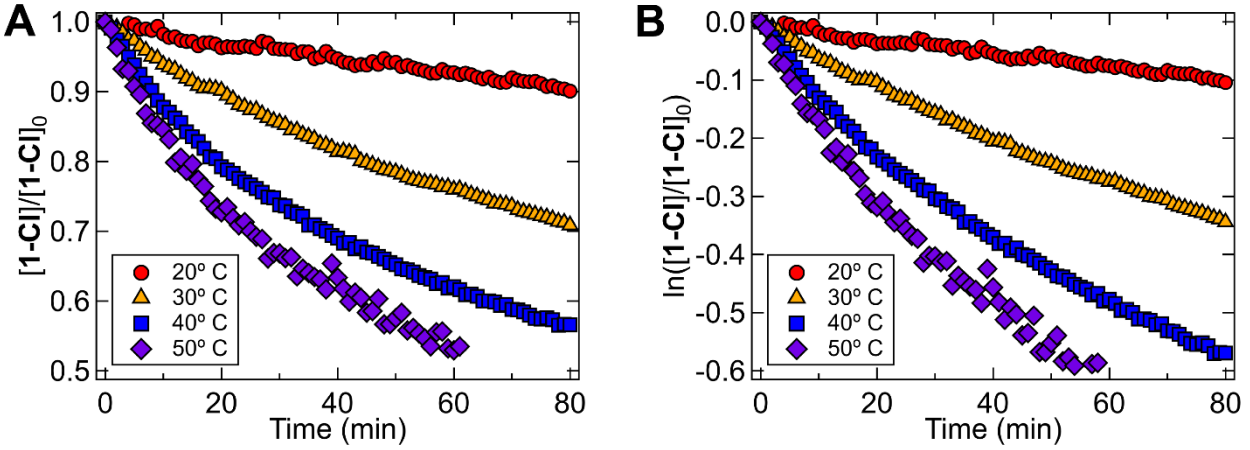

Figure S26. Evaluation of the order of the decomposition reaction, showing **1-Cl** in THF at temperatures 20 °C – 50 °C as a representative example. (A) Zero-order graph, showing the non-linearity when plotting Ni(I) concentration on the y-axis. (B) First-order graph, showing the non-linearity when plotting the natural log of the Ni(I) concentration on the y-axis.

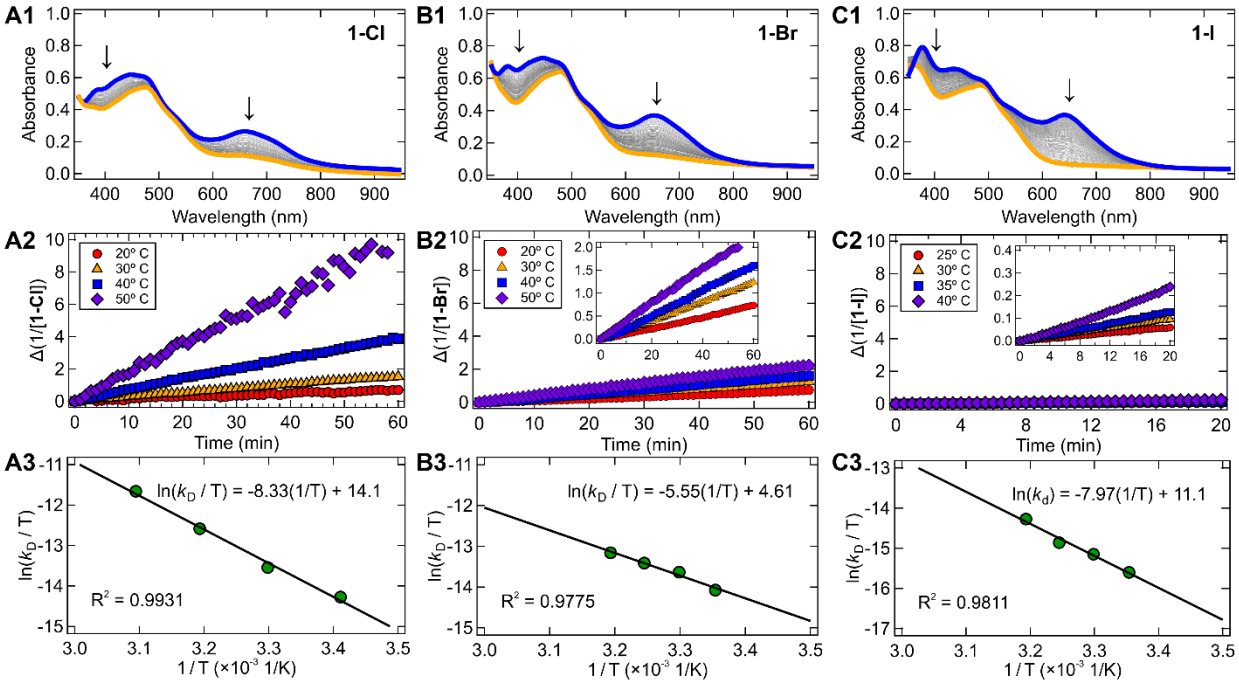

Figure S27. Experimental thermodynamic analysis of the dimerization reaction for **1-Cl**, **1-Br**, and **1-I**. (*A1, B1, C1*.) UV-vis-NIR absorption plots in THF showing the starting spectra of the Ni(I)–bpy halide generated by irradiation with 370 nm light (blue line) and the final spectra after thermally induced dimerization (orange line). Note that in the orange spectra some unreacted parent four-coordinate Ni(II)–bpy aryl halide remains. (*A2, B2, C2*.) Linear plots of 1/([**Ni(I)**]-[**Ni(I)**]$_0$) versus time showing the second-order nature of the dimerization; temperatures between 20 °C and 50 °C were chosen. (*A3, B3, C3*.) Eyring plots of ln(k_D/T) versus 1/T giving thermodynamics data. Large precipitation induced scattering required the use of early time points for **1-I**.

Identification of the Thermal Decomposition Product(s).

We sought to identify the precipitated product that originated from the second-order thermal decay of our Ni(I) species. To do this, in the glove box we prepared a 1 mM stock solution of Ni(II)($^{t\text{-Bu}}$bpy)(*o*-tolyl)Cl, the parent for **1-Cl** (16 mg in 30 mL). The solution was transferred to an air-tight, quartz 40 mL scintillation vial which was further sealed with electrical tape prior to removal from the glove box. The sample was irradiated with Kessil PR160L 370 nm LEDs overnight at 35 °C to convert all starting Ni(II). Precipitate was present the following day. The sample was brought into the glove box and left in the freezer to encourage additional precipitation (-35 °C for 72 hours). The precipitated solid was collected by pipette filtration and washed with cold toluene (3x3 mL) and hexanes (3x5 mL). The filtrate was brown and transparent; the collected solid was a brown-black color. A portion of this solid was redissolved in THF affording a brownish solution and its UV-vis spectrum recorded (Figure S28). Additionally, we collected the paramagnetic ^{1}H NMR of the sample in d_8-THF (Figure S29). ^{1}H NMR (400 MHz, d_8-THF): δ 134 (broad s, 1H), 57 (broad s, 3H), 38–41 (broad d, 3H), 1.3 (s, 36 H).

We found both spectra matched well with an independently synthesized [Ni(I)($^{t\text{-Bu}}$bpy)Cl]$_2$ dimer and with previous reports on the same complex.[2,3] As demonstrated previously, no EPR

signal was observed for the complex, even at cryogenic temperatures (Figure S30).[3] From these data, particularly the ^{1}H NMR, along with the second-order nature of the thermal decomposition reaction of **1-Cl**, we assign the primary decomposition product as a formal [Ni(I)($^{t\text{-Bu}}$bpy)Cl]$_2$ dimer.

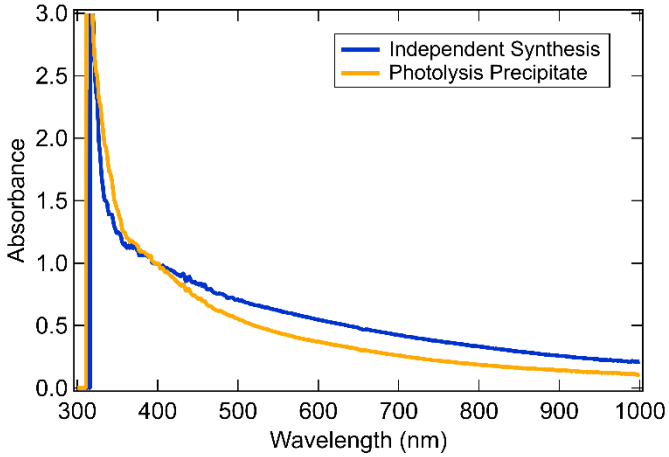

Figure S28. Comparison of the UV-vis-NIR absorbance spectra (THF) of the photolysis precipitate upon thermal decomposition of **1-Cl** to independently synthesized [Ni(I)($^{t\text{-Bu}}$bpy)Cl]$_2$ dimer. No clear absorption bands are resolved in either case in THF.

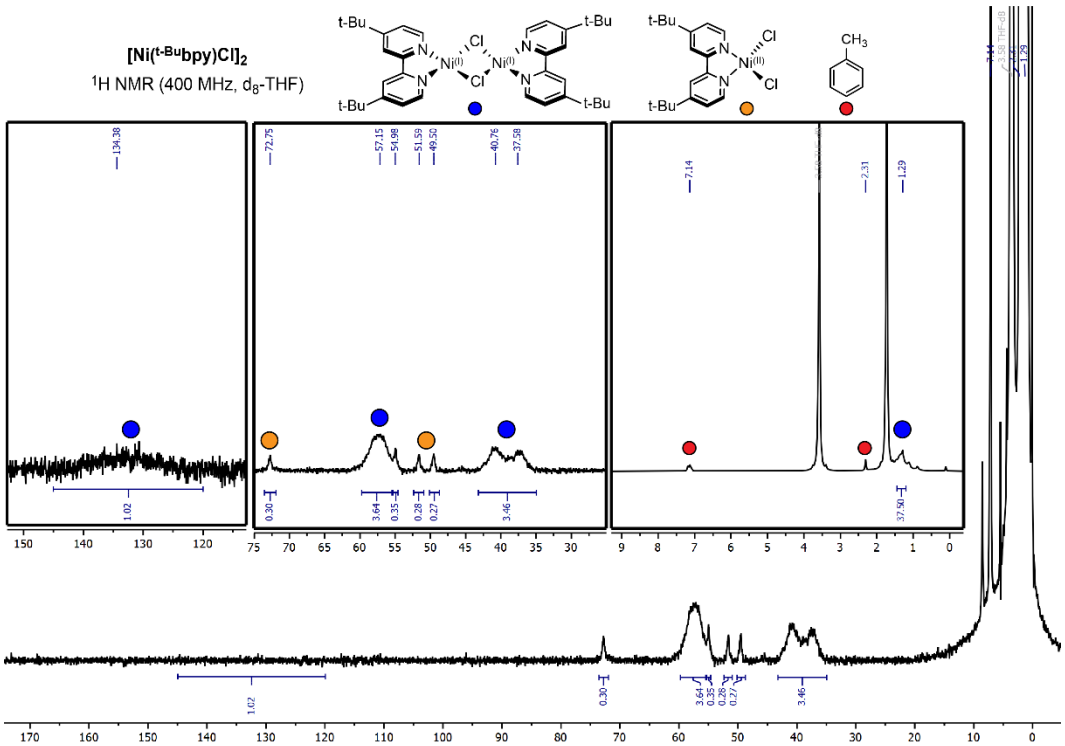

Figure S29. Paramagnetic ^{1}H NMR (400 MHz, d_8-THF) spectrum of the photolysis precipitate upon thermal decomposition of **1-Cl**. A small amount of Ni($^{t\text{-Bu}}$bpy)Cl$_2$ was also seen, likely the result of a secondary thermal decomposition of [Ni(I)($^{t\text{-Bu}}$bpy)Cl]$_2$ to Ni(II)($^{t\text{-Bu}}$bpy)Cl$_2$ and Ni(0)($^{t\text{-Bu}}$bpy).

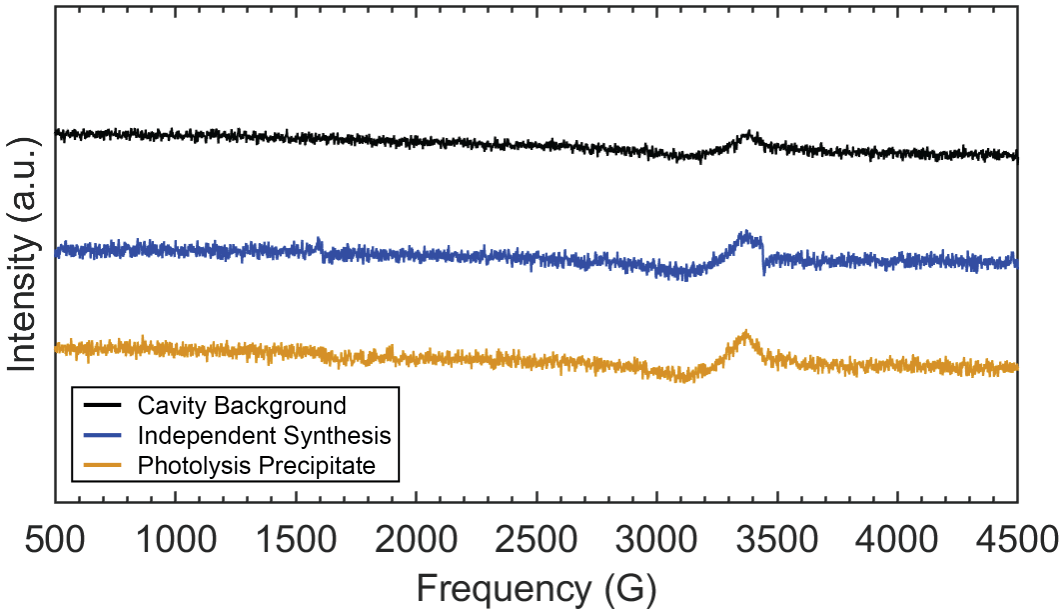

Figure S30. Comparison of the EPR spectra of the photolysis precipitate upon thermal decomposition of **1-Cl** to independently synthesized $[Ni(I)(^{t\text{-}Bu}bpy)Cl]_2$ dimer and the empty cavity background. As noted previously, the dimeric complex shows no resolvable EPR signal.[3] Data collected in 2-MeTHF and monitored by perpendicular mode EPR (5 K, 9.638 GHz, 8 G modulation amplitude, 2.184 mW power).

S1.9. Temperature and Concentration Dependent Speciation by EPR and UV-vis.

Compound **1-Cl** was subjected for the temperature- and concentration-dependent speciation analysis.

EPR samples were prepared in 4 mm medium wall, low pressure/vac Suprasil tubes, each fitted with a PTFE piston plug to ensure air- and moisture-free data collection. Samples were prepared in the glove box in 2-methyl tetrahydrofuran (2-MeTHF) as a glassing solvent analogue for THF. X-band CW-EPR spectra were acquired at the Caltech EPR facility on a Bruker EMX spectrometer. Cryogenic temperature control was achieved using liquid helium and an Oxford Instruments ESR-900 cryogen flow cryostat and an ITC-503 temperature controller. Spectra were simulated using EasySpin[4] (release 5.2.35) with Matlab R2020b.

Variable temperature UV-vis spectra were acquired using a Varian Cary 50 spectrophotometer equipped with a USP-203 series cryostat (UNISOKU Co.) and a liquid nitrogen dewar. Samples were equilibrated at each temperature for five minutes prior to acquisition. All spectra were baselined in THF at the appropriate temperature. The parent Ni(II) complex was irradiated at room temperature to afford **1-Cl**, then cooled to -90 ºC (183 K) where a UV-vis spectrum was recorded. Reversibility was ensured by warming the sample back to room temperature, re-collecting the room temperature UV-vis spectrum, the re-cooling the sample to 183 K and re-collecting the low-temperature spectrum. The spectra after the temperature cycling were identical to the ones collected prior.

Note: When referring to dilute solutions, the **1-Cl** sample was initially ~0.1-0.2 mM in THF by parent Ni(II) (as was typical for all other studies performed in this work); concentrated solutions are initially ~0.8-1 mM in THF by parent Ni(II). Dilute solutions were prepared in 1 cm cuvettes (Starna Cells 6-Q cuvettes fitted with a Kontes PTFE plug) and were irradiated using Kessil PR160L LEDs (370 nm incident light). Concentrated solutions were nearly opaque when in 1 cm cuvettes, so irradiation was performed in similar 2 mm air-tight cuvettes.

Variable Temperature and Concentration EPR Analysis.

Irradiation of a dilute solution of Ni(II)($^{t\text{-Bu}}$bpy)(*o*-tolyl)Cl with 370 nm light afforded **1-Cl** as before. However, when collecting EPR data on this same dilute sample, no EPR signal was resolvable at room temperature or at cryogenic temperature (blue and orange data in Figure S31). We turned to examining more concentrated samples in an attempt to sufficiently resolve the EPR signals.

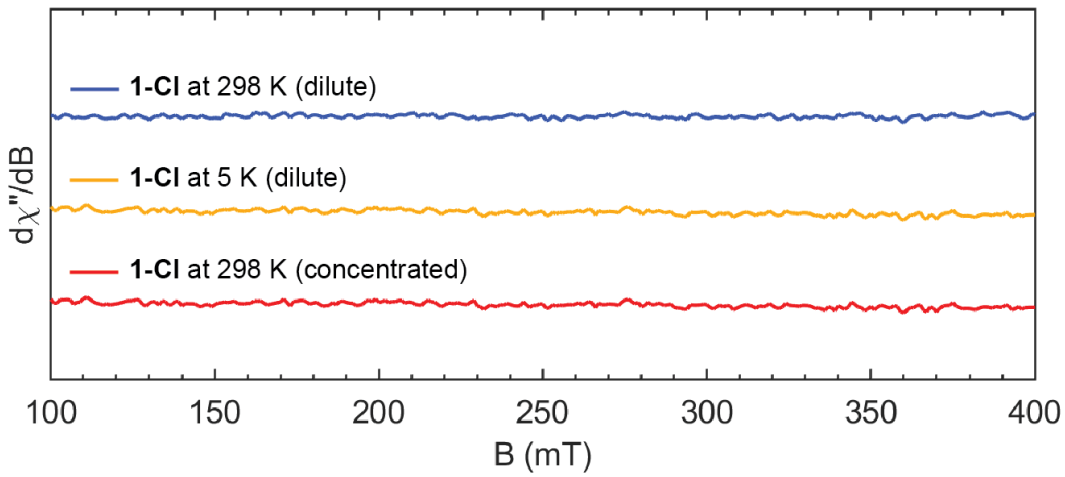

Figure S31. X-band EPR in perpendicular mode of dilute or concentrated samples of **1-Cl** formed by irradiation with 370 nm light of either 0.2 or 1 mM Ni(II)($^{t\text{-Bu}}$bpy)(*o*-tolyl)Cl in 2-MeTHF, respectively. Blue data, dilute: T = 298 K; solvent = 2-MeTHF; frequency = 9.852 GHz; power = 21.8 mW; modulation amplitude = 4 G. Orange data, dilute: frozen glass, T = 5 K; solvent = 2-MeTHF; frequency = 9.645 GHz; power = 2.2 mW; modulation amplitude = 8 G. Red data, concentrated: T = 298 K; solvent = 2-MeTHF; frequency = 9.854 GHz; power = 21.8 mW; modulation amplitude = 4 G. No EPR signals were resolvable at either temperature.

Interestingly, we noted that the room temperature UV-vis spectral profile of photogenerated **1-Cl** from a concentrated solution of parent Ni(II)($^{t\text{-Bu}}$bpy)(*o*-tolyl)Cl became mixed with another species that had overlapping absorbance at shorter wavelengths and a non-overlapping band at longer wavelengths (~850-900 nm) (Figure S32). Therefore, we find a concentration dependence on the speciation of the Ni species.

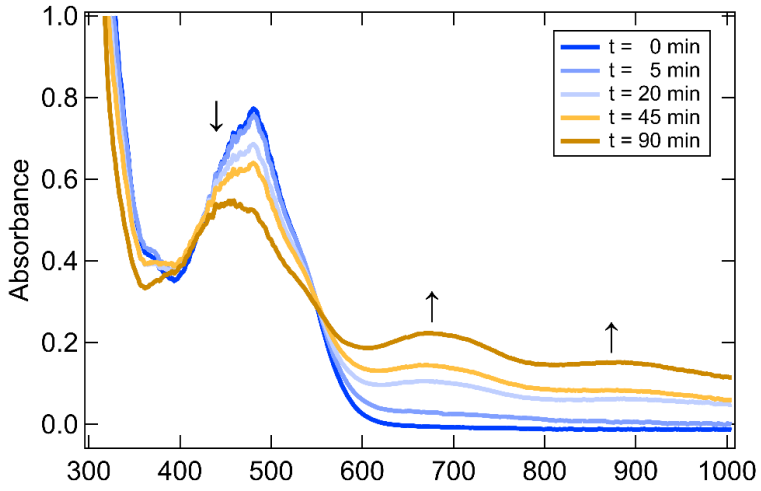

Figure S32. Irradiation of a concentrated sample of Ni(II)($^{t\text{-Bu}}$bpy)(*o*-tolyl)Cl with 370 nm light at room temperature in 2-MeTHF to form **1-Cl** and one or more additional species. DFT analysis is able to model this spectrum as a mixture of Ni(I) and a [Ni(I)/Ni(II)] binuclear species (Figure S63-S64).

While the EPR spectrum of this sample at 298 K afforded no resolvable signals (likely due to fast spin relaxation at warmer temperatures, see red data in Figure S31), spectra measured at

cryogenic temperatures (5 K) on this concentrated sample revealed a complex spectrum with additional spectral features (Figures S32-S35). We found that these could be assigned on the basis of simulations and comparisons to previous literature to two additional, distinct species. Simulations were performed on the 5 K data set to identify the complex speciation. We selected short (30 minute) and long (120 minute) irradiation times for comparison.

In the 5 K EPR data, we find an $S = 3/2$ species which features a perpendicular mode signal with effective g values of $g_1 = 3.64$, $g_2 = 4.76$, and $g_3 = 6.55$ (Figures S33-S35). A second species with $S = 2$ exhibits a parallel mode EPR signal with effective g values of $g_4 = 9.07$ and $g_5 = 13.49$ (Figures S33-S35). The relatively intense $g_5 = 13.49$ component also minimally presents itself in the perpendicular mode spectrum. The intensity of the $g_{eff} \approx 4$ signal of the $S = 3/2$ species is approximately doubled in the t = 120 min spectra over the t = 30 min spectra, while the intensity of the $S = 1/2$ signal does not change appreciably (Figures S33-S34) . In total, the complex EPR spectrum in Figure S35 can be simulated as a mixture of three species, with $S = 1/2$, $S = 3/2$, and $S = 2$ (red fit line in Figure S35) signals and a distribution ratio of ~1:16:3.

The $S = 3/2$ signal is similar to that reported by Nocera *et al.* for a mixed-valent Ni(I)/Ni(II) dimeric [Ni($^{t\text{-Bu}}$bpy)(quinuclidine)Cl]$_2$Cl complex.[5] The absence of parallel mode intensity for data reported herein indicates a half-integer spin complex, and two effective g values centered around g = 4 are generally characteristic of $S = 3/2$ systems with small zero field splitting rhombicity. No EPR signals were observed herein that could be attributed to the formal [Ni(I)($^{t\text{-Bu}}$bpy)Cl]$_2$ dimer, consistent with a previous report and our independent synthesis and analysis of this complex.[3] We also find that heating quenches the $S = 1/2$ signal and heating alone does not result in the formation of the $S = 3/2$ signal (Figure S36).

Finally, the parallel mode $S = 2$ signal is likely attributable to aggregation of dimeric [Ni(I)($^{t\text{-Bu}}$bpy)Cl]$_2$ to form the tetrameric [Ni(I)($^{t\text{-Bu}}$bpy)Cl]$_4$ species, similar to the [Ni(I)(^{EtOOC}bpy)Cl]$_2$ to [Ni(I)(^{EtOOC}bpy)Cl]$_4$ equilibrium observed by Doyle *et al.*, wherein the dimer of dimers has a combined spin of $S = 2$ by solid state magnetic moment measurements.[6]

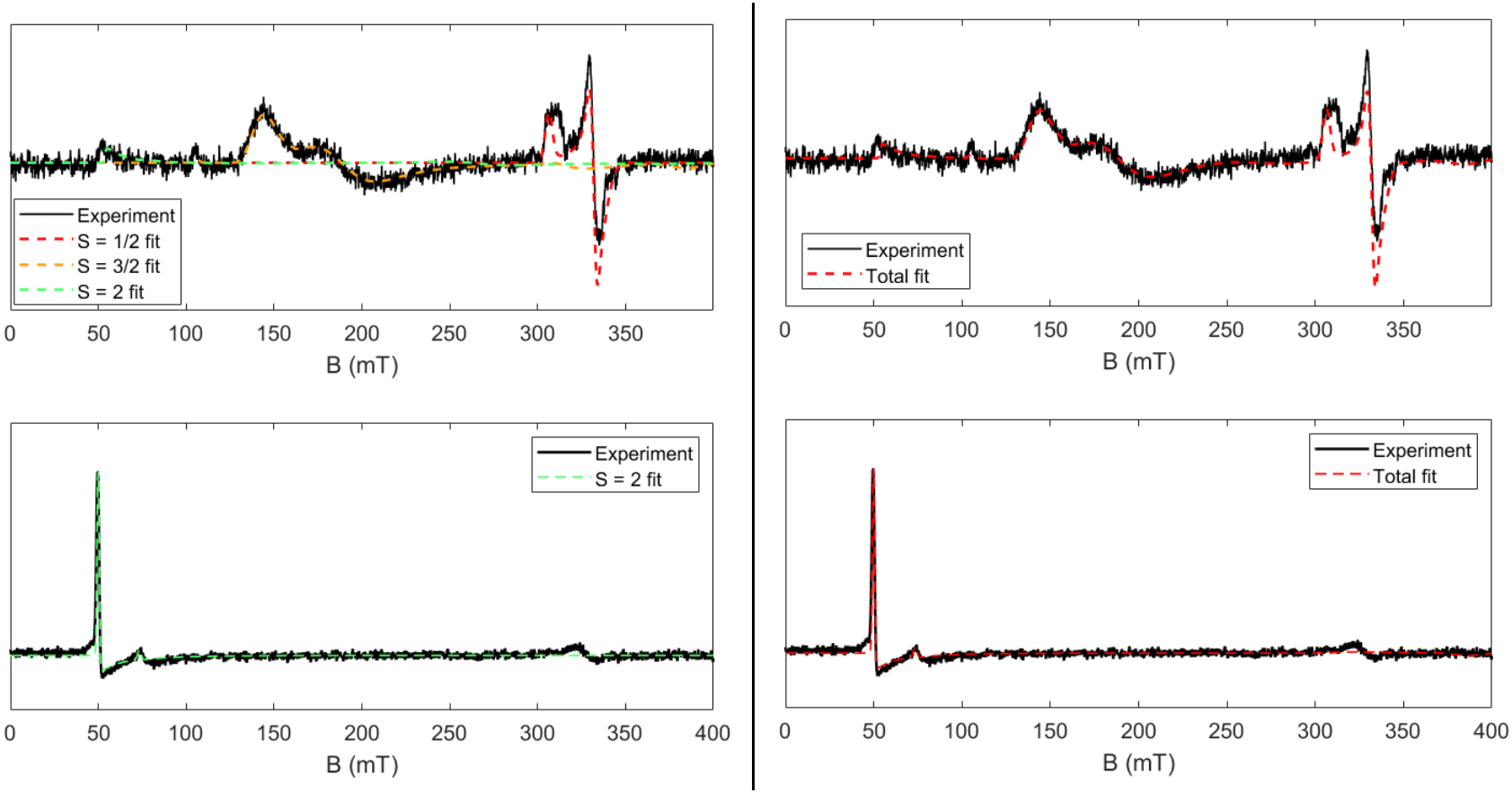

Figure S33. Frozen glass X-band EPR spectrum of photogenerated **1-Cl** from a concentrated sample of parent Ni(II)–bpy aryl halide. *Left:* Components of fit to 30-minute photolysis sample. *Right*: Total fit to 30 minutes photolysis sample. The half-field region is simulated $S = 3/2$ signal in perpendicular mode with effective g values of $g_1 = 3.64$, $g_2 = 4.76$, $g_3 = 6.55$ (T = 5 K; solvent = 2-MeTHF; frequency = 9.638 GHz; power = 2.2 mW; modulation amplitude = 8 G). The parallel mode spectrum is shown below, with $S = 2$ signal simulation ($g_4 = 9.07$ and $g_5 = 13.49$; T = 5 K; solvent = 2-MeTHF; frequency = 9.382 GHz; power = 8.8 mW; modulation amplitude = 8 G).

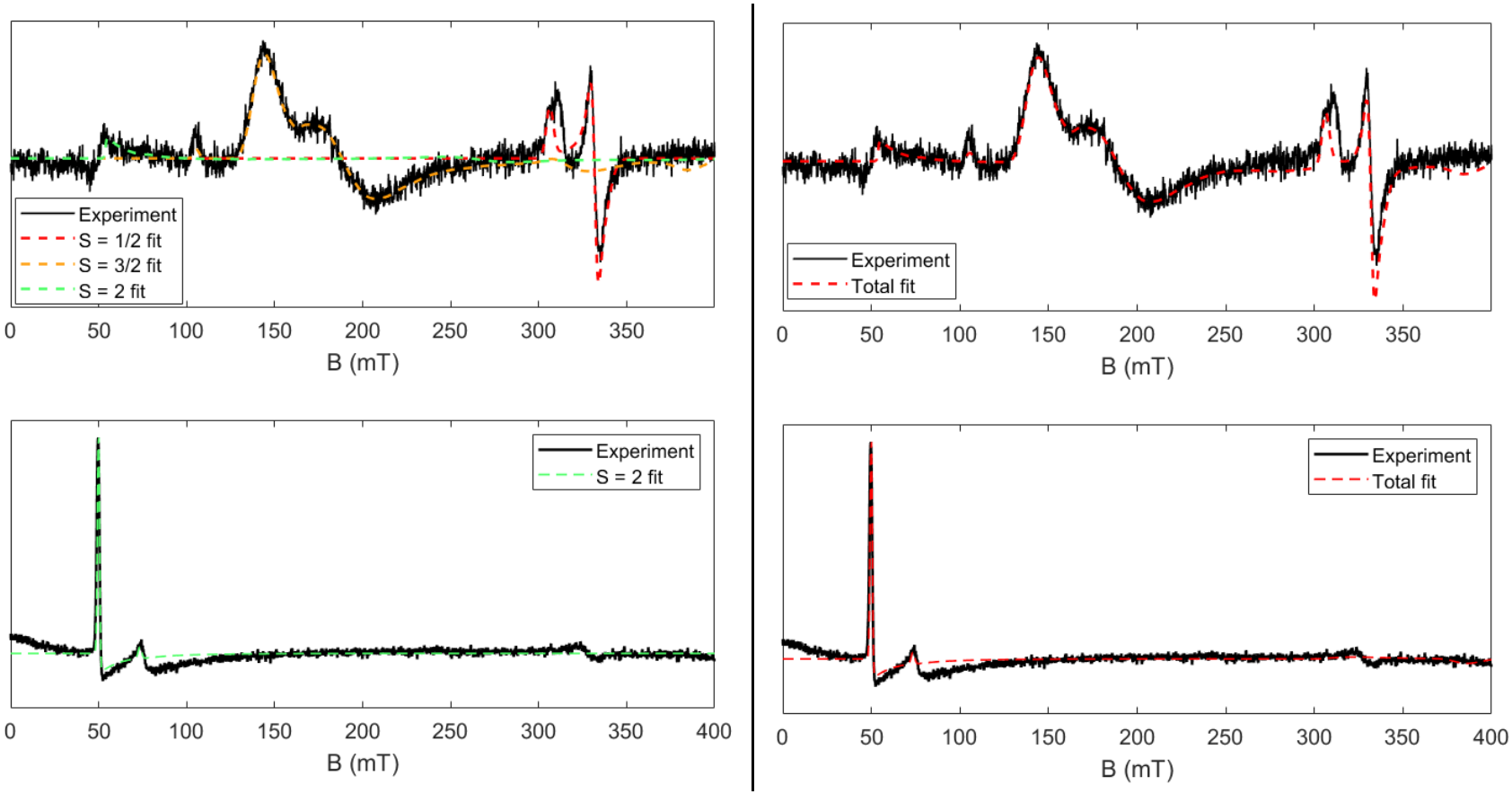

Figure S34. Frozen glass X-band EPR spectrum of photogenerated **1-Cl** from a concentrated sample of parent Ni(II)–bpy aryl halide. *Left:* Components of fit to 120-minute photolysis sample. *Right*: Total fit to 120-minutes photolysis sample. The half-field region is simulated $S = 3/2$ signal in perpendicular mode with effective g values of $g_1 = 3.64$, $g_2 = 4.76$, $g_3 = 6.55$ (T = 5 K; solvent = 2-MeTHF; frequency = 9.638 GHz; power = 2.2 mW; modulation amplitude = 8 G). The parallel mode spectrum is shown below, with $S = 2$ signal simulation ($g_4 = 9.07$ and $g_5 = 13.49$; T = 5 K; solvent = 2-MeTHF; frequency = 9.382 GHz; power = 8.8 mW; modulation amplitude = 8 G).

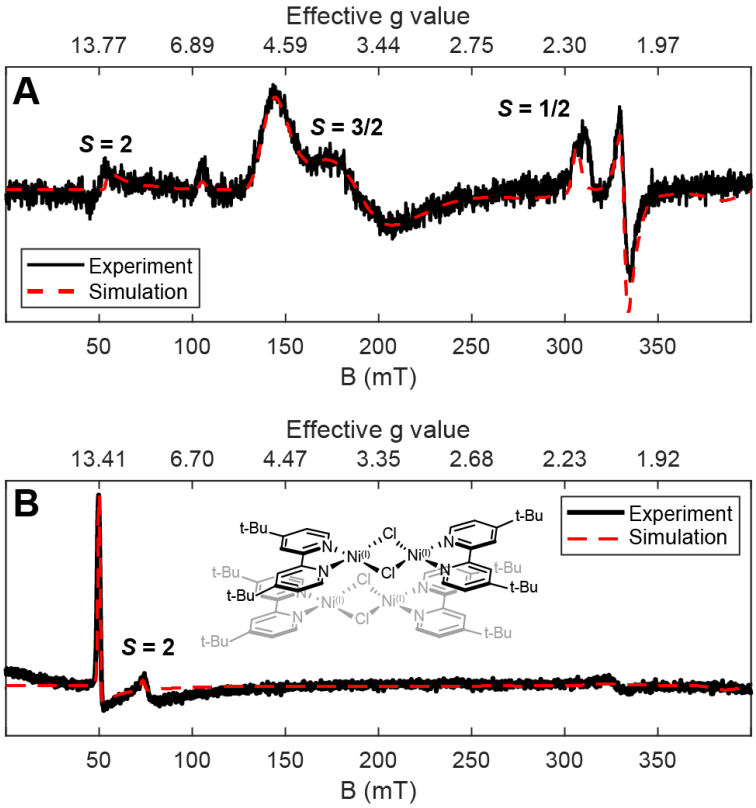

Figure S35. Frozen glass X-band EPR spectrum of photogenerated **1-Cl** from a concentrated sample of parent Ni(II)–bpy aryl halide after 120 minutes of irradiation with final fits and g values labelled. (A) The low field region is highlighted with a simulated $S = 3/2$ signal in perpendicular mode with effective g values of $g_1 = 3.64$, $g_2 = 4.76$, $g_3 = 6.55$ (T = 5 K; solvent = 2-MeTHF; frequency = 9.638 GHz; power = 2.2 mW; modulation amplitude = 8 G). (B) The parallel mode spectrum is shown, with $S = 2$ ($g_4 = 9.07$ and $g_5 = 13.49$) signal simulation and the structure of a plausible tetrameric [Ni(I)($^{t\text{-Bu}}$bpy)Cl]$_4$ species (T = 5 K; solvent = 2-MeTHF; frequency = 9.382 GHz; power = 8.8 mW; modulation amplitude = 8 G).

Table S5. Parameters for EPR fits.

	30-minute photolysis			**120-minute photolysis**		
	$S = 1/2$	$S = 3/2$	$S = 2$	$S = 1/2$	$S = 3/2$	$S = 2$
g(x)	2.045	2.161	2.0	2.045	2.161	2.0
g(y)	2.072	2.141	2.0	2.072	2.141	2.0
g(z)	2.248	2.210	2.0	2.248	2.210	2.0
D (cm^{-1})	N/A	0.467	0.694	N/A	0.467	0.694
E (cm^{-1})	N/A	0.0467	0.200	N/A	0.0467	0.200
E/D	N/A	0.10	0.29	N/A	0.10	0.29
E strain (cm^{-1})	N/A	0.037	0.0017	N/A	0.037	0.0017
HStrain(x) (MHz)	290	300	500	290	300	500
HStrain(y) (MHz)	101	300	50	101	300	50
HStrain(z) (MHz)	150	300	200	150	300	200
Weight	1	8.8	2.2	1	16	3
Species %	8.5	72.6	18.8	5.0	80.0	15.0

In Table S5, E strain values were simulated via explicit averaging over a Gaussian distribution of rhombic zero field splitting parameters, using 101 grid points. This approach is

necessary for large strains in the zero field splitting. The E strain values given specify the full-width-at-half-max of the Gaussian distribution. Note that the lineshapes of the $S = 2$ species could not be satisfactorily modeled using only D/E strain and isotropic line broadening, so anisotropic HStrain (unresolved hyperfine broadening) was employed. All simulations are conducted with a 50 knot grid. "Weight" refers to the total weighting of each component in the EasySpin simulation, which is converted to a percentage of each species in the "Species %" row. The results suggest that the concentration of the high spin species increases relative to the concentration of the $S = 1/2$ species as the photolysis time increases. Attempts to simulate the splitting of the $S = 1/2$ signal to account for potential solvent coordination through ^{1}H hyperfine coupling necessitated an unreasonably large coupling constant around 150 MHz; DFT predicts no ^{1}H couplings greater than 15 MHz (see Section S2.7. EPR hyperfine calculations). As such, the origin of this splitting is currently unclear.

Quenching experiments were conducted on samples prepared as follows. A concentrated solution of Ni(II)($^{t\text{-Bu}}$bpy)(*o*-tolyl)Cl, i.e., the parent complex for **1-Cl**, was prepared in 2-MeTHF and split into two 2 mm air-tight cuvettes. These were removed from the glove box and irradiated simultaneously (λ_{LED} = 370 nm) for 30 minutes. One cuvette was wrapped in aluminum foil to be covered from additional light and placed in a hot water bath for 90 minutes (T = 35 °C). The second cuvette was reintroduced to the glove box. An aliquot of this sample was transferred to an EPR tube for analysis. To the remaining sample, 0.2 mL of 2-*chloro*-toluene was added, resulting in a rapid color change. A portion of this sample was also transferred to an EPR tube for analysis.

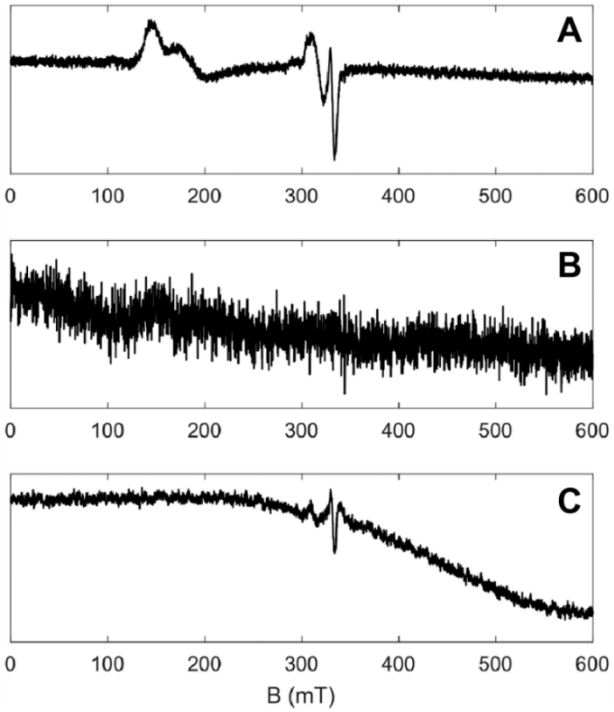

Figure S36. Quenching of a concentrated sample of **1-Cl** in 2-MeTHF monitored by perpendicular mode EPR (T = 5 K; solvent = 2-MeTHF; frequency = 9.637 GHz, power = 8.8 mW; modulation amplitude = 8 G). (A) **1-Cl** after 30 minutes of photolysis (λ_{LED} = 370 nm). (B) **1-Cl** after 30 minutes of photolysis and subsequent addition of 2-*chloro*-toluene. (C) **1-Cl** after 30 minutes of photolysis and subsequent heating (90 minutes at T = 35 °C).

The concentrated, irradiated sample shows strong S = 1/2 and S = 3/2 signals in perpendicular mode CW EPR (Figure S36A). Addition of 2-*chloro*-toluene (Figure S36B) completely quenches both the S = 1/2 and S = 3/2 signals, indicating that these signals correspond to reactivity. Additionally, both signals being quenched suggests a possible equilibrium between the two (more investigations into this notion given below). Prolonged heating (Figure S36C) significantly reduces the intensity of the S = 1/2 species but does not produce a S = 3/2 signal.

Variable Temperature UV-vis Analysis.

Because of the complex signals observed in the concentrated, low temperature EPR analysis, we sought to further decouple the concentration dependence from the temperature dependence of the samples. Therefore, we conducted detailed temperature dependence studies by variable temperature UV-vis (VT UV-vis) on a dilute sample of **1-Cl** to better understand the speciation of our system at low temperatures.

The VT UV-vis data indicate the formation of a new species at low temperature with absorption peaks at 440, 620 and 860 nm (Figure S37). These data share striking similarities to those seen in our concentrated photolysis solutions, and again, to the mixed-valent Ni(I)/Ni(II) [Ni($^{t\text{-Bu}}$bpy)(quinuclidine)Cl]$_2$Cl (S = 3/2) complex.[5] Additionally, TDDFT analysis is able to model the spectrum as a mixture of Ni(I) and the [Ni(I)/Ni(II)] binuclear species (Figure S63-S64). Thus, these data indicate that low temperature alone can drive the speciation changes seen in the cryogenic EPR.

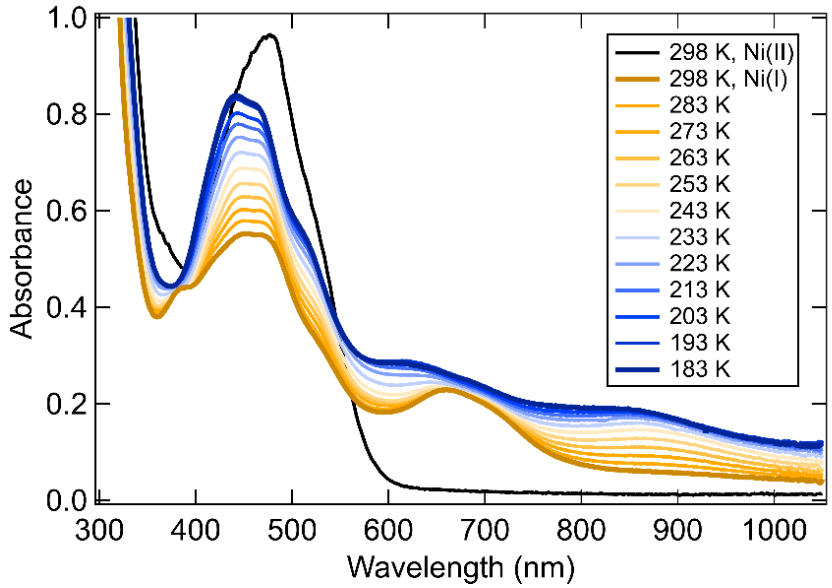

Figure S37. Variable temperature UV-vis data collected on a dilute solution of **1-Cl** in THF (mustard colored spectrum) generated by photolysis of the parent Ni(II) complex (spectrum before irradiation is given by the black line). The blue data represents low temperatures.

As we do not have quinuclidine in our system, we attempted to model the VT UV-vis data with an analogous aryl-based product, namely the mixed-valent S = 3/2 species [Ni(II)($^{t\text{-Bu}}$bpy)(*o*-tolyl)Cl/Ni(I)($^{t\text{-Bu}}$bpy)Cl], which represents the aggregation of the photogenerated Ni(I) complex, **1-Cl**, with its remaining, unreacted parent Ni(II) (Scheme S2). We

found the model to well deconvolute the low temperature data (Figure S38), with predicted thermodynamics values of $\Delta H = -7.7$ kcal mol^{-1}, $\Delta S = -13.1$ cal mol^{-1} K^{-1}, and $\Delta G(298K) = -3.8$ kcal mol^{-1}. Establishing an equilibrium constant expression for this aggregation gives equation S8, which, when using the predicted thermodynamics figures, we arrive at temperature dependent values for K_{eq} (equation S9).

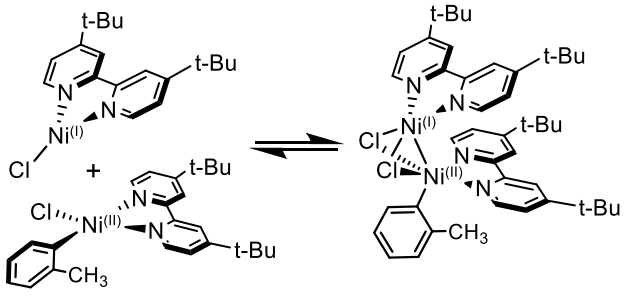

Scheme S2. Plausible equilibrium pathway for the aggregation of **1-Cl** with its unreacted parent Ni(II)–bpy aryl halide complex to form a binuclear [Ni(II)($^{t\text{-Bu}}$bpy)(*o*-tolyl)Cl/Ni(I)($^{t\text{-Bu}}$bpy)Cl] species.

$$K_{eq} = \frac{[\text{Ni(I)/Ni(II)}]}{[\text{Ni(I)}][\text{Ni(II)}]} \qquad \textbf{(eq. S8)}$$

$$K_{eq}(298K) = 6.6 \times 10^2; K_{eq}(165K) = 2.5 \times 10^7 \qquad \textbf{(eq. S9)}$$

By this model, a photogenerated, dilute sample of **1-Cl** (starting parent [Ni(II)] = 0.2 mM and assuming 50% conversion, [Ni(II)] = [Ni(I)] = 0.1 mM) will see negligible amounts of the binuclear Ni(I)/Ni(II) species present at room temperature ([Ni(I)/Ni(II)] = 6 μM). But, under concentrated conditions ([Ni(II)] = 0.5 mM = [Ni(I)] = 0.5 mM), the predicted concentration of the aggregate species is 20-fold larger, with [Ni(I)/Ni(II)] = 125 μM, and should be visible in room temperature UV-vis data (estimating $\varepsilon = 2500$ M^{-1} cm^{-1} gives an absorbance of ~0.3).

However, at T ≤165 K (the freezing point of THF) both dilute and concentrated samples of photogenerated **1-Cl** will have undergone stoichiometrically complete aggregation to the [Ni(I)/Ni(II)] binuclear complex. Therefore, the amount of remaining monomeric Ni(I) in solution is highly concentration- and temperature- dependent, determined by both the amount of Ni(I) photogenerated from the parent Ni(II), the exact ratio of Ni(I) to Ni(II) present at the end of irradiation, and the temperature at which the experiment is conducted (Table S6).

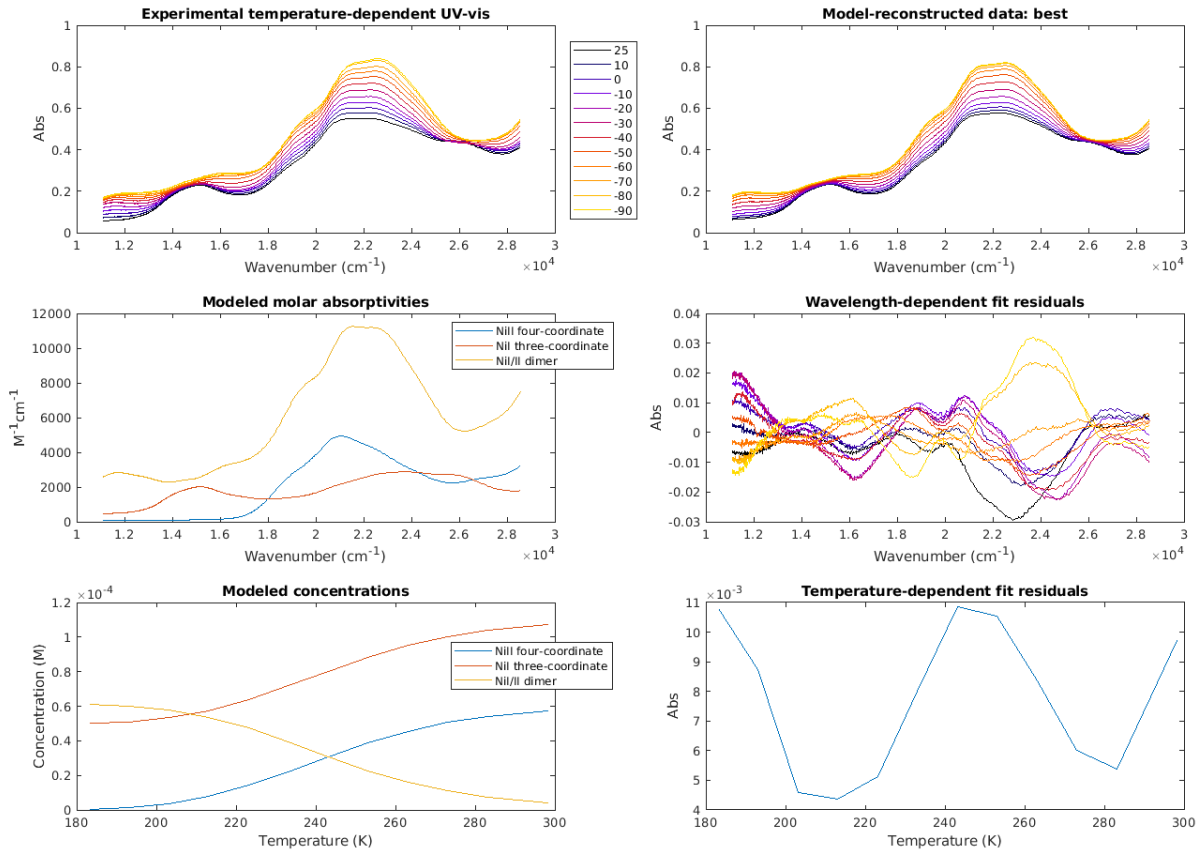

Figure S38. Global analysis modelling on the temperature dependent speciation observed in the VT UV-vis experiment on **1-Cl** in THF (Figure S37). *Top left:* Experimental temperature dependent UV-vis data. *Top right:* Reconstructed VT UV-vis dataset using the [Ni(I)] + [Ni(II)] → [Ni(I)/Ni(II)] model shown in Scheme S2. *Center left*: Deconvoluted absorption spectra given by the model for the three species in question, illustrating the new bands formed by the binuclear complex. *Center right*: Residuals after the absorbance modeling was completed. *Bottom left:* Plot of the concentrations as a function of temperature. Room temperature seems negligible binuclear complex. *Bottom right*: Residuals after the temperature dependence modeling was completed; note the small y-axis scale.

Table S6. Concentrations of various Ni species in solution as calculated from the thermodynamic values obtained from the fit to the VT UV-vis data and equations S8-9. Yellow and blue shaded data are dilute or concentrated conditions, respectively. Estimates are given for 50%, 75%, and 95% complete photolysis.

	Pre-photolysis			**Post-photolysis, Pre-equilibrium**			**Post-photolysis, Post-equilibrium**		
T (K)	**[Ni(II)] (mM)**	**[Ni(I)] (mM)**	**[Ni(I)/Ni(II)] (mM)**	**[Ni(II)] (mM)**	**[Ni(I)] (mM)**	**[Ni(I)/Ni(II)] (mM)**	**[Ni(II)] (mM)**	**[Ni(I)] (mM)**	**[Ni(I)/Ni(II)] (mM)**
298	0.200	0.000	0.000	0.100	0.100	0.000	0.097	0.097	0.006
	0.200	0.000	0.000	0.050	0.150	0.000	0.048	0.148	0.005
	0.200	0.000	0.000	0.010	0.190	0.000	0.009	0.189	0.001
	1.000	0.000	0.000	0.500	0.500	0.000	0.438	0.438	0.125
	1.000	0.000	0.000	0.250	0.750	0.000	0.203	0.703	0.093
	1.000	0.000	0.000	0.050	0.950	0.000	0.038	0.938	0.023
	Pre-photolysis			**Post-photolysis, Pre-equilibrium**			**Post-photolysis, Post-equilibrium**		
T (K)	**[Ni(II)] (mM)**	**[Ni(I)] (mM)**	**[Ni(I)/Ni(II)] (mM)**	**[Ni(II)] (mM)**	**[Ni(I)] (mM)**	**[Ni(I)/Ni(II)] (mM)**	**[Ni(II)] (mM)**	**[Ni(I)] (mM)**	**[Ni(I)/Ni(II)] (mM)**
165	0.200	0.000	0.000	0.100	0.100	0.000	0.003	0.003	0.194
	0.200	0.000	0.000	0.050	0.150	0.000	0.000	0.100	0.100
	0.200	0.000	0.000	0.010	0.190	0.000	0.000	0.180	0.020
	1.000	0.000	0.000	0.500	0.500	0.000	0.006	0.006	0.987
	1.000	0.000	0.000	0.250	0.750	0.000	0.000	0.500	0.500
	1.000	0.000	0.000	0.050	0.950	0.000	0.000	0.900	0.100

Summary of Speciation Experiments.

Altogether, we propose that the photolysis of Ni(II)–bpy aryl halides gives dominantly a single species at room temperature – namely, a three-coordinate Ni(I)–bpy halide. However, this Ni(I) complex can undergo reversible aggregation with its unreacted parent Ni(II) when either under concentrated conditions or at low temperatures, forming a mixed-valent [Ni(II)($^{t\text{-Bu}}$bpy)(*o*-tolyl)Cl/Ni(I)($^{t\text{-Bu}}$bpy)Cl] species.

Alternatively at elevated temperatures, the irreversible thermal decomposition product of the Ni(I) is a formal [Ni(I)($^{t\text{-Bu}}$bpy)X]$_2$ dimer (X = Cl, Br, I) as described in Section S1.8. These can precipitate from solution and/or can oligomerize to a tetrameric [Ni(I)($^{t\text{-Bu}}$bpy)X]$_4$ species seen in the parallel mode, low temperature EPR. Combined variable temperature UV-vis and parallel/perpendicular mode EPR thus provides a semi-quantitative handle on several catalytically relevant species and their interconversions with variations in time and reaction conditions.

S2. Computational Section.

S2.1. General Computational Details.

All the computations were performed using ORCA 5.0.3 software.[7,8] Analysis of the intrinsic bond orbitals was performed in IboView v20211019-RevA.[9,10]

The spin states considered in our computational analysis were taken following experimental data. That is, Ni(II)(^{R}bpy)ArX is a square-planar (S = 0) complex, Ni(II)(^{R}bpy)X_2 is a *pseudo*-tetrahedral (S = 1) complex, and monomeric Ni(I)(^{R}bpy)X is a $3d^9$ (S = 1/2) complex. Along the oxidative addition reaction coordinate, a doublet spin state is maintained (see Ni Löwdin population in main text Figure 5C) wherein the three-coordinate Ni(I) complex is oxidized to a five-coordinate Ni(III) complex. Rapid comproportionation of $3d^9$ (S = 1/2) Ni(I) and $3d^7$ (S = 1/2) Ni(III) return the $3d^8$ (S = 0) Ni(II) and $3d^8$ (S = 1) Ni(II) complexes mentioned above.

For the [Ni(I)/Ni(II)] binuclear complexes, an S = 3/2 spin state was considered to maintain agreement with the EPR measurements shown above in Supporting Information Section S1.9. For the [Ni(I)/Ni(I)] dimeric complexes, the high spin (S = 1) state was found in computations to be lower in energy than low spin state (S = 0). This energetic ordering is consistent with the experimental data provided by Hazari et al. on their [Ni(I)/Ni(I)] dimer[3] and with our paramagnetic ^{1}H NMR (Figures S29 and S73).

Density Functional Theory Calculations.
The molecular structures were optimized with DFT using the BP86 functional[11,12] with def2-TZVPP(Ni)+def2-TZVP basis set[13], D3BJ dispersion correction[14,15], and the CPCM solvation model (THF).[16,17] The calculations were expedited by expanding the Coulomb integrals in an auxiliary basis set, the resolution-of-identity (RI-J) approximation.[18] On top of the optimized geometries, the electronic energy terms and molecular properties were evaluated using the hybrid B3LYP functional[19,20] with the same def2-TZVPP(Ni)+def2-TZVP basis set, D3BJ dispersion correction, CPCM solvation model, and RIJCOSX approximation.[21] The transition states for Ni(I) reactivity toward oxidative addition with 2-*chloro*-toluene and toward dimerization were found by performing relaxed 1D or 2D scans on the potential energy surface and optimizing the appropriate geometry to a saddle point using OptTS keyword in ORCA. The character of the transition state was confirmed by calculating the intrinsic reaction coordinate (IRC) connecting correct reactants and products.

For the equilibrium geometries, the terms contributing to Gibbs free energy were calculated as follows:

$$G = E_{el} + G_{solv} + [E_{ZPVE} + RT - RTlnQ] \quad \textbf{(eq. S10)}$$

where, *i*) E_{el} is the *in vacuo* electronic energy; calculated using RI-B3LYP-D3 method as above, *ii*) G_{solv} is the free energy of solvation; calculated using CPCM, *iii*) [E_{ZPVE} + RT – RT ln Q] corresponds to the thermal enthalpic and entropic contributions to the solute energy with E_{ZPVE} and Q being the zero-point vibrational energy and the molecular partition function, respectively; obtained from frequency calculations with the rigid rotor/harmonic oscillator approximation (for p = 1 bar, T = 298 K).

Time-Dependent Density Functional Theory
To inspect the excited states and compare computations with the experimental UV-vis spectra, we have performed TDDFT calculations (total of 150 roots) on top of the DFT-optimized ground-state geometries.

Electron Paramagnetic Resonance Calculations
The EPR properties were predicted on top of the DFT-optimized ground-state geometries using ORCA program with the zero-order regular approximation (ZORA)[22] to account for the scalar relativistic effects along with the recontracted Ahlrichs's def2 basis set[23] analogous to above.

Intrinsic Bond Orbital Analysis (IBO)
A trajectory of the oxidative addition of 2-*chloro*-toluene near the transition state, connecting Ni(I) + 2-*chloro*-toluene reactant complex with the pentacoordinate Ni(III), was investigated in terms of intrinsic atomic orbitals (IAOs)[9], generated with IboView program. The IAOs of the occupied and valence virtual space were generated from the UKS wavefunctions along the IRC obtained from DFT calculations as described above.

Optimized structures of all the studied Ni complexes and their reactivity are attached as the XYZ coordinates in a separate zip archive.

The XYZ coordinate system used for labeling orbitals throughout the manuscript was selected according to the parent Ni(II) complexes to maintain consistency with the previous studies, i.e., the x and y axes are oriented along the Ni–N(bpy) axes, making the singly occupied orbital to be the $3d(x^2\text{-}y^2)$ (*cf.* Figures S40-S44). By this, the orbitals parallel and perpendicular to the Ni–halide axis are the mixtures of d(xz) and d(yz) orbitals. To distinguish them, we thus label the orbitals as d(xz/yz,∥) and d(xz/yz,⊥) according to their parallel and perpendicular orientation to the Ni–halide axis.

S2.2. Sample ORCA inputs

Example DFT Geometry Optimization
```
! UKS BP86 def2-TZVP def2/J RI D3BJ
! Opt Freq CPCM(THF) SlowConv
%basis
newgto Ni "def2-TZVPP" end
end
*xyzfile 0 2 orca.xyz
```

Example TD-DFT Calculation
```
! UKS B3LYP def2-TZVP def2/J RIJCOSX
! D3BJ SP CPCM(THF) SlowConv
%basis
newgto Ni "def2-TZVPP" end
end
%tddft
  maxdim 5
  nroots 150
  end
*xyzfile 0 2 orca.xyz
```

Example DFT Single-Point Calculation
```
! UKS B3LYP def2-TZVP def2/J RIJCOSX
! D3BJ SP CPCM(THF) SlowConv
%basis
newgto Ni "def2-TZVPP" end
```

Example EPR g-value Calculation
```
! UKS B3LYP RIJCOSX ZORA
! ZORA-def2-TZVP SARC/J TIGHTSCF
! SlowConv PrintBasis KeepDens Normalprint
%basis
```

```
end
*xyzfile 0 2 orca.xyz
```

```
newgto Ni "ZORA-def2-TZVPP" end
end
%method
Z_solver DIIS
Z_MaxIter 200
Z_shift 0.3
end
%eprnmr
  gtensor 1
  ori CenterOfElCharge
  printlevel 3
end
*xyzfile 0 2 orca.xyz
```

Example DFT Hyperfine Calculation:

```
! UKS B3LYP RIJCOSX EPR-II TIGHTSCF defgrid3 LargePrint

%pal nprocs 16
end
%maxcore 10000

%coords
  CTyp xyz
  Charge 0
  Mult 2
  Units Angs
  Cord's
    #partial coordinates shown for 1-Cl with equatorially bound THF
 H   0.91140189256141    -2.75340569830985     2.26706163504301  #THF 1
 H   1.38500502228926    -1.01827334418779     2.31640763935316  #THF 2
 H   -2.53521442619047    -1.66999666911873     1.54553955144057 #THF 3
 H   -1.92710462521832    -0.14712822615522     2.28463929137903 #THF 4
 H   0.06585266218129    -3.00824124719865    -0.18728883176952  #bpy 1
 H   -0.34759843194471     3.03663782528236    -0.58015902906400 #bpy 2
 H   0.05875238553313     3.31984436095385    -7.41050856790225  #t-Bu control
    #...etc...
 Ni  -0.05672247554837     0.04505035145523    -0.01438171920704
     newgto "CP(PPP)" end
 Cl  0.38801515211621     1.58197372153268     1.59887317363223
     newgto "IGLO-II" end
    # ...remaining atoms
end
end

%eprnmr
  Nuclei = 1 { aiso, adip }
  Nuclei = 2 { aiso, adip }
  Nuclei = 3 { aiso, adip }
```

```
  Nuclei = 4 { aiso, adip }
  Nuclei = 5 { aiso, adip }
  Nuclei = 6 { aiso, adip }
  Nuclei = 7 { aiso, adip }
  Nuclei = all N { aiso, adip, fgrad }
  gtensor 1
  ori CenterOfElCharge
  printlevel 3
end
```

S2.3. Intrinsic bond orbital analysis.

To interpret the molecular electronic structure of Ni(I) complexes, we analyze the SCF wavefunctions by localizing the molecular orbitals by using the intrinsic atomic orbitals (IAOs). This technique was previously reported as valuable for understanding chemical structure and reaction mechanisms generally consistent with chemical intuition.[10] We have started from the intrinsic reaction coordinate (IRC) computed for **1-Cl** oxidative addition of 2-*chloro*-toluene. For each point of the IRC, we have computed the electronic energy at the unrestricted B3LYP level and analyzed the corresponding wavefunctions. These were used to generate IAOs and the corresponding intrinsic bond orbitals (IBOs) to obtain a clearer understanding of chemical bonding and its progression along the reaction coordinate, as a measure of the change in the bond orbitals.

In our case, the IBOs transform continuously from the electronic structure of reactants to electronic structure of products; the largest change is observed in the Ni 3d(z^2) orbital, which is transformed into a new Ni–C_{aryl} σ bond and C_{aryl}–Cl σ bond that is transformed into a new Ni–Cl σ bond. This is indicative of a two-electron transfer in the S_N2-like reactivity. All other IBOs represent nonreactive orbitals, with the exception of aryl π orbitals that are shifted along the aryl plane to accommodate new bonding pattern.

As discussed in the main text, this picture corresponds to the classical S_N2-like reactivity with two electrons being transferred from the Ni 3d(z^2) orbital into the C_{aryl}–Cl σ* orbital, leading to the breaking of C_{aryl}–Cl and the formation of two new sigma bonds. However, we note that a transfer of the two electrons from Ni 3d(z^2) orbitals is not fully concerted. The β electron is transferred earlier than α, which is consistent with the higher β-3d(z^2) energy; therefore, the TS is more involved considering the β density.

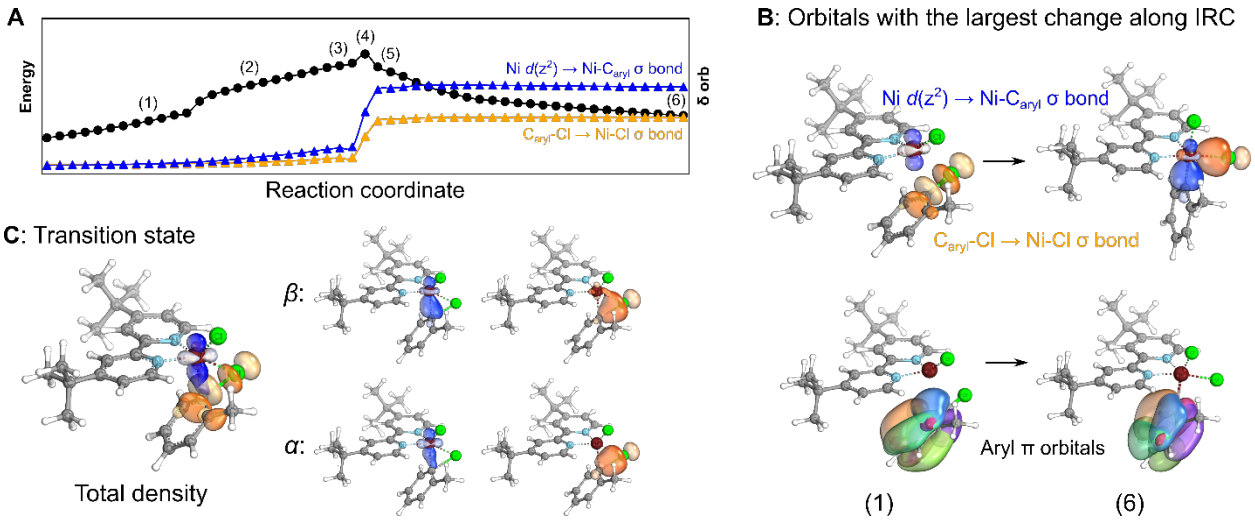

Figure S39. Intrinsic bond orbital analysis. A. The IBOs from the electronic structure of the starting material are continuously transformed to IBOs of the product, following the classical S_N2-type reactivity with Ni nucleophilic attack at the Cl–Tol carbon center. B. Orbitals with the largest change along IRC. Note that aryl π orbitals are changed due to different bonding in the reactants and product, but they are not reactive. C. The reaction is more involved at the transition state following the change in the β orbitals as the result of higher β-3d(z^2) orbital energy.

S2.4. Molecular Orbital Diagrams, Energetics, and Correlations

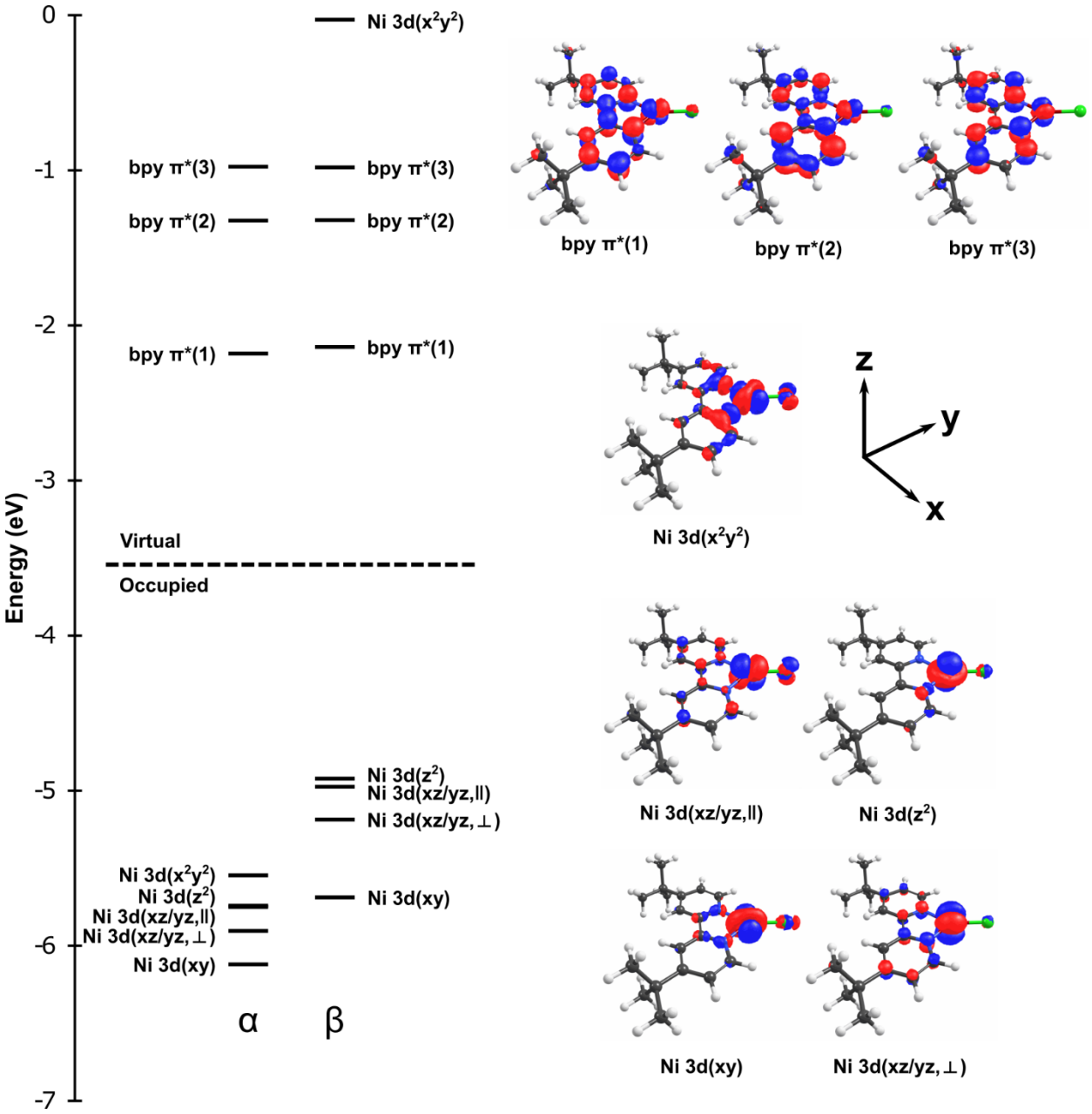

Figure S40. Molecular orbital diagram for **1-Cl** at the DFT(B3LYP) level. Note that d(xz) and d(yz) orbitals are bisecting the Ni–N(bpy) bonds; to keep the orbitals consistent with the parent square-planar Ni(II) complex, we thus label these orbitals based on their parallel (||) or perpendicular (⊥) orientation along the Ni–halide bond, while maintaining the x and y axes along the Ni–N(bpy).

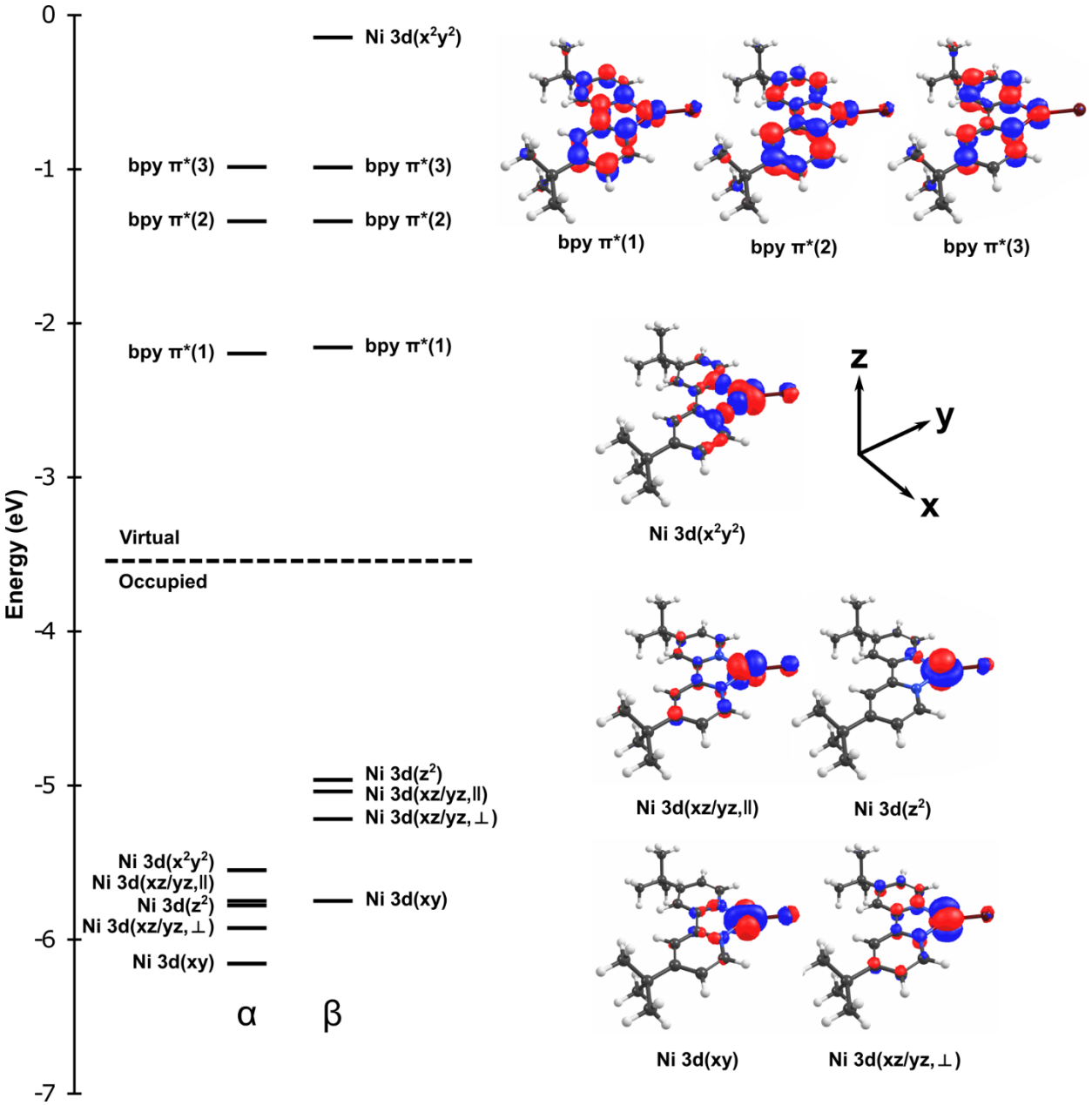

Figure S41. Molecular orbital diagram for **1-Br** at the DFT(B3LYP) level. Note that d(xz) and d(yz) orbitals are bisecting the Ni–N(bpy) bonds; to keep the orbitals consistent with the parent square-planar Ni(II) complex, we thus label these orbitals based on their parallel (∥) or perpendicular (⊥) orientation along the Ni–halide bond, while maintaining the x and y axes along the Ni–N(bpy).

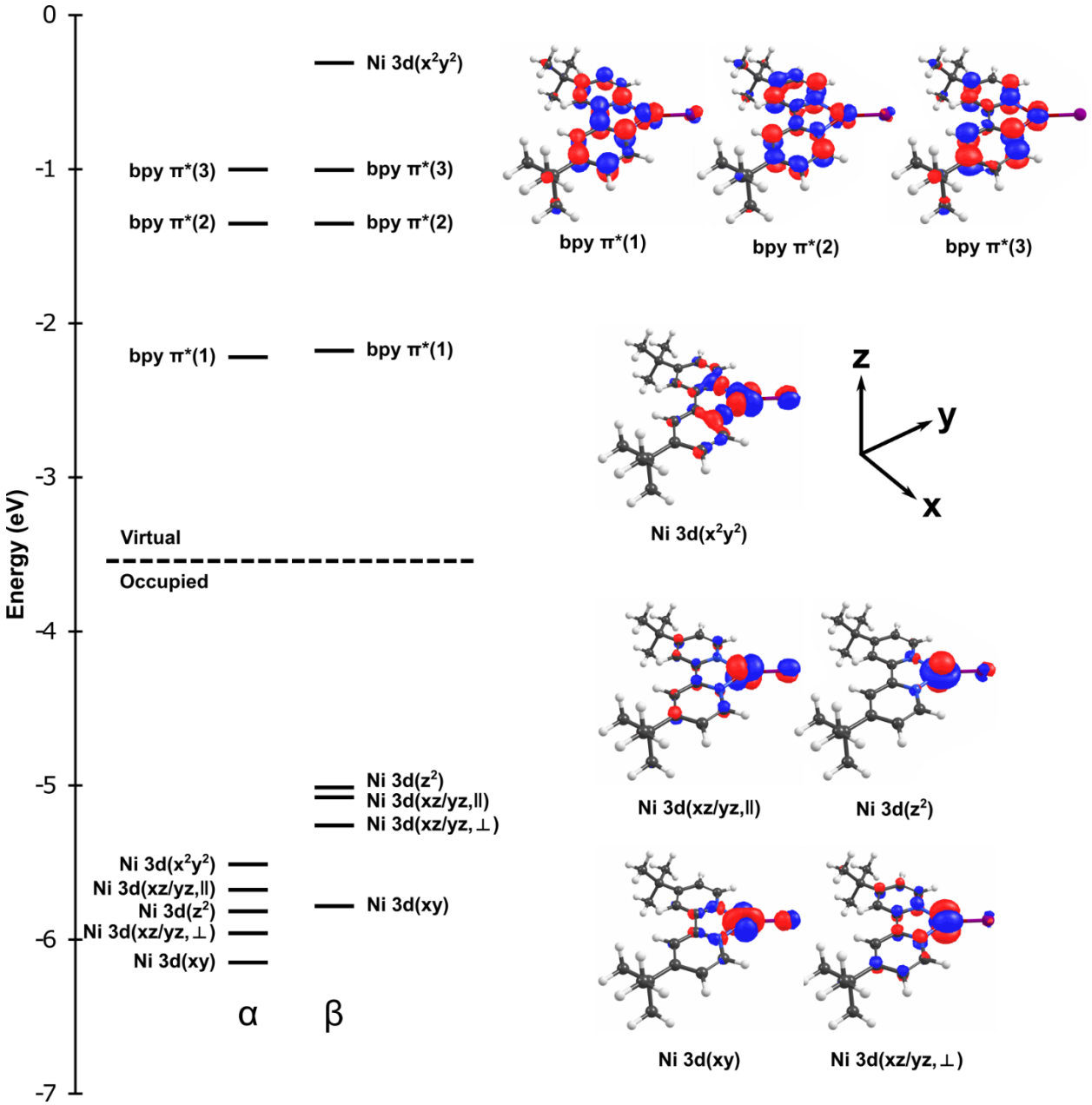

Figure S42. Molecular orbital diagram for **1-I** at the DFT(B3LYP) level. Note that d(xz) and d(yz) orbitals are bisecting the Ni–N(bpy) bonds; to keep the orbitals consistent with the parent square-planar Ni(II) complex, we thus label these orbitals based on their parallel (||) or perpendicular (⊥) orientation along the Ni–halide bond, while maintaining the x and y axes along the Ni–N(bpy).

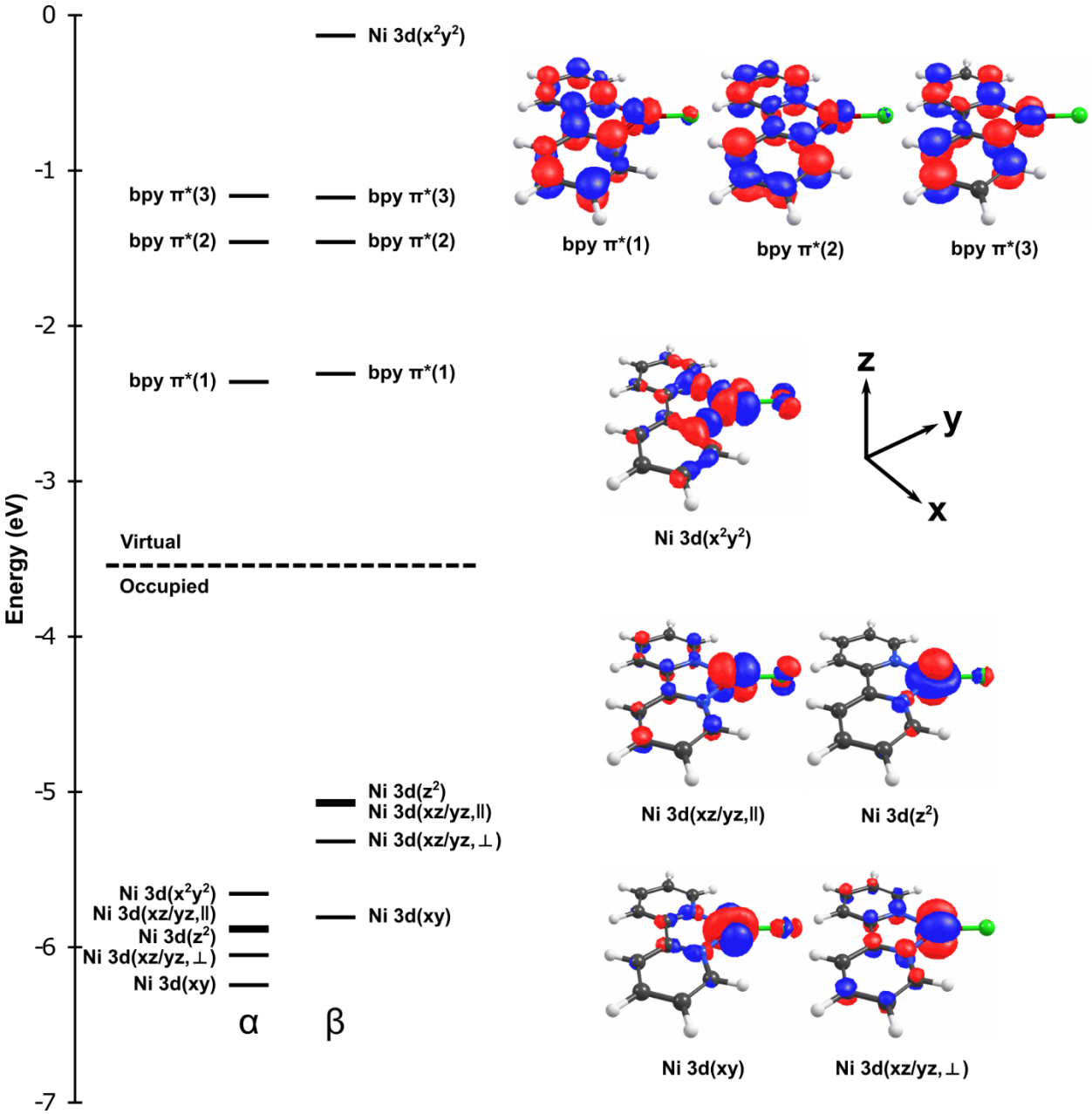

Figure S43. Molecular orbital diagram for **2-Cl** at the DFT(B3LYP) level. Note that d(xz) and d(yz) orbitals are bisecting the Ni–N(bpy) bonds; to keep the orbitals consistent with the parent square-planar Ni(II) complex, we thus label these orbitals based on their parallel (||) or perpendicular (⊥) orientation along the Ni–halide bond, while maintaining the x and y axes along the Ni–N(bpy).

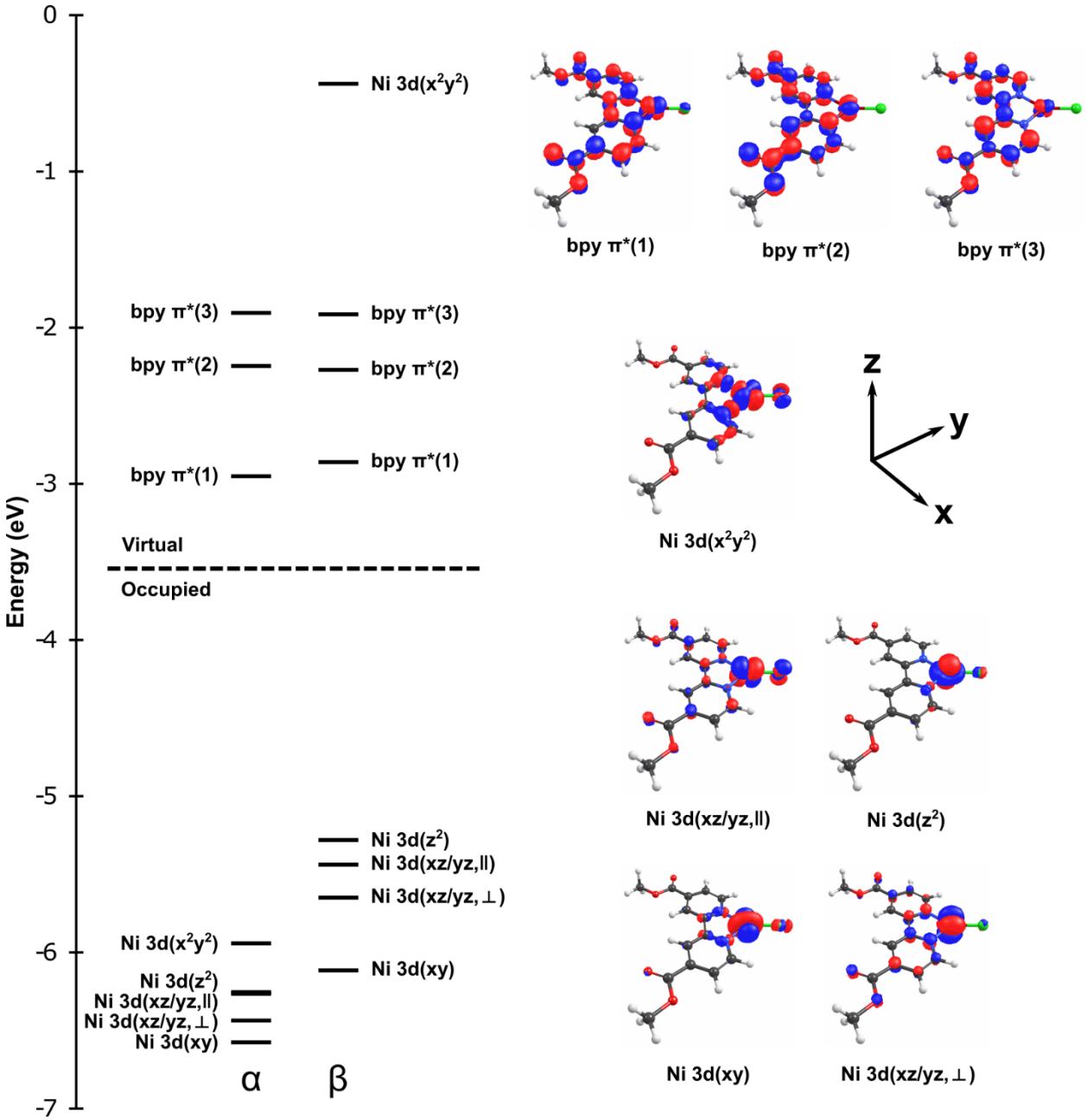

Figure S44. Molecular orbital diagram for **3-Cl** at the DFT(B3LYP) level. Note that d(xz) and d(yz) orbitals are bisecting the Ni–N(bpy) bonds; to keep the orbitals consistent with the parent square-planar Ni(II) complex, we thus label these orbitals based on their parallel (∥) or perpendicular (⊥) orientation along the Ni–halide bond, while maintaining the x and y axes along the Ni–N(bpy).

Table S7. DFT(B3LYP) orbital energies of various Ni(I) complexes. All energies are in eV.

α orbitals	**1-Cl**	**1-Br**	**1-I**	**2-Cl**	**3-Cl**
bpy π*(3)	-0.98	-0.99	-1.01	-1.17	-1.91
bpy π*(2)	-1.33	-1.34	-1.36	-1.46	-2.25
bpy π*(1)	-2.18	-2.20	-2.22	-2.36	-2.96
Ni 3d(x^2-y^2)	-5.55	-5.55	-5.52	-5.66	-5.95
Ni 3d(z^2)	-5.74	-5.78	-5.82	-5.87	-6.26
Ni 3d(xz/yz, ‖)	-5.75	-5.75	-5.68	-5.90	-6.27
Ni 3d(xz/yz, ⊥)	-5.90	-5.93	-5.96	-6.05	-6.44
Ni 3d(xy)	-6.12	-6.16	-6.15	-6.25	-6.58

β orbitals	**1-Cl**	**1-Br**	**1-I**	**2-Cl**	**3-Cl**
bpy π*(3)	-0.98	-0.99	-1.01	-1.18	-1.92
bpy π*(2)	-1.32	-1.34	-1.36	-1.46	-2.27
bpy π*(1)	-2.14	-2.16	-2.18	-2.31	-2.87
Ni 3d(x^2-y^2)	-0.03	-0.15	-0.31	-0.14	-0.44
Ni 3d(z^2)	-4.92	-4.97	-5.02	-5.06	-5.44
Ni 3d(xz/yz, ‖)	-4.98	-5.04	-5.08	-5.09	-5.28
Ni 3d(xz/yz, ⊥)	-5.19	-5.22	-5.26	-5.32	-5.65
Ni 3d(xy)	-5.69	-5.75	-5.79	-5.81	-6.12

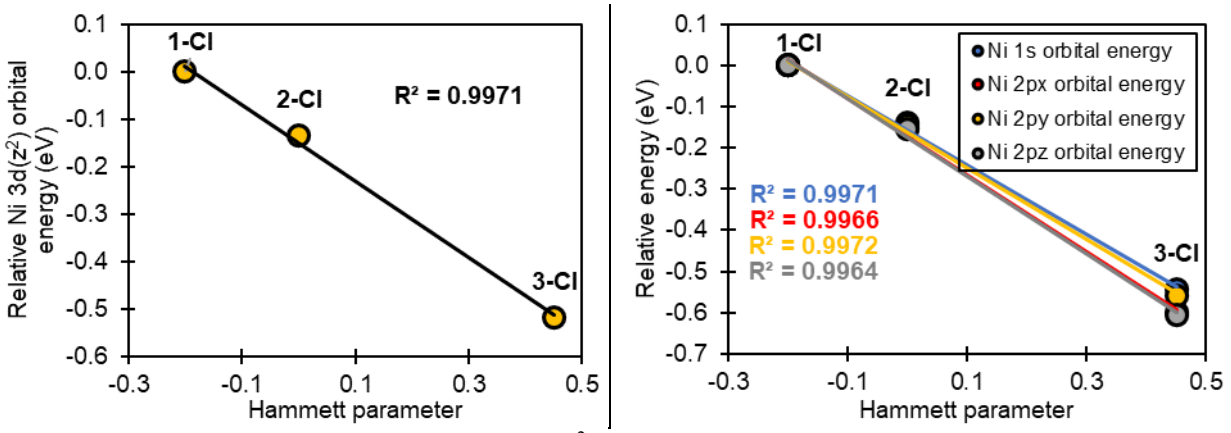

Figure S45. *Left*. Correlation between the Ni 3d(z^2) orbital energies of **1-Cl**, **2-Cl**, and **3-Cl** and Hammett parameters of their bipyridine substituents. *Right*. Correlation between the Ni core orbital (Ni(I) 1*s* and 2*p*(x,y,z)) energies of **1-Cl**, **2-Cl**, and **3-Cl** and Hammett parameters of their bipyridine substituents. The orbital energies are plotted as the energy change as referenced to the energy of the orbitals of **1-Cl** complex (i.e., with tert-Bu substituents on the bipyridine).

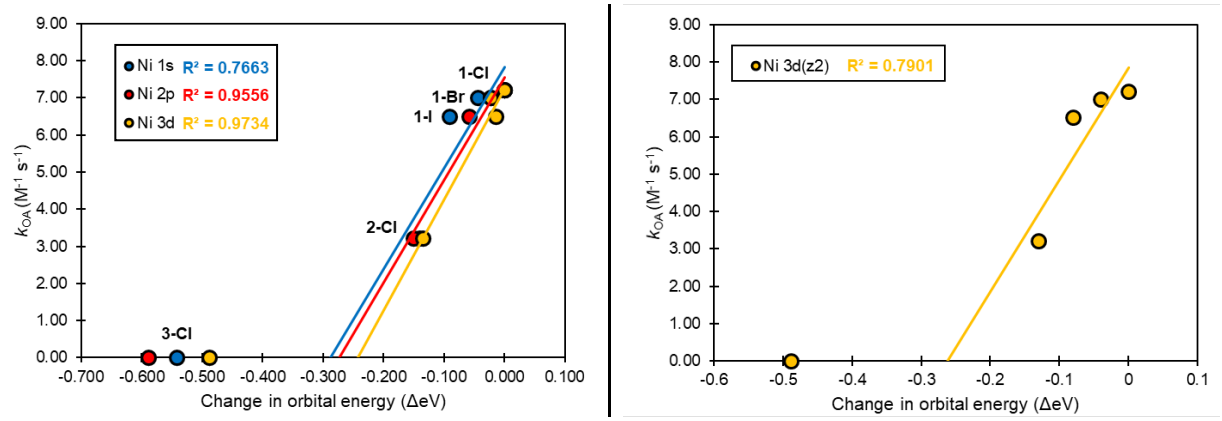

Figure S46. Plots of the oxidative addition rate constants, k_{OA}, vs the change in the Ni α-orbital energies relative to **1-Cl**. *Left*. Changes in the energies of Ni 1*s*, 2*p*, and 3*d*-orbital are plotted. Note that the 2*p*-orbital energies are averaged from $2p_x$, $2p_y$, $2p_z$ and 3*d*-orbital energies are averaged from $3d(x^2\text{-}y^2)$, $3d(z^2)$, 3*d*(xy), 3*d*(xz), 3*d*(yz). *Right*. Change in the Ni $3d(z^2)$ orbital energy is plotted.

S2.5. TDDFT Spectra and Tabulated Transitions

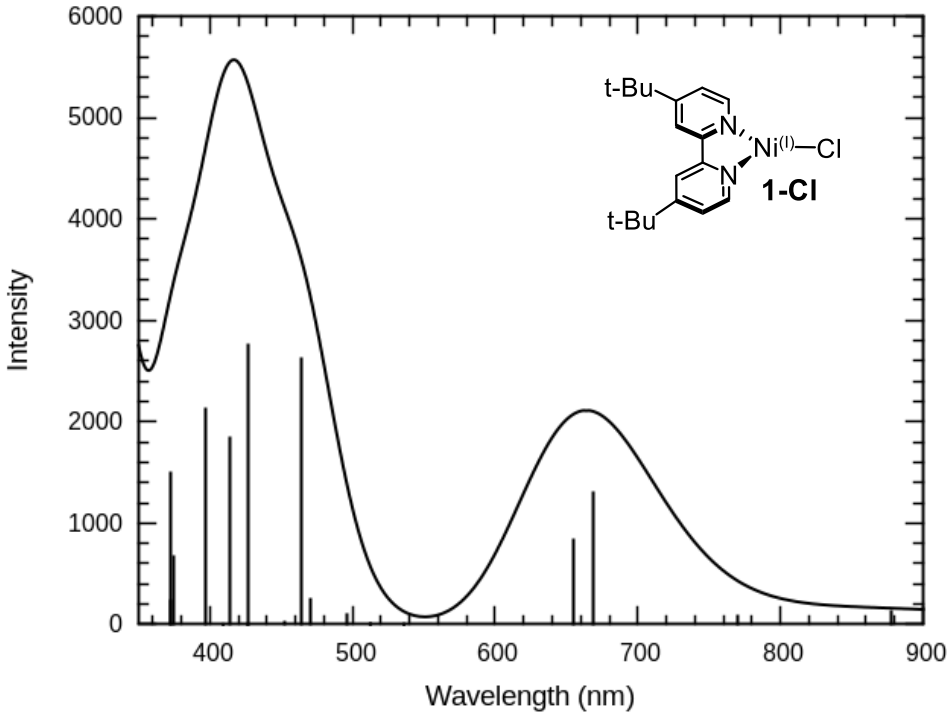

Figure S47. Calculated UV-vis spectrum for the equilibrium structure of **1-Cl** at the TDDFT (B3LYP) level with the CPCM(THF) solvation model.

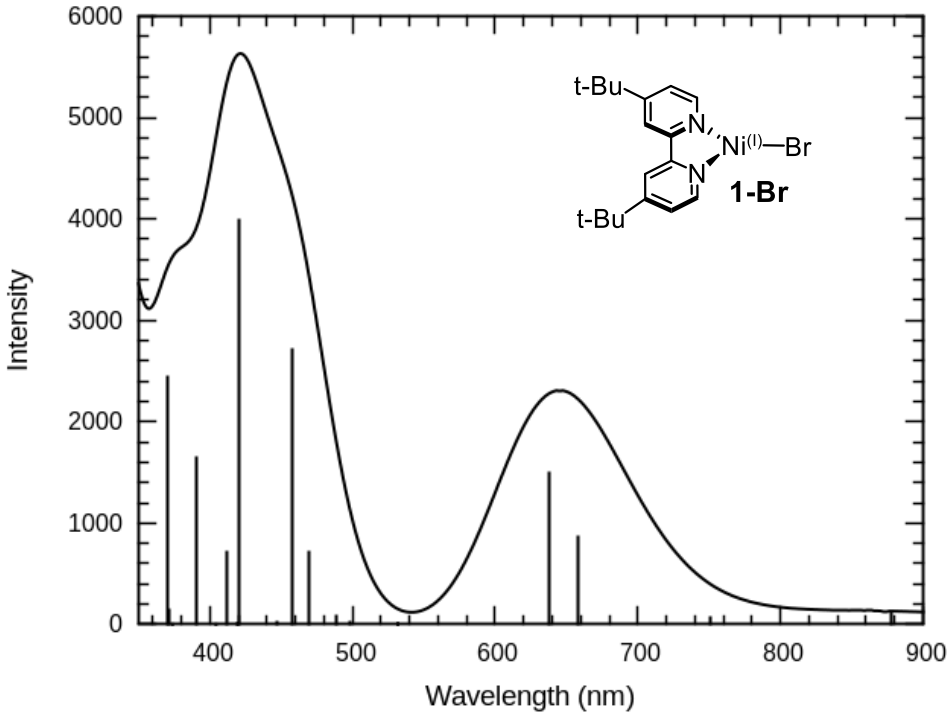

Figure S48. Calculated UV-vis spectrum for the equilibrium structure of **1-Br** at the TDDFT (B3LYP) level with the CPCM(THF) solvation model.

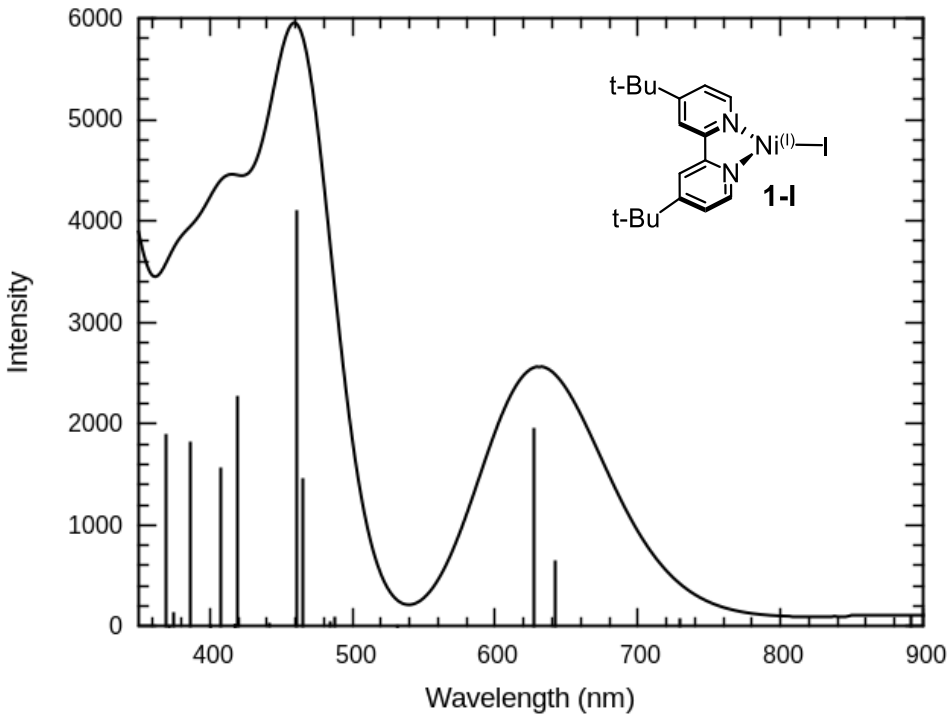

Figure S49. Calculated UV-vis spectrum for the equilibrium structure of **1-I** at the TDDFT (B3LYP) level with the CPCM(THF) solvation model.

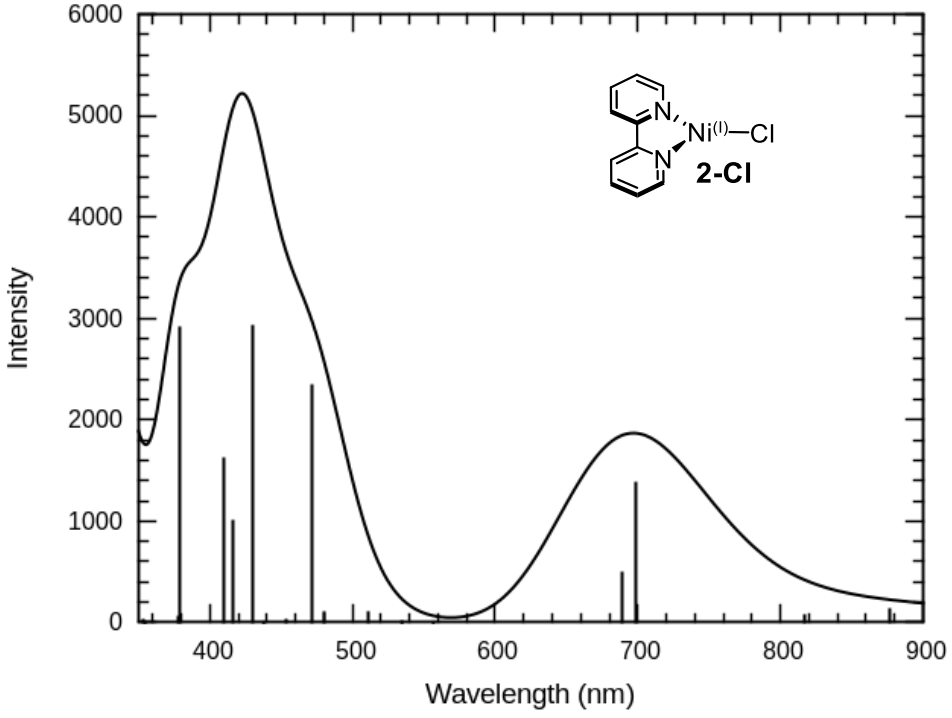

Figure S50. Calculated UV-vis spectrum for the equilibrium structure of **2-Cl** at the TDDFT (B3LYP) level with the CPCM(THF) solvation model.

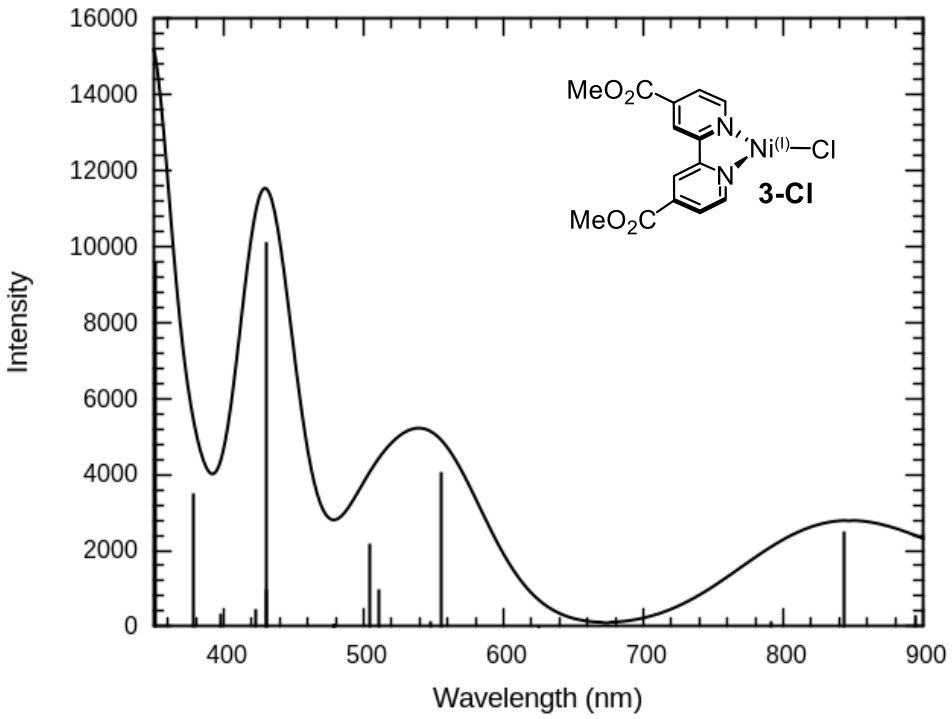

Figure S51. Calculated UV-vis spectrum for the equilibrium structure of **3-Cl** at the TDDFT (B3LYP) level with the CPCM(THF) solvation model.

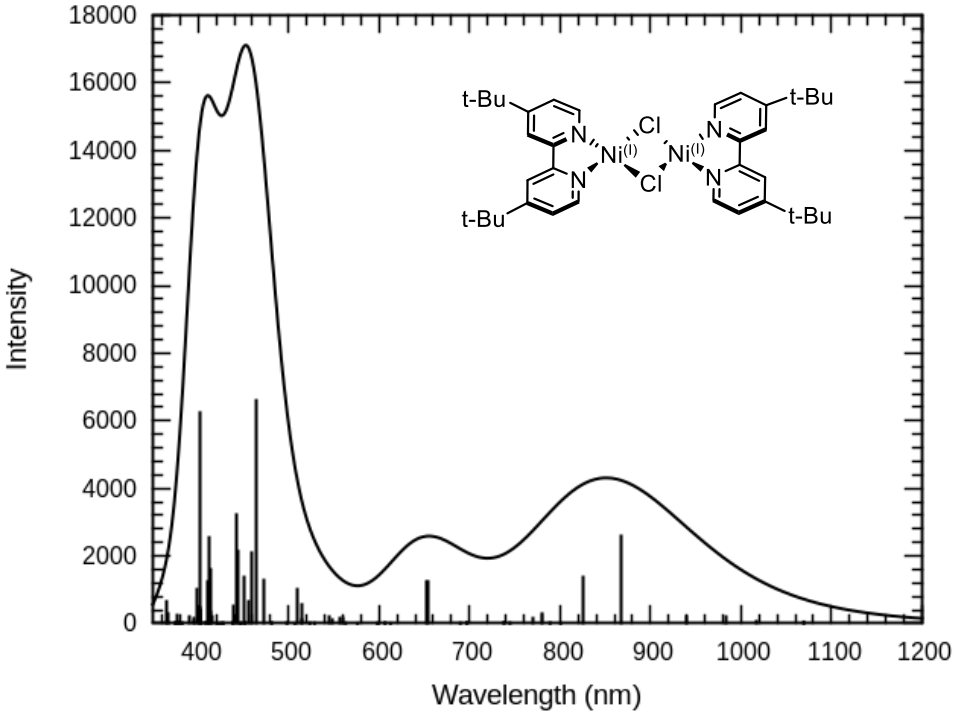

Figure S52. Calculated UV-vis spectrum of the 'flat' dimer generated from **1-Cl** at the TDDFT (B3LYP) level with the CPCM(THF) solvation model.

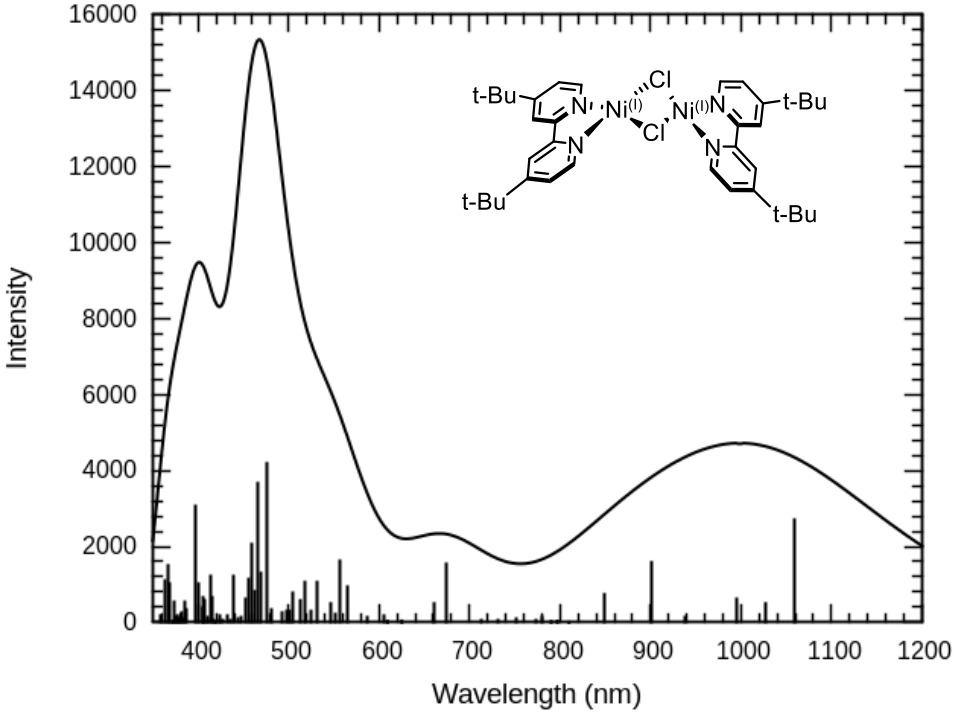

Figure S53. Calculated UV-vis spectrum of the 'peaked' dimer generated from **1-Cl** at the TDDFT (B3LYP) level with the CPCM(THF) solvation model.

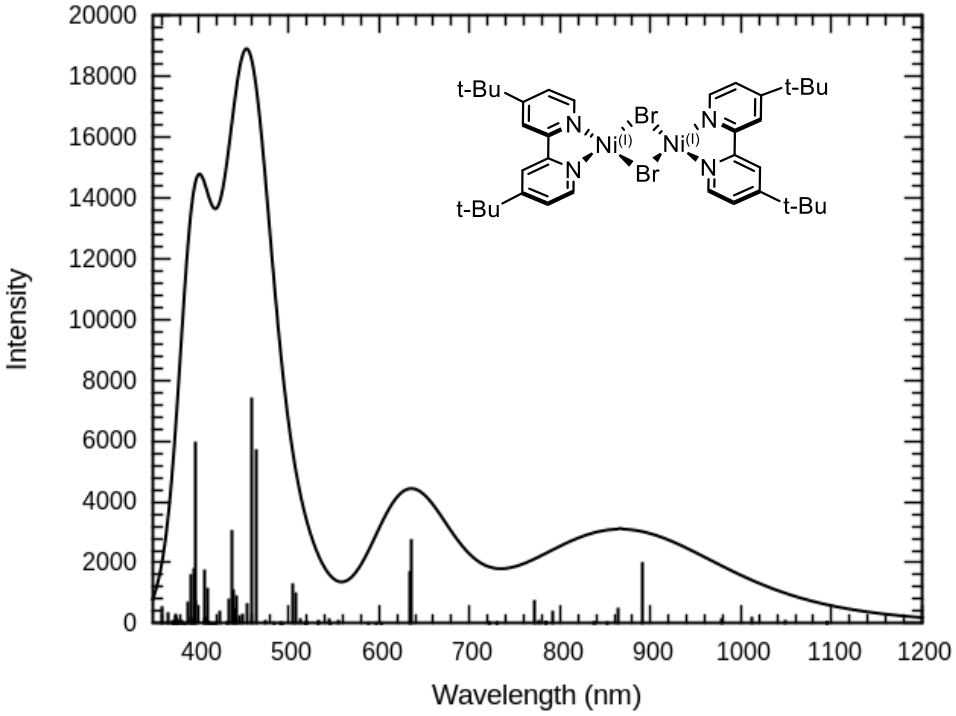

Figure S54. Calculated UV-vis spectrum of the 'flat' dimer generated from **1-Br** at the TDDFT (B3LYP) level with the CPCM(THF) solvation model.

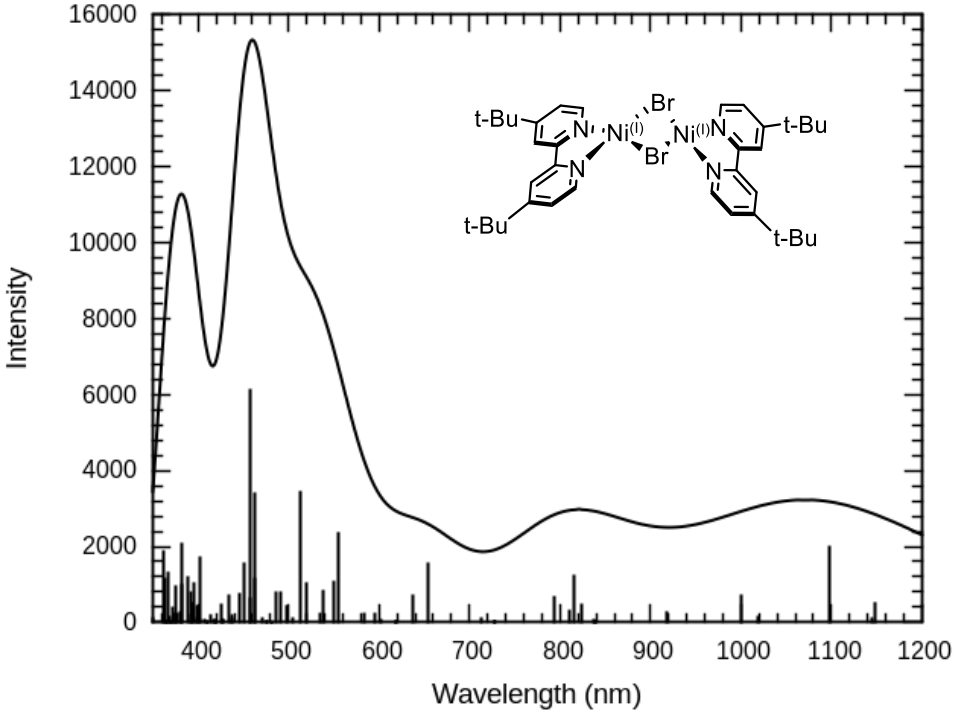

Figure S55. Calculated UV-vis spectrum of the 'peaked' dimer generated from **1-Br** at the TDDFT (B3LYP) level with the CPCM(THF) solvation model.

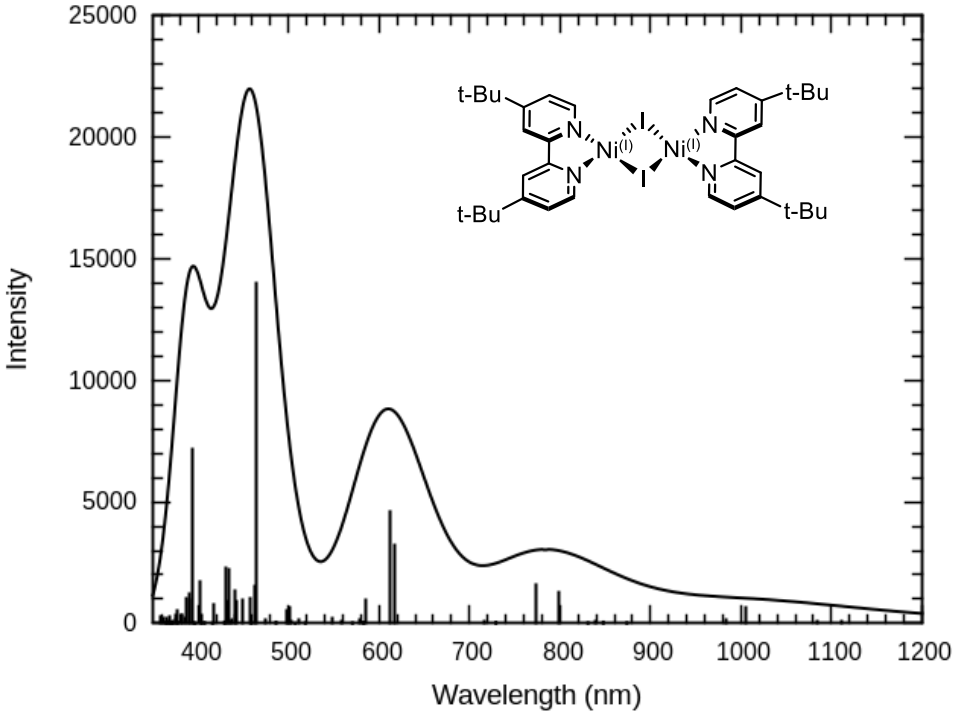

Figure S56. Calculated UV-vis spectrum of the 'flat' dimer generated from **1-I** at the TDDFT (B3LYP) level with the CPCM(THF) solvation model.

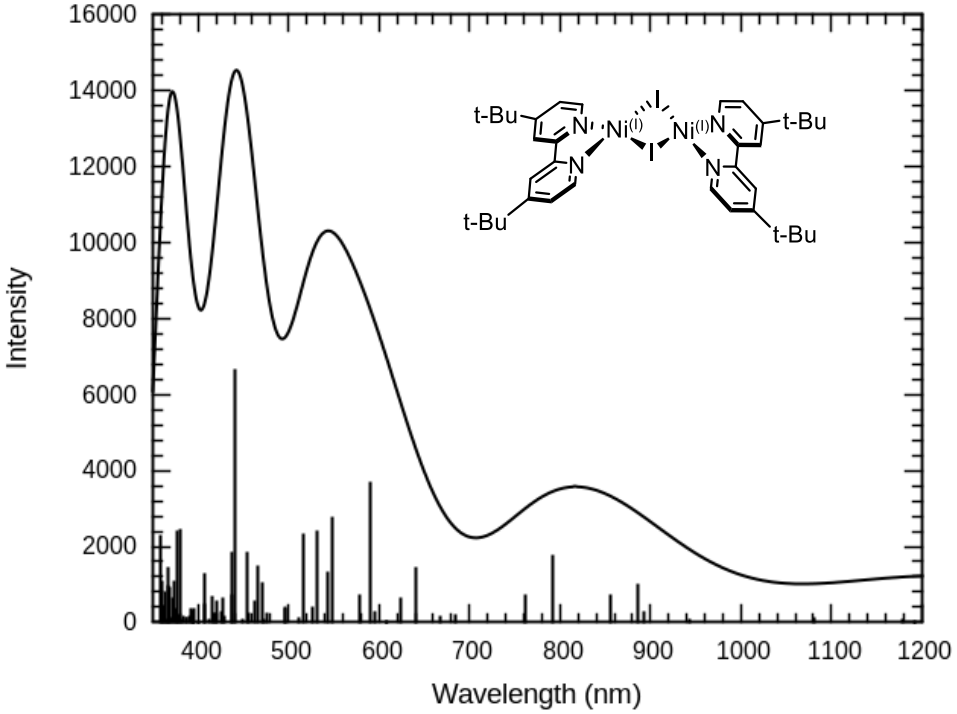

Figure S57. Calculated UV-vis spectrum of the 'peaked' dimer generated from **1-I** at the TDDFT (B3LYP) level with the CPCM(THF) solvation model.

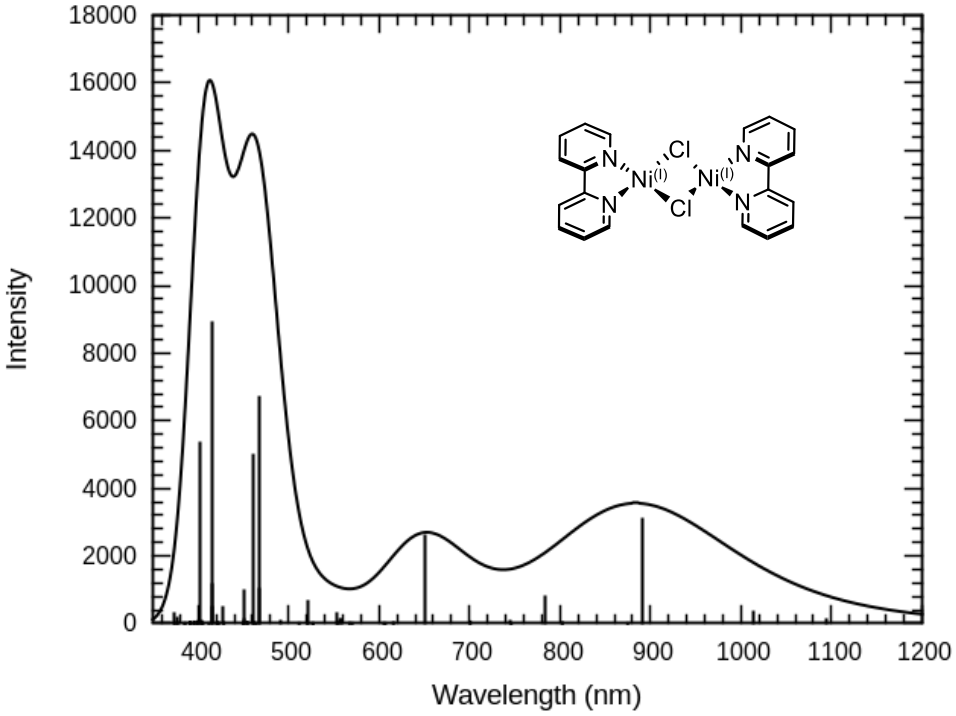

Figure S58. Calculated UV-vis spectrum of the 'flat' dimer generated from **2-Cl** at the TDDFT (B3LYP) level with the CPCM(THF) solvation model.

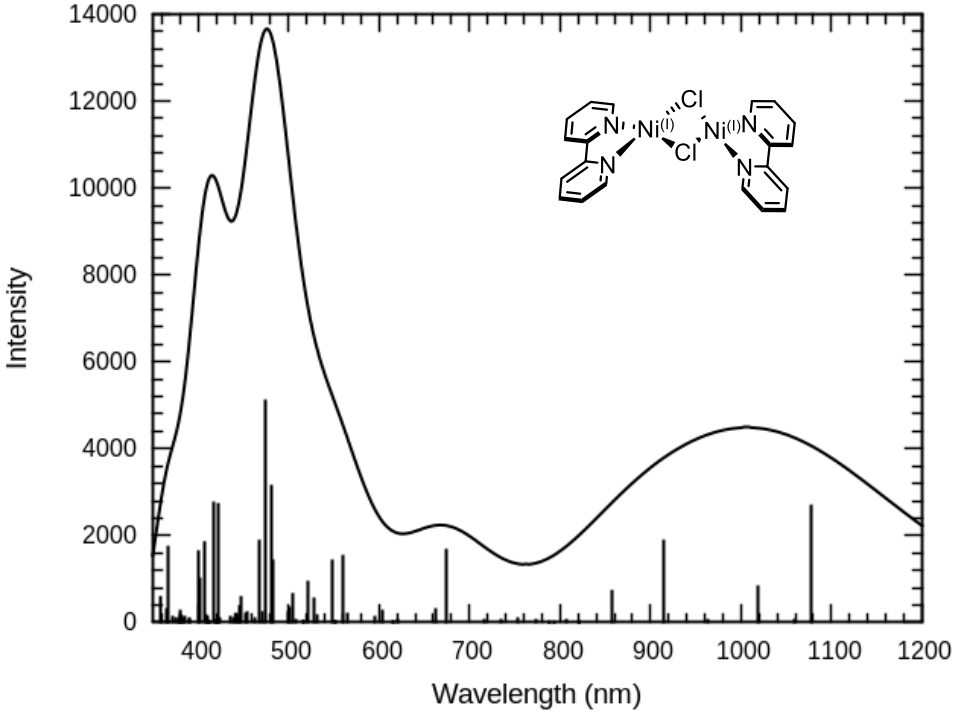

Figure S59. Calculated UV-vis spectrum of the 'peaked' dimer generated from **2-Cl** at the TDDFT (B3LYP) level with the CPCM(THF) solvation model.

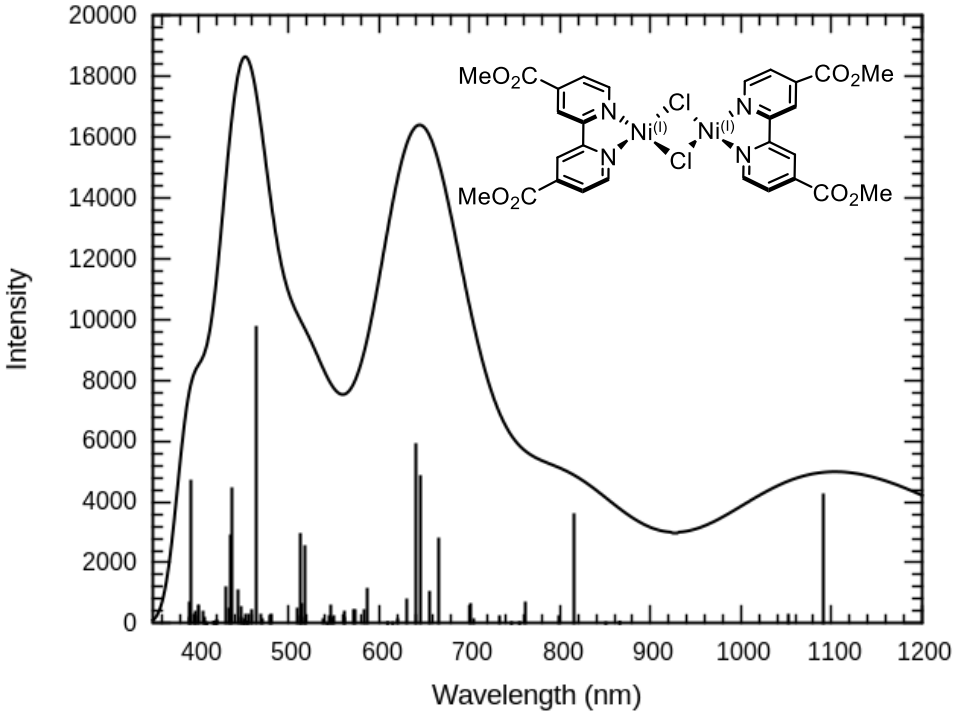

Figure S60. Calculated UV-vis spectrum of the 'flat' dimer generated from **3-Cl** at the TDDFT (B3LYP) level with the CPCM(THF) solvation model.

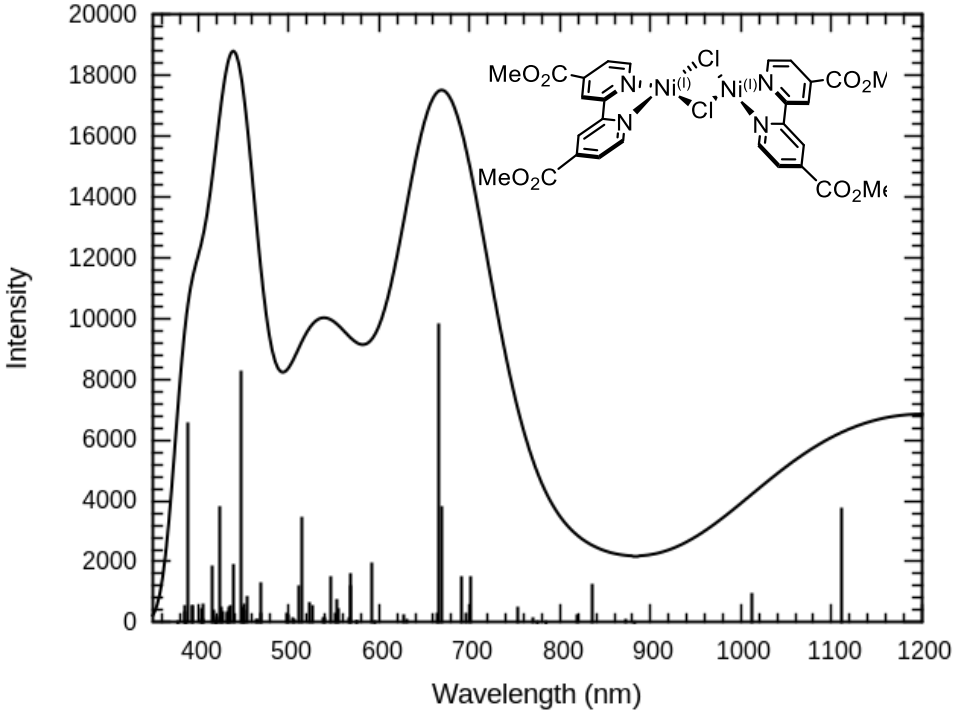

Figure S61. Calculated UV-vis spectrum of the 'peaked' dimer generated from **3-Cl** at the TDDFT (B3LYP) level with the CPCM(THF) solvation model.

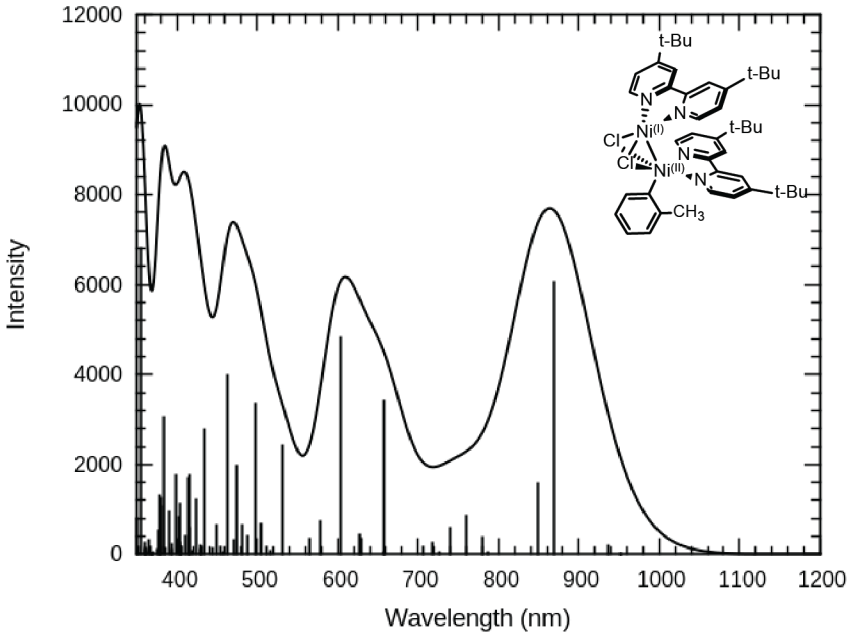

Figure S62. Calculated UV-vis spectrum of the [Ni(I)/Ni(II)] dimer generated from reacting **1-Cl** with the parent Ni(II)($^{t\text{-Bu}}$bpy)(*o*-tolyl)Cl at the TDDFT (B3LYP) level with the CPCM(THF) solvation model.

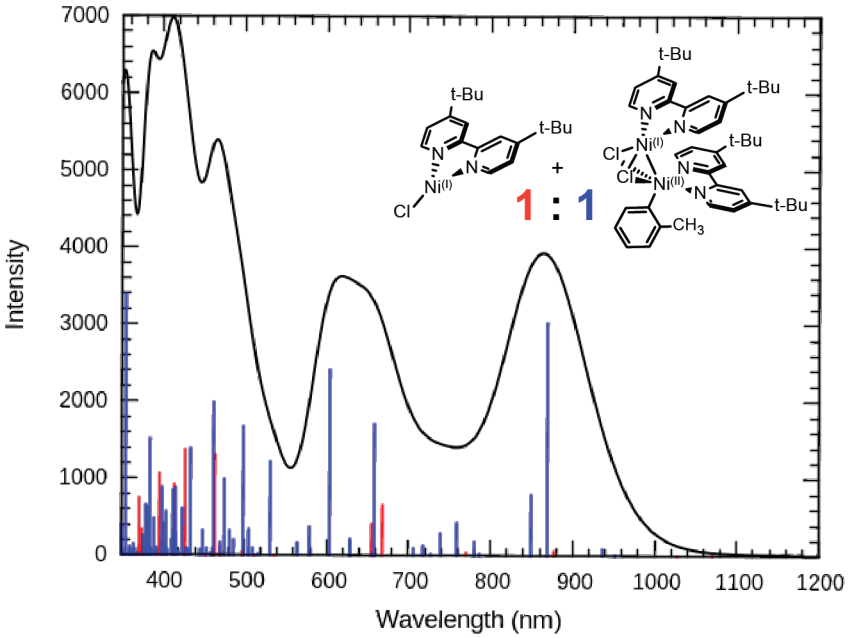

Figure S63. Calculated UV-vis spectrum of **1-Cl** and the [Ni(I)/Ni(II)] dimer generated from reacting **1-Cl** with the parent Ni(II)($^{t\text{-Bu}}$bpy)(*o*-tolyl)Cl in the ratio of 1:1 at the TDDFT (B3LYP) level with the CPCM(THF) solvation model.

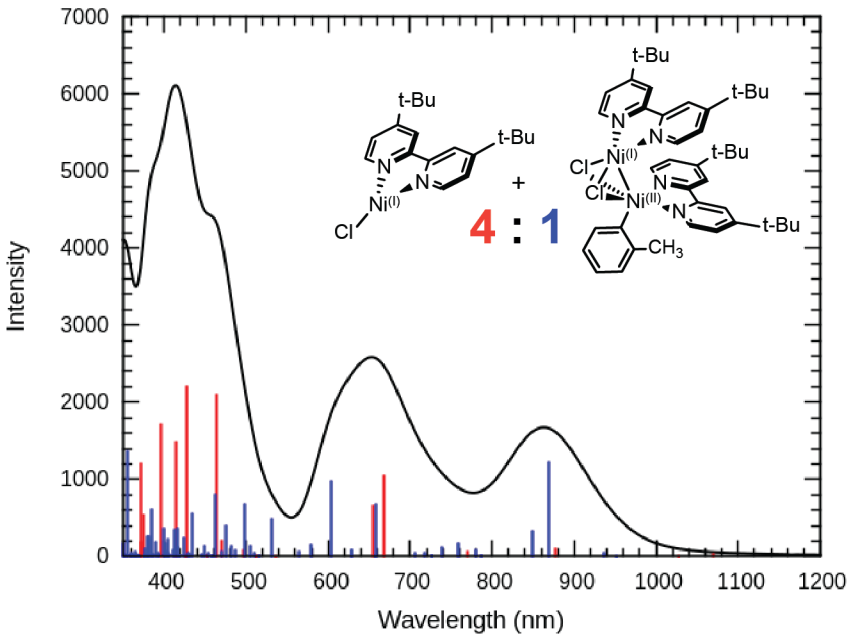

Figure S64. Calculated UV-vis spectrum of **1-Cl** and the [Ni(I)/Ni(II)] dimer generated from reacting **1-Cl** with the parent Ni(II)($^{t\text{-Bu}}$bpy)(*o*-tolyl)Cl in the ratio of 4:1 at the TDDFT (B3LYP) level with the CPCM(THF) solvation model.

Table S8. Absorption transitions for the equilibrium structure of **1-Cl** at the TDDFT(B3LYP) level with the CPCM(THF) solvation model.

State	E/cm^{-1}	E/nm	f_{osc}	Assignment
1	9342	1071	0.0004093	β-Ni 3d(z^2) → β-Ni 3d(x^2-y^2)
2	9731	1028	0.0000517	β-Ni 3d(xz/yz,⊥) → β-Ni 3d(x^2-y^2)
3	10768	929	0.0000016	β-Ni 3d(xz/yz,∥) → β-Ni 3d(x^2-y^2)
4	11394	878	0.0014232	β-Ni 3d(xy) → β-Ni 3d(x^2-y^2)
5	12989	770	0.0008731	β-Ni 3d(z^2) → β-π*(1)
6	14959	669	0.0149121	β-Ni 3d(xz/yz,∥) → β-π*(1)
7	15258	655	0.0095299	β-Ni 3d(xz/yz,⊥) → β-π*(1)
8	18654	536	0.0000425	α-Ni 3d(x^2-y^2) → α-π*(1)
9	19513	513	0.0000976	β-Ni 3d(xy) → β-π*(1)
10	20163	496	0.0010822	α-Ni 3d(z^2) → α-π*(1)
11	21250	471	0.0027619	α-Ni 3d(xz/yz,⊥) → α-π*(1)
12	21550	464	0.0301730	α-Ni 3d(xz/yz,∥) → α-π*(1)
13	22098	453	0.0002474	β-Ni 3d(z^2) → β-π*(2)
14	23401	427	0.0317360	β-Ni 3d(xz/yz,∥) → β-π*(2)
15	23442	427	0.0000273	α-Ni 3d(xy) → α-π*(1)
16	24180	414	0.0212063	β-Ni 3d(xz/yz,⊥) → β-π*(2)
17	24432	409	0.0000056	β-Ni 3d(z^2) → β-π*(3)
18	25186	397	0.0245216	β-Ni 3d(xz/yz,∥) → β-π*(3)
19	26718	374	0.0077156	α-π → α-π*(1)
20	26864	372	0.0172151	β-Ni 3d(xz/yz,⊥) → β-π*(3)
21	26884	372	0.0026728	α-Ni 3d(x^2-y^2) → α-π*(2)
22	28370	353	0.0000002	β-Ni 3d(xy) → β-π*(2)

Table S9. Absorption transitions for the equilibrium structure of **1-Br** at the TDDFT(B3LYP) level with the CPCM(THF) solvation model.

State	E/cm^{-1}	E/nm	f_{osc}	Assignment
1	8912	1122	0.0003999	β-Ni 3d(z^2) → β-Ni 3d(x^2-y^2)
2	9366	1068	0.0000572	β-Ni 3d(xz/yz,⊥) → β-Ni 3d(x^2-y^2)
3	10611	942	0.0000095	β-Ni 3d(xz/yz,∥) → β-Ni 3d(x^2-y^2)
4	11399	877	0.0012904	β-Ni 3d(xy) → β-Ni 3d(x^2-y^2)
5	13313	751	0.0008386	β-Ni 3d(z^2) → β-π*(1)
6	15206	658	0.0098878	β-Ni 3d(xz/yz,⊥) → β-π*(1)
7	15675	638	0.0172284	β-Ni 3d(xz/yz,∥) → β-π*(1)
8	18806	532	0.0001137	α-Ni 3d(x^2-y^2) → α-π*(1)
9	20079	498	0.0001965	β-Ni 3d(xy) → β-π*(1)
10	20451	489	0.0009620	α-Ni 3d(z^2) → α-π*(1)
11	21307	469	0.0081174	α-Ni 3d(xz/yz,⊥) → α-π*(1)
12	21856	458	0.0312229	α-Ni 3d(xz/yz,∥) → α-π*(1)
13	22349	448	0.0002499	β-Ni 3d(z^2) → β-π*(2)
14	23759	421	0.0460045	β-Ni 3d(xz/yz,∥) → β-π*(2)
15	23851	419	0.0001131	α-Ni 3d(xy) → α-π*(1)
16	24301	412	0.0081566	β-Ni 3d(xz/yz,⊥) → β-π*(2)
17	24737	404	0.0000136	β-Ni 3d(z^2) → β-π*(3)
18	25571	391	0.0189379	β-Ni 3d(xz/yz,∥) → β-π*(3)
19	26753	374	0.0000166	α-π → α-π*(1)
20	26963	371	0.0016411	α-Ni 3d(x^2-y^2) → α-π*(2)
21	27037	370	0.0281544	β-Ni 3d(xz/yz,⊥) → β-π*(3)

Table S10. Absorption transitions for the equilibrium structure of **1-I** at the TDDFT(B3LYP) level with the CPCM(THF) solvation model.

State	E/cm^{-1}	E/nm	f_{osc}	Assignment
1	8277	1208	0.0002910	β-Ni 3d(z^2) → β-Ni 3d(x^2-y^2)
2	8838	1132	0.0000570	β-Ni 3d(xz/yz,⊥) → β-Ni 3d(x^2-y^2)
3	10262	975	0.0000007	β-Ni 3d(xz/yz,∥) → β-Ni 3d(x^2-y^2)
4	11213	892	0.0011739	β-Ni 3d(xy) → β-Ni 3d(x^2-y^2)
5	13698	730	0.0007835	β-Ni 3d(z^2) → β-π*(1)
6	15582	642	0.0073844	β-Ni 3d(xz/yz,⊥) → β-π*(1)
7	15941	627	0.0223901	β-Ni 3d(xz/yz,∥) → β-π*(1)
8	18816	532	0.0000213	α-Ni 3d(x^2-y^2) → α-π*(1)
9	20514	488	0.0009253	β-Ni 3d(xy) → β-π*(1)
10	20624	485	0.0003878	α-Ni 3d(z^2) → α-π*(1)
11	21483	466	0.0167038	α-Ni 3d(xz/yz,⊥) → α-π*(1)
12	21677	461	0.0472389	α-Ni 3d(xz/yz,∥) → α-π*(1)
13	22642	442	0.0003175	β-Ni 3d(z^2) → β-π*(2)
14	23832	420	0.0260560	β-Ni 3d(xz/yz,∥) → β-π*(2)
15	23945	418	0.0001339	α-Ni 3d(xy) → α-π*(1)
16	24547	407	0.0178325	β-Ni 3d(xz/yz,⊥) → β-π*(2)
17	24976	400	0.0000578	β-Ni 3d(z^2) → β-π*(3)
18	25922	386	0.0209118	β-Ni 3d(xz/yz,∥) → β-π*(3)
19	26732	374	0.0014182	α-π → α-π*(1)
20	26921	372	0.0000211	α-Ni 3d(x^2-y^2) → α-π*(2)
21	27115	369	0.0216714	β-Ni 3d(xz/yz,⊥) → β-π*(3)

Table S11. Absorption transitions for the equilibrium structure of **2-Cl** at the TDDFT(B3LYP) level with the CPCM(THF) solvation model.

State	E/cm^{-1}	E/nm	f_{osc}	Assignment
1	9389	1065	0.0004564	β-Ni 3d(z^2) → β-Ni 3d(x^2-y^2)
2	9791	1021	0.0000317	β-Ni 3d(xz/yz,⊥) → β-Ni 3d(x^2-y^2)
3	10952	913	0.0000003	β-Ni 3d(xz/yz,∥) → β-Ni 3d(x^2-y^2)
4	11415	876	0.0014430	β-Ni 3d(xy) → β-Ni 3d(x^2-y^2)
5	12238	817	0.0008286	β-Ni 3d(z^2) → β-π*(1)
6	14313	699	0.0159057	β-Ni 3d(xz/yz,∥) → β-π*(1)
7	14512	689	0.0055488	β-Ni 3d(xz/yz,⊥) → β-π*(1)
8	17964	557	0.0000091	α-Ni 3d(x^2-y^2) → α-π*(1)
9	18703	535	0.0000804	β-Ni 3d(xy) → β-π*(1)
10	19588	511	0.0011314	α-Ni 3d(z^2) → α-π*(1)
11	20816	480	0.0011049	α-Ni 3d(xz/yz,⊥) → α-π*(1)
12	21223	471	0.0269910	α-Ni 3d(xz/yz,∥) → α-π*(1)
13	22059	453	0.0001977	β-Ni 3d(z^2) → β-π*(2)
14	22845	438	0.0000112	α-Ni 3d(xy) → α-π*(1)
15	23260	430	0.0336255	β-Ni 3d(xz/yz,∥) → β-π*(2)
16	23794	420	0.0000003	β-Ni 3d(z^2) → β-π*(3)
17	24010	417	0.0114265	β-Ni 3d(xz/yz,⊥) → β-π*(2)
18	24375	410	0.0185067	β-Ni 3d(xz/yz,∥) → β-π*(3)
19	26400	379	0.0334554	α-Ni 3d(x^2-y^2) → α-π*(2)
20	26460	378	0.0005935	α-π → α-π*(1)
21	26649	375	0.0000040	β-Ni 3d(xz/yz,⊥) → β-π*(3)
22	28202	355	0.0000262	β-Ni 3d(xy) → β-π*(2)
23	28311	353	0.0002561	α-Ni 3d(x^2-y^2) → α-π*(3)

Table S12. Absorption transitions for the equilibrium structure of **3-Cl** at the TDDFT(B3LYP) level with the CPCM(THF) solvation model.

State	E/cm^{-1}	E/nm	f_{osc}	Assignment
1	9077	1102	0.0001541	β-Ni 3d(z^2) → β-π*(1)
2	9167	1091	0.0033551	β-Ni 3d(z^2) → β-Ni 3d(x^2-y^2)
3	10385	963	0.0004445	β-Ni 3d(xz/yz,⊥) → β-Ni 3d(x^2-y^2)
4	11176	895	0.0030595	β-Ni 3d(xy) → β-Ni 3d(x^2-y^2)
5	11349	881	0.0000069	β-Ni 3d(xz/yz,‖) → β-Ni 3d(x^2-y^2)
6	11860	843	0.0284840	β-Ni 3d(xz/yz,‖) → β-π*(1)
7	12640	791	0.0010937	β-Ni 3d(xz/yz,⊥) → β-π*(1)
8	15991	625	0.0000288	β-Ni 3d(xy) → β-π*(1)
9	16038	624	0.0000043	α-Ni 3d(x^2-y^2) → α-π*(1)
10	17995	556	0.0462390	β-Ni 3d(xz/yz,‖) → β-π*(2)
11	18259	548	0.0009887	α-Ni 3d(z^2) → α-π*(1)
12	18815	532	0.0000006	β-Ni 3d(z^2) → β-π*(2)
13	19556	511	0.0107873	β-Ni 3d(xz/yz,⊥) → β-π*(2)
14	19830	504	0.0246536	α-Ni 3d(xz/yz,⊥) → α-π*(1)
15	20891	479	0.0003752	β-Ni 3d(xz/yz,‖) → β-π*(3)
16	21177	472	0.0000015	α-Ni 3d(xy) → α-π*(1)
17	22194	451	0.0000025	β-Ni 3d(z^2) → β-π*(3)
18	23234	430	0.0108947	α-Ni 3d(x^2-y^2) → α-π*(2)
19	23252	430	0.1159463	α-Ni 3d(xz/yz,‖) → α-π*(1)
20	23666	423	0.0050143	β-Ni 3d(xz/yz,⊥) → β-π*(3)
21	24521	408	0.0000004	β-Ni 3d(xy) → β-π*(2)
22	25112	398	0.0032968	α-π → α-π*(1)
23	25860	387	0.0000005	α-Ni 3d(z^2) → α-π*(2)
24	26051	384	0.0000004	α-Ni 3d(x^2-y^2) → α-π*(3)
25	26471	378	0.0398278	α-Ni 3d(xz/yz,‖) → α-π*(2)
26	27783	360	0.0000089	β-Ni 3d(xy) → β-π*(3)
27	28461	351	0.1102159	α-Ni 3d(xz/yz,⊥) → α-π*(2)

S2.6. DFT Reactivity Investigations – Oxidative Addition and Dimerization

We used DFT calculations to evaluate key intermediates along the reaction coordinate for the oxidative addition of various aryl halides to three-coordinate Ni(I)(^{R}bpy)X species. The free energy barriers correlate with the strengths of the Ar–X bonds with the trend of $\Delta G^{\neq}$ = 2-*Cl*-Tol > 2-*Br*-Tol > 2-*I*-Tol. The major difference in the reactivity of Ni(I)(^{R}bpy)X species arises in the variation of the bpy substituents, with the most electron-withdrawing methyl ester, increasing the $\Delta G^{\neq}$.

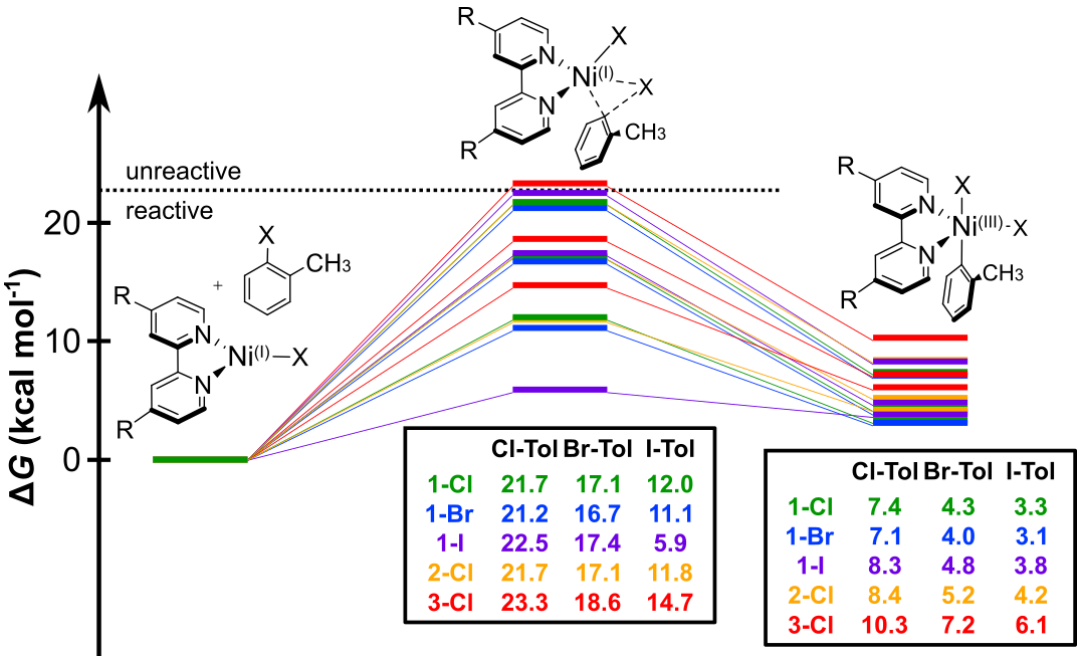

	Cl-Tol	Br-Tol	I-Tol
1-Cl	21.7	17.1	12.0
1-Br	21.2	16.7	11.1
1-I	22.5	17.4	5.9
2-Cl	21.7	17.1	11.8
3-Cl	23.3	18.6	14.7

	Cl-Tol	Br-Tol	I-Tol
1-Cl	7.4	4.3	3.3
1-Br	7.1	4.0	3.1
1-I	8.3	4.8	3.8
2-Cl	8.4	5.2	4.2
3-Cl	10.3	7.2	6.1

Figure S65. DFT energetics of the oxidative addition reactions of Ni(I)(^{R}bpy)X with tolyl halides. Relative Gibbs free energy values were computed at the DFT(B3LYP) level with the CPCM(THF) solvation model.

We note that comproportionation step in **1-Br** and **1-I** reactivity with 2-*chloro*-toluene can yield various mixed-halide products, i.e., possibly resulting in parent Ni(II)($^{t\text{-Bu}}$bpy)(*o*-tolyl)Cl, instead of regenerating Ni(II)($^{t\text{-Bu}}$bpy)(*o*-tolyl)Br and Ni(II)($^{t\text{-Bu}}$bpy)(*o*-tolyl)I parent species. Similarly, the produced Ni(II) dihalide can contain two chlorides or mixed chloride and bromide/iodine. For simplicity, we have considered the original halide to be transferred to Ni(I) during comproportionation, generating Ni(II)($^{t\text{-Bu}}$bpy)(*o*-tolyl)Cl and mixed-halide Ni(II) dihalide species; the original halide appears to be more accessible for transfer from Ni(III), as it resides in the axial position after the oxidative addition step.

We next investigated the kinetic dependence of the substituents on the aryl chloride substrates and performed a computational Hammett analysis on the reactivity of series of para-substituted aryl chlorides with **1-Cl.**

The natural logarithm of the ratio between k_x and k_H rate constants was obtained from the Eyring equation, assuming the same transmission coefficients κ for both reactions:

$$k = \frac{\kappa k_B T}{h} e^{\frac{-\Delta G^{\neq}}{RT}} \qquad \textbf{(eq. S11)}$$

$$\ln\left(\frac{k_x}{k_H}\right) = \frac{\Delta G_H^{\neq} - \Delta G_x^{\neq}}{RT} \qquad \textbf{(eq. S12)}$$

The computed slope of the Hammett plot of ρ ~5.8 is consistent with the experimental observation of ρ = 5.2, suggesting an S_NAr-type activation of the C(sp^2)–Cl bond by Ni(I) nucleophilic attack.

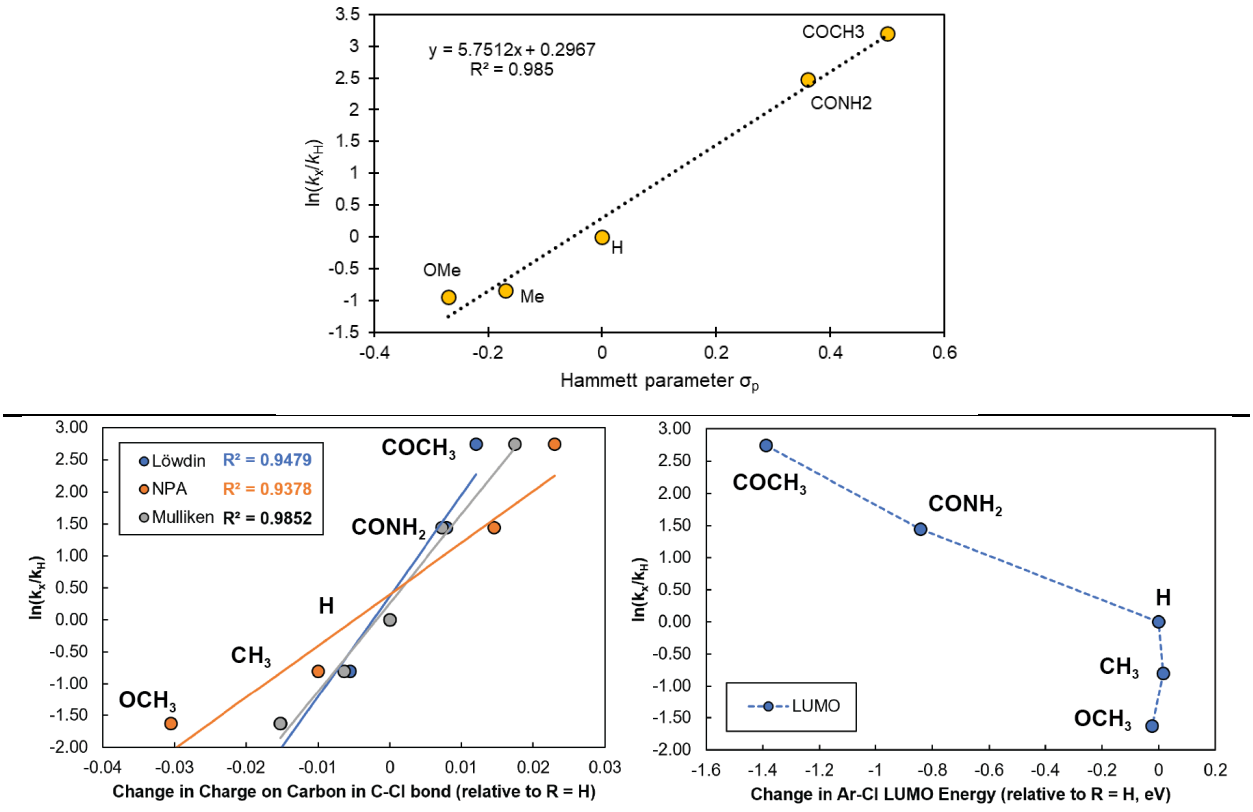

Figure S66. *Top.* Computational Hammett analysis for the reaction of **1-Cl** with 4-substituted aryl chlorides. *Bottom*. Comparison of experimental oxidative addition rate constants to computed values, the (*left*) atomic charges at the carbon in the Ar–Cl bond and (*right*) LUMO energy of the free aryl chlorides.

A slope of ρ > 4 also suggests the possibility of the reactivity through a single-electron transfer (SET) from Ni(I) to aryl halides. We note, however, we now observe that the experimental rate constants trend linearly and positively with the Löwdin atomic charges, the Mulliken atomic charges, and the natural population

analysis (NPA) charges at the carbon in the Ar–Cl bond, but they do not trend well with the energy of the LUMO of the aryl chlorides (Figure S66). This observation is indicative of the electrophilicity of this carbon being related to the rate and not the reduction potential of the aryl chlorides.

Furthermore, we find that the electrochemical reduction potentials of all aryl halides are computed to be too negative to be accessed directly by **1-Cl**, suggesting the single-electron transfer is unfeasible, consistent with the proposed S_NAr oxidative addition mechanism. The computed data are in agreement with the experimental reduction potentials of the *o*-tolyl halides in Section S1.6, which demonstrate that only 2-*iodo*-toluene is reduced in the solvent window at the reduction potential of –2.7 V vs. $Fc^{+/0}$. The irreversibility of the 2-*iodo*-toluene reduction is likely due to dissociation of iodide as also predicted by DFT computations. We also examined both a structure with 2-*chloro*-toluene coordinated to **1-Cl** and the stacked structure shown in Figure 5A to evaluate if the Ni(I) complexes could activate the aryl halide substrates and facilitate SET (Figure S67). Notably, we find that the first unoccupied orbital on the aryl chlorides increase by ~70 or 100 mV when either coordinated or stacked to the Ni(I), respectively, making them even more challenging to reduce. Furthermore, the coordinated **1-Cl** + chlorotoluene structure is 11 kcal mol^{-1} higher than the separated reagents, making it unlikely to form in solution.

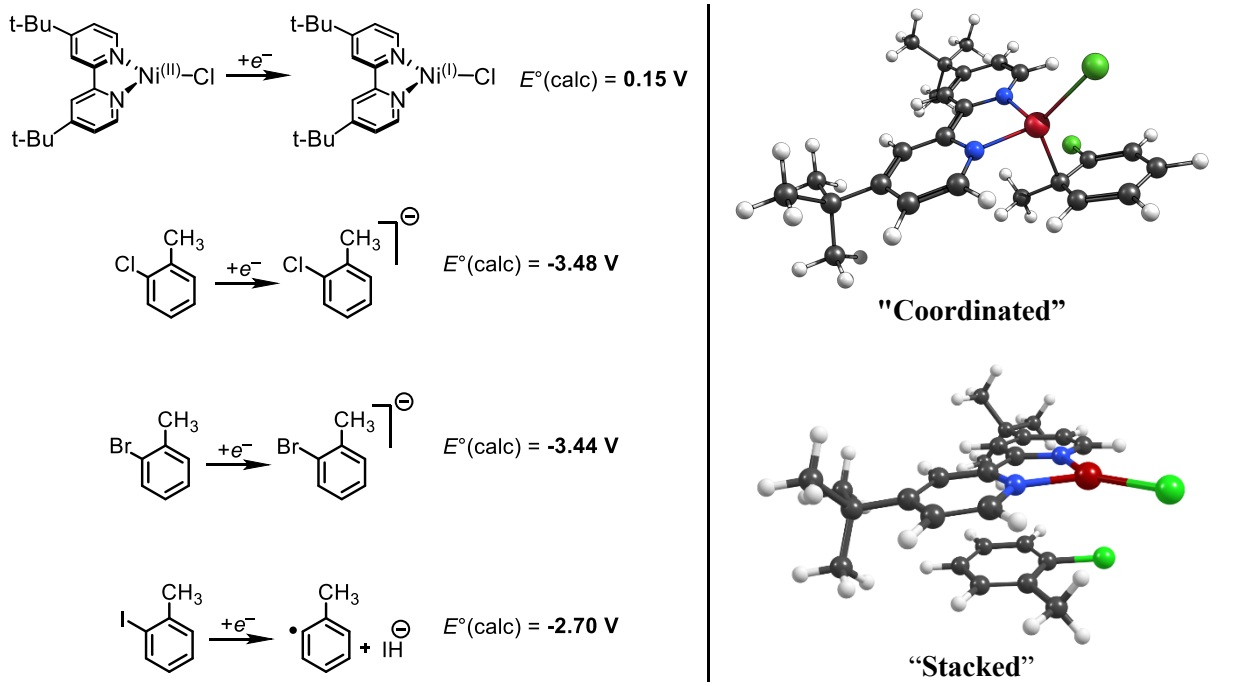

Figure S67. *Left.* Calculated reduction potentials of Ni(II)(^{tBu}bpy)(*o*-tolyl)Cl and *o*-tolyl halides, referenced to the absolute potential of the ferrocenium/ferrocene couple, computed at –4.51 eV in THF, using the same methodology. Experimental data shown in Figure S11. *Right*. The structure of the **1-Cl** + 2-*chloro*-toluene coordinated (*top right)* and stacked (*bottom right,* also depicted in main text Figure 5A). The first unoccupied orbital on the aryl chloride increases in energy by ~70-100 mV in either the coordinated or stacked structure vs the free aryl halide, indicating that prior coordination or stacking of the aryl halide to the low valent d^9 Ni(I) center would likely serve to partially reduce the aryl halide by backdonation from the Ni to the unoccupied Ar–Cl antibonding orbitals and further disfavor SET.

Table S13. Energetics of the oxidative addition reactivity of 2-*chloro*-toluene to Ni(I) complexes at the DFT(B3LYP) level with the CPCM(THF) solvation model. All energies are in kcal mol^{-1} and referenced to the energy of separated reagents.

Compounds	Reactant complex	Transition state	Pentacoordinate Ni(III) intermediate	Separated products of comproportionation
1-Cl + 2-*chloro*-toluene	1.0	21.7	7.4	-25.0
1-Br + 2-*chloro*-toluene	0.2	21.2	7.1	-23.0
1-I + 2-*chloro*-toluene	1.3	22.5	8.3	-20.6
2-Cl + 2-*chloro*-toluene	2.4	21.7	8.4	-24.3
3-Cl + 2-*chloro*-toluene	0.8	23.3	10.3	-21.6

Table S14. Structure analysis of the oxidative addition reactivity of 2-*chloro*-toluene to Ni(I) complexes at the DFT(B3LYP) level with the CPCM(THF) solvation model. All bond lengths are in Å.

Compound	Tricoordinate Ni(I)				
	Ni–N(1)	Ni–N(2)	Ni–X(1)	Ni–C	Ni–X(2)
1-Cl	1.926	1.934	2.146	---	---
1-Br	1.924	1.929	2.285	---	---
1-I	1.925	1.930	2.452	---	---
2-Cl	1.926	1.929	2.144	---	---
3-Cl	1.919	1.923	2.139	---	---
Compounds	**Transition State**				
	Ni–N(1)	**Ni–N(2)**	**Ni–X(1)**	**Ni–C**	**Ni–X(2)**
1-Cl + 2-*chloro*-toluene	1.974	2.014	2.282	2.009	2.292
1-Br + 2-*chloro*-toluene	1.971	2.013	2.434	2.005	2.285
1-I + 2-*chloro*-toluene	1.967	2.013	2.614	2.001	2.278
2-Cl + 2-*chloro*-toluene	1.974	2.014	2.280	2.008	2.286
3-Cl + 2-*chloro*-toluene	1.967	2.008	2.273	2.008	2.271
Compounds	**Pentacoordinate Ni(III)**				
	Ni–N(1)	**Ni–N(2)**	**Ni–X(1)**	**Ni–C**	**Ni–X(2)**
1-Cl + 2-*chloro*-toluene	1.954	2.009	2.338	1.916	2.195
1-Br + 2-*chloro*-toluene	1.949	2.004	2.190	1.915	2.502
1-I + 2-*chloro*-toluene	1.941	2.000	2.184	1.913	2.715
2-Cl + 2-*chloro*-toluene	1.958	2.015	2.334	1.916	2.190
3-Cl + 2-*chloro*-toluene	1.957	2.016	2.328	1.916	2.185

Table S15. Calculated bond-dissociation free energies at the DFT (B3LYP) level with the CPCM(THF). All energies are in kcal mol^{-1}.

Ni(II)–C(aryl) homolytic dissociation	
Ni(II)(^{tBu}bpy)(*o*-tolyl)Cl → **1-Cl** + Tol$^{\bullet}$	31.8
Ni(II)(^{tBu}bpy)(*o*-tolyl)Br → **1-Br** + Tol$^{\bullet}$	30.4
Ni(II)(^{tBu}bpy)(*o*-tolyl)I → **1-I** + Tol$^{\bullet}$	30.5
Ni(II)(bpy)(*o*-tolyl)Cl → **2-Cl** + Tol$^{\bullet}$	31.7
Ni(II)(^{COOMe}bpy)(*o*-tolyl)Cl → **3-Cl** + Tol$^{\bullet}$	30.6
X–C(aryl) homolytic dissociation	
Cl–(*o*-tolyl) → Tol$^{\bullet}$ + Cl$^{\bullet}$	92.9
Br–(*o*-tolyl) → Tol$^{\bullet}$ + Br$^{\bullet}$	81.8
I–(*o*-tolyl) → Tol$^{\bullet}$ + I$^{\bullet}$	70.3

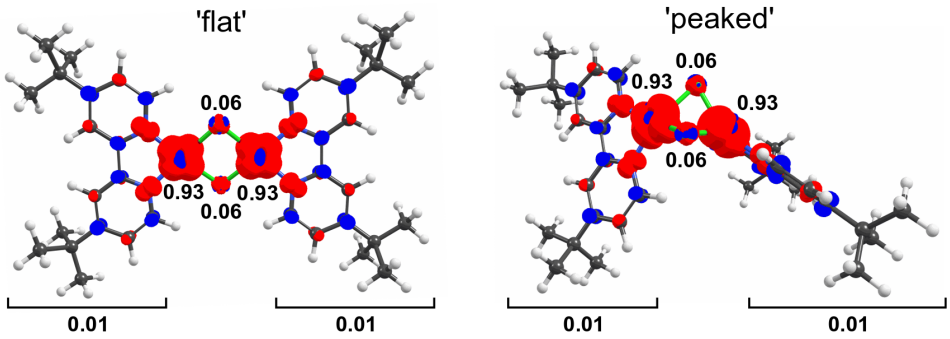

Figure S68. Spin density plots and Löwdin spin populations of 'flat' and 'peaked' [Ni(I)/Ni(I)] dimer geometries obtained at the DFT (B3LYP) level with the CPCM(THF) solvation model.

Table S16. Energetics of the dimerization of the Ni(I) complexes at the DFT(B3LYP) level with the CPCM(THF) solvation model. All energies are in kcal mol^{-1} and referenced to the energy of separated reagents.

	Transition state	**Peaked dimer**	**Flat dimer**
1-Cl	19.8	15.7	15.2
1-Br	21.0	19.4	19.1
1-I	21.7	20.9	20.6
2-Cl	17.3	16.7	14.4
3-Cl	17.6	14.4	14.3

Table S17. Properties of the [Ni(I)/Ni(I)] and oxidized (formally [Ni(I)/Ni(II)]) dimers obtained at the DFT (B3LYP) level with the CPCM(THF) solvation model.

Spin population	**Ni1**		**Ni2**		**Summation over bipyridines**		**Summation over Cl atoms**	
'flat' dimer [Ni(I)/Ni(I)]	0.93		0.93		0.02		0.12	
'peaked' dimer [Ni(I)/Ni(I)]	0.93		0.93		0.02		0.12	
'flat' dimer oxidized	1.33		1.28		0.18		0.20	
'peaked' dimer oxidized	1.31		1.31		0.20		0.17	
Bond distance (Å)	**Ni1–Cl1**	**Ni1–Cl2**	**Ni2–Cl1**	**Ni1–Cl2**	**Ni1–N1**	**Ni1–N2**	**Ni2–N3**	**Ni2–N4**
'flat' dimer [Ni(I)/Ni(I)]	2.35	2.35	2.36	2.35	1.96	1.96	1.96	1.96
'peaked' dimer [Ni(I)/Ni(I)]	2.34	2.36	2.36	2.34	1.97	1.97	1.97	1.96
'flat' dimer oxidized	2.33	2.31	2.33	2.31	1.99	1.99	2.00	1.99
'peaked' dimer oxidized	2.31	2.39	2.38	2.31	2.01	2.01	2.01	2.01
Reduction potential[a]								
'Ni(II)Ni(I)'/[Ni(I)/Ni(I)]	–0.72 V							

[a]Reduction potential is computed between the 'peaked' geometry of the oxidized dimer and the 'flat' geometry of the [Ni(I)/Ni(I)] dimer, which are predicted to have the lowest free energies. The potential is referenced to the absolute potential of the ferrocenium/ferrocene couple, computed at –4.51 eV in THF, using the same methodology.

S2.7. Additional Analysis of EPR Spectra

The EPR spectra of **1-Cl**, **1-Br**, and **1-I** display an unexpected twofold splitting of the high-field peak around 310 mT, whereas an axial Ni(I) would be expected to have a single unsplit g_z feature. Two explanations are readily suggested: (1) hyperfine splitting of the g_z feature, or (2) an additional g resonance from a second EPR active species. To investigate the former, ^{1}H and ^{14}N hyperfine coupling tensors were calculated for **1-Cl** by DFT using core basis sets. To account for potential hyperfine coupling to the protons of the THF solvent, a single THF molecule was included. Geometry optimization showed the THF could bind at the equatorial position (Figure S69).

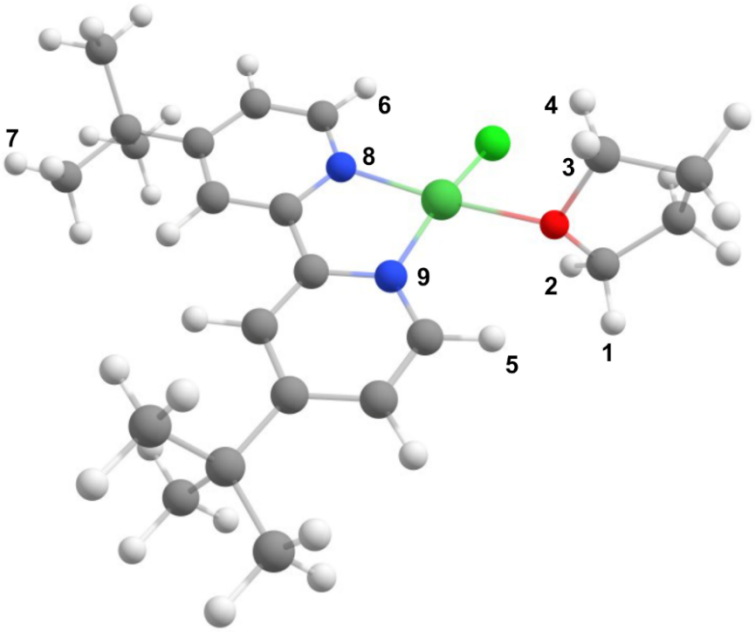

Figure S69. Input geometry of THF-bound **1-Cl** for DFT hyperfine calculation. Atoms included in the hyperfine tensor calculation are numbered.

The isotropic and dipolar hyperfine tensor contributions were calculated for atoms 1-9. Hydrogen atoms 1-6 and nitrogen atoms 8-9 could have large spin density buildup, while hydrogen 7 was included as a control. The principal values of the hyperfine tensor are reported in Table S18.

Table S18: DFT-calculated hyperfine couplings for THF-bound **1-Cl.**

Atom #	Atom type	A_1 (MHz)	A_2 (MHz)	A_3 (MHz)
1	H	-1.60	3.96	-1.45
2	H	7.57	-3.37	-3.62
3	H	-2.53	-2.26	4.45
4	H	7.72	-2.42	-2.72
5	H	2.32	15.38	3.99
6	H	1.17	12.12	1.89
7	H	0.30	0.01	0.02
8	N	37.10	29.19	27.21
9	N	27.57	20.88	18.78

All protons on the equatorially bound THF displayed small couplings (< 8 MHz) with anisotropy patterns consistent with point dipole-dipole interactions (principal values of 2T, –T, and –T). Stronger hyperfine couplings were observed for the nearest bipyridine protons (5-6) which possess couplings up to 15 MHz. These couplings possess significant isotropic hyperfine (average of A_1, A_2, and A_3 > 0 MHz), indicating spin density delocalization. As expected, the control hydrogen #7 displayed negligible hyperfine coupling. The strongest hyperfine couplings occur with the ligated nitrogen atoms (~20-40 MHz). However, none of the calculated couplings are capable of explaining the g_z peak splitting in **1-Cl**, which would require an $I = 1/2$ ^{1}H coupling of around 150 MHz. Therefore, the g_z peak splitting is not explained by hyperfine coupling.

To investigate the potential for a secondary S = 1/2 species, EasySpin simulations were conducted on **1-Cl** with two S = 1/2 spin systems. The additional features at ~310-315 mT could be satisfactorily fit using a second species with g = [2.165, 2.174, 2.203], with a relative weight of ~10% as compared to the main Ni(I) species assigned in the main text. This minority species could be attributable to weak solvent coordination effects from the 2-methyl-THF glass. We conclude that solvent coordination is the most likely explanation for the presence of additional features in the Ni(I) *g*-value region.

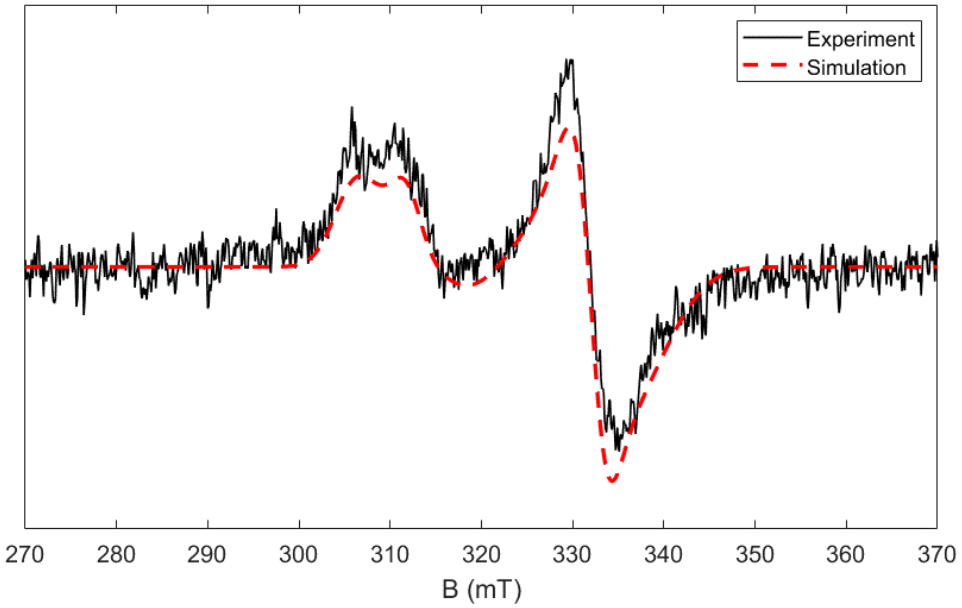

Figure S70. Fit to **1-Cl** EPR spectrum (9.637 GHz, 5 K, 2.2 mW, 8 G modulation amplitude, 2Me-THF) using two S = 1/2 species.

Table S19. Optimized parameters for the two-component fit to the **1-Cl** EPR spectrum.

Species	g_x	g_y	g_z	gStrain(x)	gStrain(y)	gStrain(z)	Spectral weight
#1	2.040	2.071	2.248	0.060	0.023	0.041	90.1 %
#2	2.165	2.174	2.203	0.069	0.068	0.023	9.9 %

S3. Additional NMR Data.

Proton nuclear magnetic resonance (^{1}H NMR) spectra were recorded on a 400 MHz Varian Spectrometer with broadband auto-tune OneProbe. All ^{13}C NMR spectra were collected on a Bruker AV-III HD 400 MHz spectrometer. ^{13}C NMR spectra were ^{1}H decoupled. Chemical shifts are reported in parts per million and are referenced to residual solvent signal (CD_2Cl_2 = δ 5.32 ppm, d_8-THF = δ 3.58 ppm).

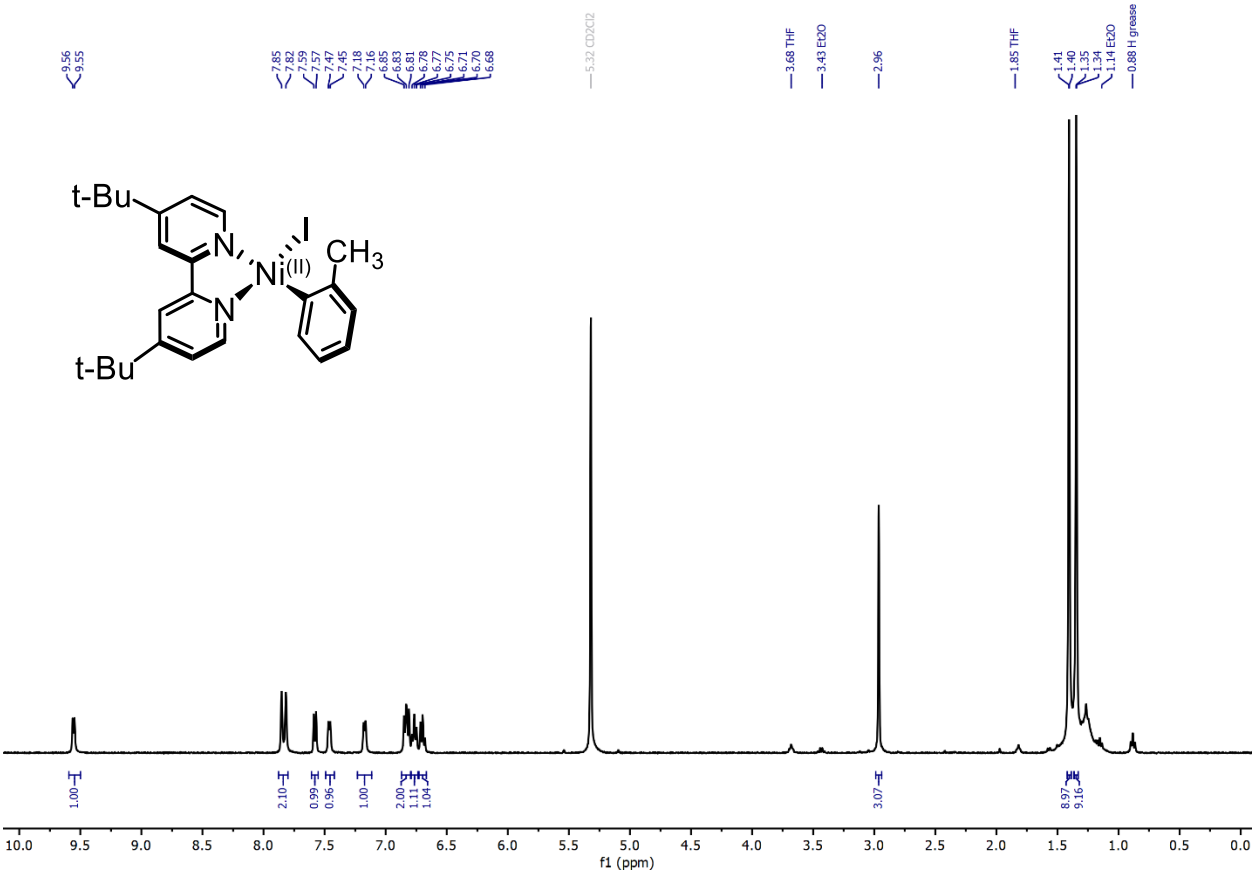

Figure S71. ^{1}H NMR (400 MHz, CD_2Cl_2) spectra of Ni($^{t\text{-Bu}}$bpy)(*o*-tolyl)I, parent compound for **1-I**.

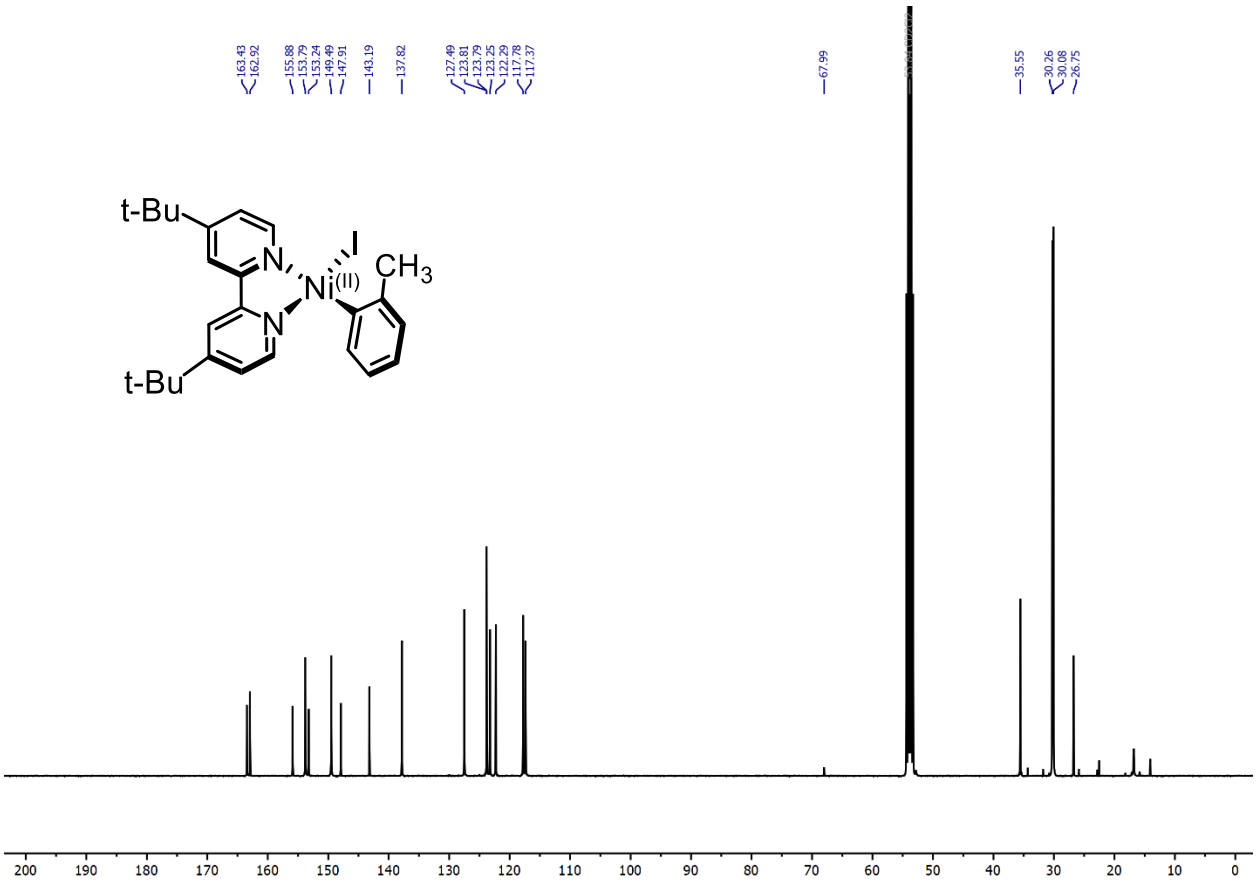

Figure S72. ^{13}C NMR (100 MHz, CD_2Cl_2) spectra of Ni($^{t\text{-Bu}}$bpy)(*o*-tolyl)I, parent compound for **1-I**.

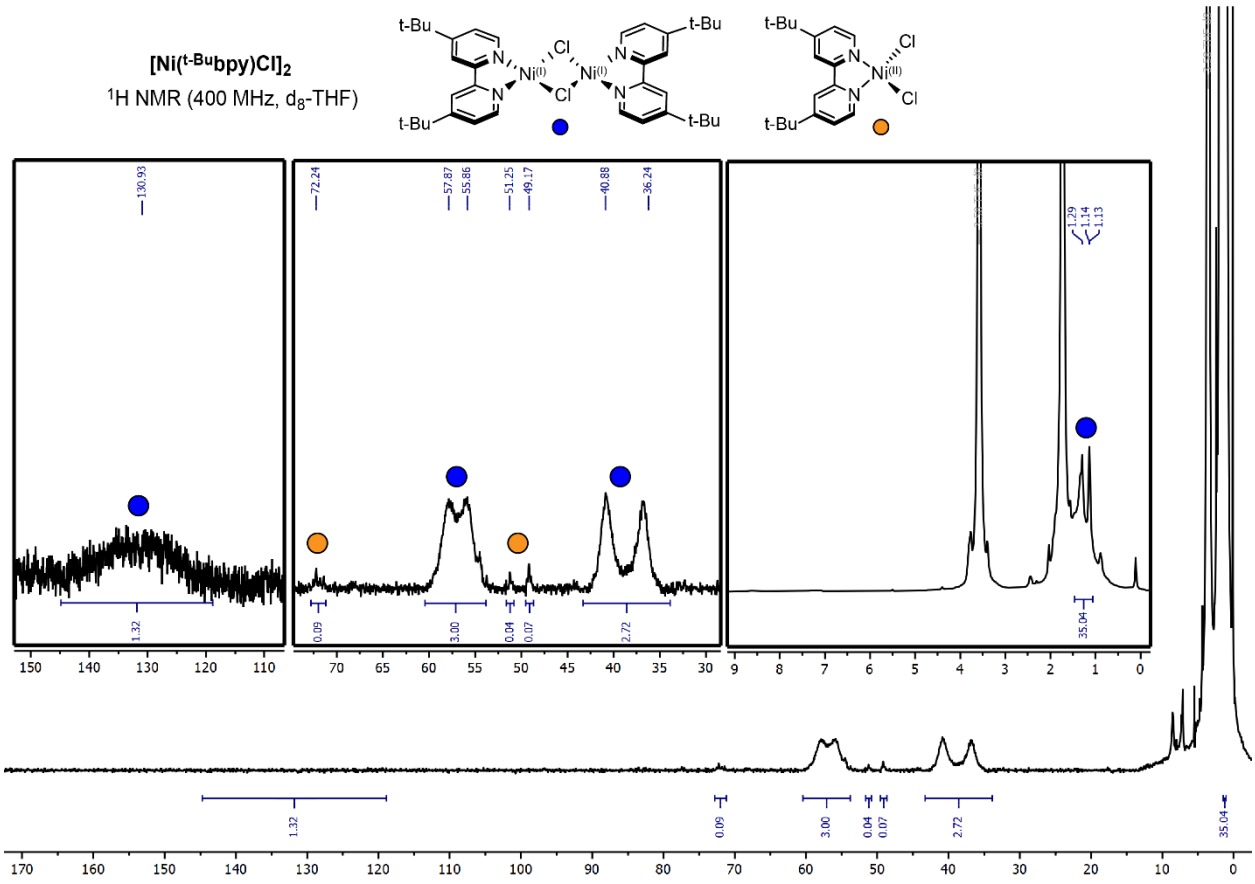

Figure S73. ^{1}H NMR (400 MHz, d_8-THF) spectra of dimeric [Ni(I)($^{t\text{-Bu}}$bpy)Cl]$_2$. A very minor amount of Ni(II)($^{t\text{-Bu}}$bpy)Cl$_2$ (yellow circles) was present in the sample.

S4. References.

(1) Cagan, D. A.; Bím, D.; Silva, B.; Kazmierczak, N. P.; McNicholas, B. J.; Hadt, R. G. Elucidating the Mechanism of Excited-State Bond Homolysis in Nickel–Bipyridine Photoredox Catalysts. *J. Am. Chem. Soc.* **2022**, *144* (14), 6516–6531. https://doi.org/10.1021/jacs.2c01356.

(2) Ting, S. I.; Garakyaraghi, S.; Taliaferro, C. M.; Shields, B. J.; Scholes, G. D.; Castellano, F. N.; Doyle, A. G. ^{3}d-d Excited States of Ni(II) Complexes Relevant to Photoredox Catalysis: Spectroscopic Identification and Mechanistic Implications. *J. Am. Chem. Soc.* **2020**, *142* (12), 5800–5810. https://doi.org/10.1021/jacs.0c00781.

(3) Mohadjer Beromi, M.; Brudvig, G. W.; Hazari, N.; Lant, H. M. C.; Mercado, B. Q. Synthesis and Reactivity of Paramagnetic Nickel Polypyridyl Complexes Relevant to C(sp^2)–C(sp^3)Coupling Reactions. *Angew. Chem. Int. Ed.* **2019**, *58* (18), 6094–6098. https://doi.org/10.1002/anie.201901866.

(4) Stoll, S.; Schweiger, A. EasySpin, a Comprehensive Software Package for Spectral Simulation and Analysis in EPR. *J. Magn. Reson.* **2006**, *178* (1), 42–55. https://doi.org/10.1016/j.jmr.2005.08.013.

(5) Sun, R.; Qin, Y.; Ruccolo, S.; Schnedermann, C.; Costentin, C.; Daniel G. Nocera. Elucidation of a Redox-Mediated Reaction Cycle for Nickel-Catalyzed Cross Coupling. *J. Am. Chem. Soc.* **2019**, *141* (1), 89–93. https://doi.org/10.1021/jacs.8b11262.

(6) Ting, S. I.; Williams, W. L.; Doyle, A. G. Oxidative Addition of Aryl Halides to a Ni(I)-Bipyridine Complex. *J. Am. Chem. Soc.* **2022**, *144* (12), 5575–5582. https://doi.org/10.1021/jacs.2c00462.

(7) Neese, F. The ORCA Program System. *WIREs Comput. Mol. Sci.* **2012**, *2* (1), 73–78. https://doi.org/10.1002/wcms.81.

(8) Neese, F. Software Update: The ORCA Program System—Version 5.0. *WIREs Comput. Mol. Sci.* **2022**, *12* (5), e1606. https://doi.org/10.1002/wcms.1606.

(9) Knizia, G. Intrinsic Atomic Orbitals: An Unbiased Bridge between Quantum Theory and Chemical Concepts. *J. Chem. Theory Comput.* **2013**, *9* (11), 4834–4843. https://doi.org/10.1021/ct400687b.

(10) Knizia, G.; Klein, J. E. M. N. Electron Flow in Reaction Mechanisms—Revealed from First Principles. *Angew. Chem. Int. Ed.* **2015**, *54* (18), 5518–5522. https://doi.org/10.1002/anie.201410637.

(11) Perdew, J. P. Density-Functional Approximation for the Correlation Energy of the Inhomogeneous Electron Gas. *Phys. Rev. B* **1986**, *33* (12), 8822–8824. https://doi.org/10.1103/PhysRevB.33.8822.

(12) Becke, A. D. Density-Functional Exchange-Energy Approximation with Correct Asymptotic Behavior. *Phys. Rev. A* **1988**, *38* (6), 3098–3100. https://doi.org/10.1103/PhysRevA.38.3098.

(13) Weigend, F.; Ahlrichs, R. Balanced Basis Sets of Split Valence, Triple Zeta Valence and Quadruple Zeta Valence Quality for H to Rn: Design and Assessment of Accuracy. *Phys. Chem. Chem. Phys.* **2005**, *7* (18), 3297–3305. https://doi.org/10.1039/B508541A.

(14) Grimme, S.; Antony, J.; Ehrlich, S.; Krieg, H. A Consistent and Accurate Ab Initio Parametrization of Density Functional Dispersion Correction (DFT-D) for the 94 Elements H-Pu. *J. Chem. Phys.* **2010**, *132* (15), 154104. https://doi.org/10.1063/1.3382344.

(15) Grimme, S.; Ehrlich, S.; Goerigk, L. Effect of the Damping Function in Dispersion Corrected Density Functional Theory. *J. Comput. Chem.* **2011**, *32* (7), 1456–1465. https://doi.org/10.1002/jcc.21759.
(16) Klamt, A.; Schüürmann, G. COSMO: A New Approach to Dielectric Screening in Solvents with Explicit Expressions for the Screening Energy and Its Gradient. *J. Chem. Soc. Perkin Trans. 2* **1993**, No. 5, 799–805. https://doi.org/10.1039/P29930000799.
(17) Barone, V.; Cossi, M. Quantum Calculation of Molecular Energies and Energy Gradients in Solution by a Conductor Solvent Model. *J. Phys. Chem. A* **1998**, *102* (11), 1995–2001. https://doi.org/10.1021/jp9716997.
(18) Eichkorn, K.; Treutler, O.; Öhm, H.; Häser, M.; Ahlrichs, R. Auxiliary Basis Sets to Approximate Coulomb Potentials. *Chem. Phys. Lett.* **1995**, *240* (4), 283–290. https://doi.org/10.1016/0009-2614(95)00621-A.
(19) Lee, C.; Yang, W.; Parr, R. G. Development of the Colle-Salvetti Correlation-Energy Formula into a Functional of the Electron Density. *Phys. Rev. B* **1988**, *37* (2), 785–789. https://doi.org/10.1103/PhysRevB.37.785.
(20) Becke, A. D. Density-functional Thermochemistry. III. The Role of Exact Exchange. *J. Chem. Phys.* **1993**, *98* (7), 5648–5652. https://doi.org/10.1063/1.464913.
(21) Neese, F.; Wennmohs, F.; Hansen, A.; Becker, U. Efficient, Approximate and Parallel Hartree–Fock and Hybrid DFT Calculations. A 'Chain-of-Spheres' Algorithm for the Hartree–Fock Exchange. *Chem. Phys.* **2009**, *356* (1), 98–109. https://doi.org/10.1016/j.chemphys.2008.10.036.
(22) Lenthe, E. van; Baerends, E. J.; Snijders, J. G. Relativistic Regular Two-component Hamiltonians. *J. Chem. Phys.* **1993**, *99* (6), 4597–4610. https://doi.org/10.1063/1.466059.
(23) Pantazis, D. A.; Chen, X.-Y.; Landis, C. R.; Neese, F. All-Electron Scalar Relativistic Basis Sets for Third-Row Transition Metal Atoms. *J. Chem. Theory Comput.* **2008**, *4* (6), 908–919. https://doi.org/10.1021/ct800047t.